The influence of disorder in metallic photonic crystals

Dissertation

zur

Erlangung des Doktorgrades

der Naturwissenschaften

(Dr. rer. nat.)

der

Mathematisch-Naturwissenschaftlichen Fakultät

der

Rheinischen Friedrich-Wilhelms-Universität Bonn

vorgelegt von

Dietmar Nau

aus Marburg

Bonn 2006

Angefertigt mit Genehmigung der Mathematisch-Naturwissenschaftlichen Fakultät
der Rheinischen Friedrich-Wilhelms-Universität Bonn

1. Referent: Professor Dr. Harald Gießen
2. Referent: Professor Dr. Karsten Buse

Tag der Promotion: 17.05.2006

Diese Dissertation ist auf dem Hochschulschriftenserver der ULB Bonn
`http://hss.ulb.uni-bonn.de/diss_online` elektronisch publiziert (2006).

Abstract

This thesis provides a comprehensive analysis of the influence of disorder on the optical properties of metallic photonic crystal slabs. These artificial crystals consist of metallic nanowires that are arranged on top of a dielectric waveguide material. Such structures belong to the class of active photonic crystals that exhibit simultaneously electronic and photonic resonances in the same spectral range. The structures show strong coupling effects with characteristic spectral transmission features and pronounced bandstructures. Both are dominated by the properties of a polariton-type quasiparticle. In this work, artificial disorder with a well-defined type and amount is introduced into these structures with high accuracy. When measuring the optical properties of these manipulated systems, a direct relation between disorder type and amount on the one hand and their spectral characteristics on the other hand is found. Thus, the structures presented in this thesis can serve as model system for structures with intrinsic disorder.

In the first part of the thesis, the disorder models are presented and characterized in detail. Different kinds of positional disorder are considered, where the positions of the nanowires on top of the waveguide slab are varied with respect to the perfect arrangement. The disorder models differ in the positions of next-neighbors that are either correlated or uncorrelated. Statistical methods, two-point correlation functions, and Fourier-analysis are utilized to reveal the differences of the models. Transmission experiments at normal light incidence show that disorder strongly influences the optical properties of the structures. The observed modified polariton coupling is explained in terms of a simple model, that is based on the reduced spatial overlap of the resonances in the disordered samples. Furthermore, the observed spectral effects are completely reproduced by a straightforward theory derived from diffraction theory. Angle-resolved measurements yield the bandstructure of the polaritonic system. It is shown how the bandstructure is influenced by disorder type and amount.

In the second part of the thesis, concepts for possible applications are discussed that are based on the perfect metallic photonic crystal slab. Covering the structure with a layer of a photoaddressable polymer allows to realize an all-optical switch. This device makes use of the optically induced birefringence in the polymer layer. The results are confirmed nicely by theoretical calculations. Using a hydrogen-gas sensitive material as waveguide

layer allows to change the transmission spectrum of the sample in dependency of the hydrogen concentration in the surrounding. A change of the transmission as well as of the resonance-wavelengths in different hydrogen atmospheres is observed. Such modified samples can be employed as sensors for hydrogen gas.

Publications

Parts of this thesis have been published in scientific journals:

- **Optical switching in metallic photonic crystal slabs with photoaddressable polymers**
  D. Nau, R. P. Bertram, K. Buse, T. Zentgraf, J. Kuhl, S. G. Tikhodeev, N. A. Gippius, and H. Giessen
  Applied Physics B 82, 543 (2006).

- **Disorder issues in metallic photonic crystals**
  D. Nau, A. Schönhardt, A. Christ, C. Bauer, T. Zentgraf, J. Kuhl, and H. Giessen
  Physica status solidi (b) (2006), in press.

- **Correlation effects in disordered metallic photonic crystal slabs**
  D. Nau, A. Schönhardt, C. Bauer, A. Christ, T. Zentgraf, J. Kuhl, and H. Giessen
  Physical Review Letters (2006), submitted.

- **A hydrogen sensor based on metallic photonic crystal slabs**
  D. Nau, A. Christ, J. Kuhl, S.-H. Lee, S. Deb, and H. Giessen
  Applied Physics Letters (2006), submitted.

Parts of this thesis have been presented on conferences or scientific seminars:

- **Metallic photonic crystals: Superlattices and disorder effects**
  H. Giessen, D. Nau, A. Christ, A. Schönhardt, T. Zentgraf, S. G. Tikhodeev, N. A. Gippius, and J. Kuhl
  NOEKS-8 2006, Münster, Invited Talk (Th 2-1)

- **Linear and nonlinear optical properties of strongly coupled metallic nanoparticles**
  H. Giessen, A. Christ, D. Nau, A. Schönhardt, T. Zentgraf, C. Bauer, S. G. Tikhodeev, N. A. Gippius, and J. Kuhl
  QELS 2006, San José, USA, Invited Talk

- **The influence of the disorder type on the optical properties of metallic photonic crystals**
  D. Nau, A. Schönhardt, A. Christ, J. Kuhl, and H. Giessen
  IQEC and CLEO-PR 2005, Tokyo, Japan, Talk CTuE4-6

- **Disorder in metallic photonic crystals**
  D. Nau, A. Schönhardt, A. Christ, J. Kuhl, and H. Giessen
  PECS-VI 2005, Crete, Greece, Poster C-31

- **The influence of disorder on the optical properties of metallic photonic crystals**
  D. Nau, A. Schönhardt, A. Christ, J. Kuhl, and H. Giessen
  DPG spring meeting 2005, Berlin, Germany, Talk HL 62.5

- **The influence of disorder in metallic photonic crystal slabs**
  D. Nau, A. Christ, S. Linden, J. Kuhl, and H. Giessen
  IQEC 2004, San Francisco, USA, Talk IThB6

- **Fano resonances in metallic photonic crystals**
  H. Giessen, S. Linden, A. Christ, J. Kuhl, D. Nau, T. Meier, P. Thomas, and S. W. Koch
  IQEC 2004, San Francisco, USA, Talk IFC5

- **The influence of disorder on the optical properties of metallic photonic crystals**
  D. Nau, H. Giessen, A. Christ, J. Kuhl, C. Zanke, M. Frommberger, and E. Quandt
  DPG spring meeting 2003, Hannover, Germany, Poster Q49.23

Additional publications that are not presented in this thesis:

- **Phase-resolved pulse propagation through metallic photonic crystal slabs**
  A. Schönhardt, D. Nau, C. Bauer, H. Gräbeldinger, and H. Giessen
  Phys. Rev. B (2006), submitted.

- **Metallic photonic crystals based on solution-processible gold nanoparticles**
  X. P. Zhang, B. Sun, R. H. Friend, H. Guo, D. Nau, and H. Giessen
  Nano Lett. 6, 651 (2006).

- **Metallodielectric photonic crystal superlattices: Influence of periodic defects on transmission properties**
  T. Zentgraf, A. Christ, J. Kuhl, N. A. Gippius, S. G. Tikhodeev, D. Nau, and H. Giessen
  Phys. Rev. B 73, 115103 (2006).

- **Photonic crystals with polymer waveguides for microforce detection**
  B. Winzek, V. Emelianov, A. Radke, H. Guo, D. Nau, and H. Giessen
  Proc. SPIE 5950, 26 (2005).

- **Large-area metallic photonic crystal fabrication with interference lithography and dry etching**
  H. C. Guo, D. Nau, A. Radke, X. P. Zhang, J. Stodolka, X. L. Yang, S. G. Tikhodeev, N. A. Gippius, and H. Giessen
  Appl. Phys. B 81, 271 (2005).

- **Fabrication of two-dimensional hybrid photonic crystals utilizing electron beam lithography**
  J. Stodolka, D. Nau, M. Frommberger, C. Zanke, H. Giessen, and E. Quandt
  Microelectronic Engineering 78-79, 442-447 (2005).

- **Group velocity dispersion of tapered fibers immersed in different liquids**
  R. Zhang, J. Teipel, X. Zhang, D. Nau, and H. Giessen
  Opt. Express 12, 1700 (2004).

- **Optical properties of planar metallo-dielectric photonic crystals**
  A. Christ, S. Linden, T. Zentgraf, K. Schubert, D. Nau, S. G. Tikhodeev, N. A. Gippius, J. Kuhl, F. Schindler, A. W. Holleitner, J. Stehr, J. Crewett, J. Lupton, T. Klar, U. Scherf, J. Feldmann, C. Dahmen, G. von Plessen, and H. Giessen
  In: Photonic Crystals (ed. by H. Föll, Wiley, 2004), pp. 85-108.

- **Fabrication of metallic photonic crystals by optical interference lithography**
  K. Mellert, D. Nau, and H. Giessen
  PECS-IV, Los Angeles 2002, Poster II-28.

- **1 GHz repetition rate femtosecond optical parametric oscillator**
  X. P. Zhang, J. Hebling, A. Bartels, D. Nau, J. Kuhl, W. W. Rühle, and H. Giessen
  Appl. Phys. Lett. 80, 1873 (2002).

- **Spectrally and temporally resolved measurements of white light continuum generated in tapered fibers**
  H. Giessen, K. Franke, J. Teipel, D. Meiser, K. Mellert, D. Nau, and M. Leuschner
  OSA Trends in Optics and Photonics (TOPS), Vol. 79, Nonlinear Optics, OSA Technical Digest, Postconference Edition (Optical Socienty of America, Washington DC, 2001), pp. 461-463.

Contents

List of Figures

List of Tables

Chapter 1

Introduction

A lot of effort has been made in recent times to examine the optical properties of nanoscaled materials. They do not only show interesting optical and physical properties, they are also considered to be promising materials for various applications and quantum information processing. A special class of nanostructured media are photonic crystals. The idea behind these crystals is to design materials that can affect the properties of light, similar to the modified properties of electrons in semiconductors. This is realized by a periodic variation of the dielectric constant, where the periodicity is on the order of the wavelength of light [1]. Such an arrangement can cause Bragg scattering of electromagnetic waves, resulting in a gap in their electromagnetic transmission characteristic [1]. A photonic bandgap describes an energy range for which light is forbidden to propagate and to even exist inside the crystal. Depending on the dimensionality of the dielectric constant variation, the material is called a 1-dim, 2-dim or 3-dim photonic crystal, see Fig. 1.1.

The idea for these crystals arose several years ago. Yablonovitch suggested a periodic dielectric structure to control the radiative properties of materials [2]. John had the idea to localize light inside disordered dielectrica [3]. Especially the idea to use photonic crystal structures to guide light brought about fascinating concepts to develop photonic crystal based applications. Contrary to total internal reflection that is usually utilized to direct light in dielectrica, photonic crystals allow light guiding by using photonic bandgaps to confine light along defect lines in the otherwise perfect crystal [1]. Due to their interesting optical properties, these crystals brought forward a lot of fascinating ideas like beam splitting with photonic crystals [4], enhancing light extraction from light-emitting diodes [5], developing integrated optical elements like routers and switches [6], or sensing applications.

While the idea of dielectric photonic crystals was developed a number of years ago, the concept of metallic photonic crystals has gained a lot of interest only recently [7]. In metal based structures, one of the dielectric constituents is replaced by a metal. One possibility to fabricate such structures is for example to arrange metallic nanostructures

[1] Only if the difference of the dielectric constants is large enough.

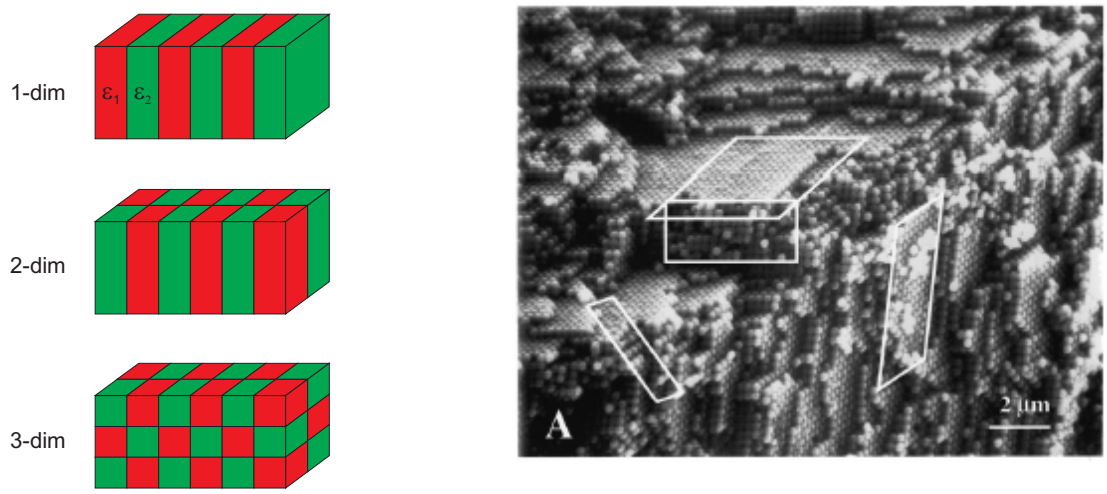

Figure 1.1: Left panel: Photonic crystals made of materials with different dielectric constants ε_1 and ε_2. From top to bottom: 1-dim, 2-dim, 3-dim. Right panel: SEM-image of a disordered photonic crystal made of opals. Taken from [11].

periodically on top of a dielectric waveguide slab [8]. This structure belongs to the class of active crystals that provide simultaneously photonic and electronic resonances in the same spectral range. Not only interesting physical effects like a strong coupling between the resonances were observed [9]. Also, possible applications based on these structures were discussed [10].

One problem arises when working with photonic crystals. Theory and device concepts always deal with perfect periodic structures, where the different dielectrica are arranged on perfect lattices. However, such crystals are artificially fabricated materials. Especially when working in the visible spectral range, the fabrication requirements often reach the limits of the utilized machines. Consequently, real photonic crystals can show strong deviations from the perfect structure [11], see Fig. 1.1. Of course, such disorder directly influences the optical properties of real crystals [12]. Not only possible applications require a detailed knowledge about the influence of disorder in these artificial structures. From a fundamental point of view, the already interesting optical properties of photonic crystals show some further interesting effects in the presence of disorder. Typical examples are disorder-induced modifications of photon states and of the transmission. In his elementary work John found, that disorder can strongly modify the photon density of states by causing Anderson localization of light [3]. The band edge is shifted and a spectral mobility edge appears that separates localized and extended photon states. Interestingly, such localized states can give rise to a macroscopic non-localized mode, a so-called optical necklace state [13]. Localized states with nearly identical energies can couple to form a non-localized mode, that is extended over the entire sample via multiple resonances. Fur-

thermore, disorder-induced modifications of the linear optical properties were reported. The influence of localization on the transmission of certain disordered systems was discussed in [14]. There, disorder can widen the transmission gap in a frequency range that is much broader than the gap in the ordered system. This result was explained with the occurrence of localized states in a wide-spread frequency range. A different phenomenon was reported in [15], where enhanced transmission inside the bandgap at moderate disorder amounts was observed. Additional channels in the density of states that appear in the disordered system were proposed as possible origin of this effect. These states that are not present in the perfect system enable the propagation of light at frequencies within the bandgap.

Further publications about disorder in photonic crystals can be found in the literature. However, they all deal with dielectric photonic crystals. Also, a quantitative ab-initio theory for the description of the optical properties is missing. Most theoretical papers present simulations, based on averaging FDTD calculations. Apart from the lacking theory, to our knowledge no results have been reported on disordered metallic systems so far. It is the aim of this thesis to enlighten the influence of disorder on the optical properties of metallic photonic crystals slabs. Therefore, a new concept to study this relation in a quantitative way is presented by artificially introducing disorder in a controlled manner into the structures. Measuring their optical properties allows to directly relate transmission spectra to disorder type and amount. The structures consist of a metallic nanowire arrangement on top of a dielectric waveguide slab. As electron-beam lithography is used to fabricate the samples, we are able to control the nanowires' positions and shapes with a very high accuracy. This process provides us with a powerful tool to introduce artificial disorder with a well-defined type and strength into the crystals. A straightforward theory derived from diffraction theory helps to understand the experimentally observed spectral features.

In the second part of this thesis, two applications based on the perfect structure are presented. Covering the structure with a photoaddressable polymer (PAP) helps to realize an all-optical switch. Illuminating PAP optically within its absorption band induces a birefringence, that changes the transmission of the metallo-dielectric structure reversibly. When a gas-sensitive dielectric medium is used as waveguide layer, a direct relation between the gas concentration in the surrounding and changes in the transmission of the structure can be found. Such a material is tungsten oxide (WO_3) that allows to build a hydrogen sensor.

This work is organized as follows. After introducing the optical properties of metallic photonic crystal slabs and analyzing them from several perspectives in Chapter 2, the sample fabrication and the experimental setup are described (Chapter 3). Then, the considered disorder models are characterized in Chapter 4. The models are presented and analyzed by means of statistical methods, two-point correlation-functions, and Fourier

analysis. Experimental and theoretical results are shown and discussed in detail in Chapter 5. In the last two chapters of this thesis we concentrate on applications based on the perfect structures. Concepts for an all-optical switch and for a hydrogen sensor are given in Chapters 6 and 7, respectively.

Chapter 2

Theory

In this chapter we will introduce the basic physical phenomena of metallic photonic crystal slabs. These structures consist of a metallic grating arrangement on top of a dielectric waveguide layer that is deposited on a quartz substrate. The outline of this chapter is as follows: we will start with the description of the metallic nanostructures and their electronic resonances, then consider waveguide materials and their optical resonances, and finish with the compound system of metallic nanostructures and waveguide materials. The last part of this chapter deals with disordered systems.

2.1 Optical properties of metallic nanostructures

We will derive the optical properties of metallic nanostructures in this section. After discussing the dielectric function $\epsilon(\omega)$ of metals, especially of gold, an overview of the theory of the optical properties of metallic nanostructures will be presented. General expressions for calculating the extinction of light by nanoparticles will be expanded for particles that are smaller than the wavelength of light. These expressions already allow a good description of the concept of particle plasmons which are of major importance in metallic photonic crystal slabs.

2.1.1 Dielectric function of gold

In this section we deal with the electrical and optical properties of small structures made of metals. This kind of material is characterized by a high electrical conductivity because a large number of conduction electrons can move freely in the metal [16]. Their mobility is caused by an usually low binding energy of the valence electrons. As we are dealing with gold nanostructures in this work, we will concentrate in the following on this material and adopt the theory to it. Gold as a noble metal has a completely filled 5d-orbital, the relevant outer electron configuration is $5d^{10}6s$ [16]. This configuration influences the electrical and optical properties of gold because it determines the dielectric function $\epsilon(\omega)$. This function describes the linear response of the material to electromagnetic waves and

is related to the polarization $\mathbf{P}$ by

$$\epsilon(\omega) = 1 + P/(\epsilon_0 E), \tag{2.1}$$

where E is the amplitude of the electrical field and $P = |\mathbf{P}|$. Due to the electron configuration of gold, its dielectric function $\epsilon(\omega)$ has two contributions. One part originates from the conduction band electrons, denoted as $\chi^C(\omega)$. The second contribution is caused by interband transitions between the completely filled 5d-orbital and the partially filled 6sp-orbital. We will refer to this contribution as $\chi^{IB}(\omega)$. The dielectric function $\epsilon(\omega)$ of gold can be specified by [1]

$$\epsilon(\omega) = 1 + \chi^C(\omega) + \chi^{IB}(\omega). \tag{2.2}$$

$\chi^C(\omega)$ can be modeled with the Drude-Lorentz-Sommerfeld theory [17], where the conduction electrons are described in terms of a free electron model. According to this model, the valence electrons become conduction electrons that can move freely through the crystal [16]. The theory starts in a first step by determining the response of a single conduction electron to external forces. The electron is considered to be a Lorentz harmonic oscillator with mass m_e [18]. Macroscopic effects are taken into account by multiplying the effect of the single electron by the number n of electrons. For an electrical field $\mathbf{E} = \mathbf{E}_0 \exp(-i\omega t)$, $\chi^C(\omega)$ is given as [17]

$$\chi^C(\omega) = -\frac{\omega_p^2}{\omega^2 + \Gamma^2} + i\frac{\omega_p^2 \Gamma}{\omega(\omega^2 + \Gamma^2)} \tag{2.3}$$

with

$$\omega_p = \sqrt{\frac{ne^2}{\epsilon_0 m_e}} \tag{2.4}$$

as the Drude plasma frequency (see below). Γ is a damping constant that is related to the electron mean free path l by $\Gamma = v_F/l$ with the Fermi velocity v_F.

Figure 2.1 shows experimental and theoretical data for $\epsilon(\omega)$ of gold. Plotted are the real ϵ_1 and the imaginary part ϵ_2 with $\epsilon(\omega) = \epsilon_1(\omega) + i\epsilon_2(\omega)$. The experimental data were taken from [19], the theoretical results were obtained from the Drude-Lorentz-Sommerfeld model in Eqn. (2.3). The free parameters were set to $\hbar\omega_p = 8.6$ eV and $\hbar\Gamma = 0.08$ eV. We observe a good agreement between experiment and theory for energies below 2.0 eV. The deviations become stronger for larger energies, indicating that the Drude-Lorentz-Sommerfeld model can no longer be used to model $\epsilon(\omega)$. This energy region marks a threshold for the onset of the interband transitions [19]. Above this energy, the form of the curve depends on the specific band structure of gold. The threshold for interband absorption in gold was determined to be around 2.4 eV [20]. As a result, the Drude-Lorentz-Sommerfeld model of the free-electron behavior is valid only in the near-infrared

[1] This equation is valid for all metals [17].

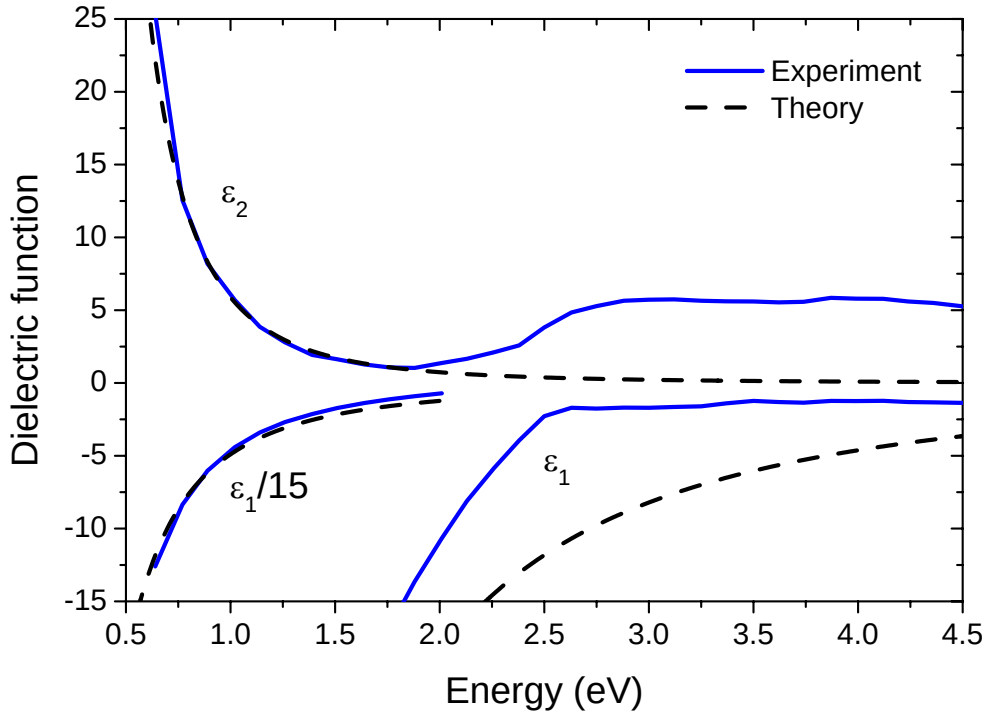

Figure 2.1: Dielectric function $\epsilon(\omega)$ of gold. Solid line from measurements (data taken from [19]), dotted line as determined by the Drude-Lorentz-Sommerfeld model, see Eqn. (2.3).

region. The deviations become stronger in the visible spectral range, the model can no longer be used for even higher energies.

To correctly describe $\epsilon(\omega)$, the contribution of the interband transition $\chi^{IB}(\omega)$ to $\epsilon(\omega)$ has to be taken into account. This part of the susceptibility can be calculated with an electric-dipole approximation for the electron-photon interaction Hamiltonian for direct transitions [17]. The model includes the band structure $E(\mathbf{k})$ of the solid and the transition matrix elements M_{if} for the interband transition between initial state i and final state f. We receive

$$\begin{aligned}\chi^{IB}(w) &= \frac{8\hbar^3\pi e^2}{m_{eff}^2}\sum_{i,f}\int_{BZ}\frac{2d\mathbf{k}}{(2\pi)^3}|\mathbf{e}M_{if}(\mathbf{k})|^2 \\ &\left(\frac{1}{[E_f(\mathbf{k})-E_i(\mathbf{k})][(E_f(\mathbf{k})-E_i(\mathbf{k}))^2-\hbar^2\omega^2]}\right. \\ &\left.+\, i\frac{\pi}{2\hbar^3\omega^2}\,\delta[E_f(\mathbf{k})-E_i(\mathbf{k})-\hbar\omega]\right).\end{aligned} \tag{2.5}$$

Here, $\mathbf{e}$ is the unit vector along the direction of the electric field, E_i and E_f denote the energies of initial and final state. The integral covers the first Brillouin zone. The

imaginary part of $\chi^{IB}(\omega)$ provokes a direct energy dissipation. Directly related to it is a damping of the electronic excitation in the material [8]. A consequence of the discussed theory is the fact that independent optical excitation processes (interband and intraband transitions) result in a modified $\epsilon(\omega)$ [see Eqn. (2.2)]; they do not affect the optical absorption [17].

We already mentioned the Drude plasma frequency ω_p in Eqn. (2.4). This frequency gives a hint about the microscopic processes within the material. Metals consist of negatively charged conduction electrons and positively charged ion cores with their concentrations being equal. A system with equal concentrations of positive and negative charges and at least one type being mobile is called a plasma [16]. The value ω_p gives the eigenfrequency of a longitudinal oscillation of the conduction electrons. This eigen-oscillation of the free electrons in the background of the immobile ion cores is called a *plasmon*.

2.1.2 Optical properties of single metallic nanoparticles

Now we want to focus on the optical properties of metallic clusters or nanoparticles. Clusters are an intermediate state between atoms and solids or liquids [17]. In general, they are build of a number of unspecified objects. This general definition does not include a specific size scale, they are rather characterized by the numbers of the objects. When dealing with atomic clusters, the clusters are composed of N atoms with $3 < N < 10^7$ [17]. Depending on N, the clusters are divided into different classes, see Table 2.1. In the following, we will always deal with large clusters made of a metal.

N	**Size**
$2 < \mathrm{N} \leq 20$	Very small clusters
$20 \leq \mathrm{N} \leq 500$	Small clusters
$500 \leq \mathrm{N} \leq 10^7$	Large clusters

Table 2.1: Definition of cluster sizes.

When illuminating such particles by a beam of light, parts of the light are scattered, absorbed, and reflected. The response of a particle to light with arbitrary polarization depends strongly on shape, size, and material of which it is composed [18]. We will start with considering an arbitrary particle, neglecting its specific parameters. The theory follows the calculation in [18], however, only the most important aspects are given here. The main focus will be set on numerical results of the optical properties of certain gold nanostructures.

The problem of calculating the optical properties is to determine the electromagnetic field inside the particle $(\vec{E}_1, \vec{H}_1)$ and in the surrounding $(\vec{E}_2, \vec{H}_2)$. The field in the surrounding is a superposition of the incoming field $\vec{E}_i, \vec{H}_i$ and the scattered field at the particle $\vec{E}_s, \vec{H}_s$

$$\vec{E}_2 = \vec{E}_i + \vec{E}_s, \qquad \vec{H}_2 = \vec{H}_i + \vec{H}_s. \tag{2.6}$$

These fields must obey the Maxwell equations and the resulting vector wave equations

$$\vec{\nabla}^2\vec{E} + k^2\vec{E} = 0, \qquad \vec{\nabla}^2\vec{H} + k^2\vec{H} = 0. \tag{2.7}$$

Comparing the incoming field with the scattered electromagnetic field gives information about the extinction of light by the particle. Energy of the incoming field is absorbed by the particle and part of it is then scattered into different directions. The extinction is defined as the attenuation of the incoming field by scattering and absorption. With the time-averaged Poynting vector

$$\vec{S} = \frac{1}{2}\mathrm{Re}(\vec{E}_2 \times \vec{H}_2^*) = \vec{S}_i + \vec{S}_s + \vec{S}_{ext}, \tag{2.8}$$

where we have divided $\vec{S}$ into components

$$\begin{aligned} \vec{S}_i &= \frac{1}{2}\mathrm{Re}(\vec{E}_i \times \vec{H}_i^*) \\ \vec{S}_s &= \frac{1}{2}\mathrm{Re}(\vec{E}_s \times \vec{H}_s^*) \\ \vec{S}_{ext} &= \frac{1}{2}\mathrm{Re}(\vec{E}_i \times \vec{H}_s^* + \vec{E}_s \times \vec{H}_i^*), \end{aligned} \tag{2.9}$$

the cross-sections of absorption, scattering and extinction can be calculated. Here, $\vec{S}_i$ is the Poynting vector associated with the incoming field, $\vec{S}_s$ is the Poynting vector of the scattered field, and $\vec{S}_{ext}$ the term that arises from the interaction of incident and scattered fields. To determine the cross-sections, we need to know the absorbed power W_a and the scattered power W_s. Therefore, we construct an imaginary sphere with radius r and surface A around the particle. As the surrounding material was assumed to be not absorbing, W_a is determined only by the absorption of the particle as $W_a = W_i - W_s + W_{ext}$. In a non-absorbing media, also W_i vanishes, we receive

$$W_{ext} = W_a + W_s = -\int_A \vec{S}_{ext} \cdot \vec{e}_r \, dA \tag{2.10}$$

with

$$W_s = -\int_A \vec{S}_s \cdot \vec{e}_r \, dA, \qquad W_a = -\int_A \vec{S} \cdot \vec{e}_r \, dA \tag{2.11}$$

as energy scattering rate and energy absorption rate, respectively. With $I_i = |\vec{S}_i|$ as the intensity of the incoming light field, we can determine the cross-sections of absorption, scattering, and extinction as

$$C_a = \frac{W_a}{I_i}, \qquad C_s = \frac{W_s}{I_i}, \qquad C_{ext} = \frac{W_{ext}}{I_i}. \tag{2.12}$$

They can be understood as imaginary areas that shadow the incoming light field and reduce its power according to Eqn. (2.12) [8].

These results describe the response of a single particle on an incident electromagnetic field. Now we want to concentrate on an ensemble of non-interacting identical particles. Their density $\mathcal{N}$ is defined as the number of particles per unit volume. We are interested in the transmitted field $\vec{E}_t$ at a point P that lies in the forward direction of the light beam but outside of the area of the particle ensemble. $\vec{E}_t$ is the sum of the incident field $\vec{E}_i$ and the fields scattered at the particles:

$$\vec{E}_t = \vec{E}_i + \sum_j \vec{E}_{s,j}. \tag{2.13}$$

After some calculations it is found that the transmitted field $\vec{E}_t$ is only determined by the scattered light in forward direction. Light that is scattered into different directions does not play a role because it interferes destructively. Additionally, the polarization of the light has changed in P: Initially linearly polarized light shows an elliptical polarization. Neglecting this polarization effect allows to describe the macroscopic extinction by microscopic parameters. With α_{Ext} as the extinction coefficient in the Lambert-Beer absorption law

$$I_t(z) = I_i \exp(-\alpha_{Ext} z), \tag{2.14}$$

we can derive the macroscopic extinction coefficient α_{Ext} as a function of C_{ext}

$$\alpha_{Ext} = \mathcal{N} C_{ext}. \tag{2.15}$$

This remarkable results indicates that an ensemble of particles shows a macroscopic extinction that can be derived by the particle density $\mathcal{N}$ and the microscopic extinction cross-section C_{ext}.

2.1.3 Electrostatic approximation

So far, this theory is not related to special particles and deals with general properties. However, using these results to find a solution for a specific problem is difficult. The optical properties can be evaluated only for some simple cases. Especially for spherical particles an analytical solution of the Maxwell equations exists that allows to determine C_a, C_s and C_{ext}. The underlying theory is called *Mie theory* after Gustav Mie who published the corresponding results in 1908 [21]. This theory is valid for particles with a radius larger than 10 nm.

A different approach is the *electrostatic approximation* where C_a, C_s, and C_{ext} can be determined approximately for particles that are smaller than the wavelength of the light [18]. In this approximation the particle can be considered to be located in a homogeneous electrical field whose temporal changes act simultaneously on the whole particle [8]. The particle can then be understood as a dipole that is excited by the incoming electrical field.

Its dipole moment

$$\vec{p} = \epsilon_m \alpha \vec{E}_0 \tag{2.16}$$

includes the permittivity ϵ_m of the surrounding medium and the amplitude $\vec{E}_0$ of the electrical field. The polarizability α can be determined by electrostatic methods and contains the material properties and the geometrical size of the particle. Using the above presented formalism allows to express C_a, C_s and C_{ext} as a function of α:

$$C_{ext} = k\,\mathrm{Im}(\alpha), \quad C_s = \frac{k^4}{6\pi}|\alpha|^2, \quad C_a \approx C_{ext} = k\,\mathrm{Im}(\alpha). \tag{2.17}$$

We used the momentum k of the illuminating plane wave and the fact that the absorption dominates for small particles [18]. The scattering is neglectable, hence $C_a \approx C_{ext}$.

Especially ellipsoids can be treated with the electrostatic approximation. They are smooth particles of regular shape, characterized by three principal axes r_x, r_y, and r_z and permittivity ϵ_1. For ellipsoidal particles, the polarizability α is a symmetric second order tensor whose components

$$\alpha_j = 4\pi r_x r_y r_z \frac{\epsilon_1 - \epsilon_m}{3\epsilon_m + 3L_j(\epsilon_1 - \epsilon_m)}, \quad j = x, y, z \tag{2.18}$$

include the form factors

$$L_j = \frac{r_x r_y r_z}{2} \int_0^\infty \frac{dq}{(r_j^2 + q)\sqrt{(r_x^2 + q)(r_y^2 + q)(r_z^2 + q)}}, \quad j = x, y, z. \tag{2.19}$$

With this notation, the cross-sections C_a, C_s and C_{ext} are seen to depend on the polarization of the incoming light field. For a light polarization parallel to the main axis r_x, r_y or r_z, we calculate

$$C_{ext,x} = k\,\mathrm{Im}(\alpha_x), \quad C_{ext,y} = k\,\mathrm{Im}(\alpha_y), \quad \text{or} \quad C_{ext,z} = k\,\mathrm{Im}(\alpha_z) \tag{2.20}$$

for the extinction and

$$C_{s,x} = \frac{k^4}{6\pi}|\alpha_x|^2, \quad C_{s,y} = \frac{k^4}{6\pi}|\alpha_y|^2, \quad \text{or} \quad C_{s,z} = \frac{k^4}{6\pi}|\alpha_z|^2 \tag{2.21}$$

for the scattering [8]. It can be seen that for ellipsoids with axis $r_x \neq r_y \neq r_z$ the cross-sections in the corresponding directions are different. As an example, Figure 2.2 shows the calculated $C_{ext,x}$ of an ellipsoid with $r_x = r_y = 100$ nm and increasing height r_z. We used the experimentally determined dielectric function of gold, as reported in [19]. A broad peak appears in the visible spectral range that shifts to higher energies for increasing r_z. It is a typical result for particles made of noble metals whose resonances are usually excited in the visible or infrared part of the spectrum [17]. The agreement of the electrostatic approximation with experimental results was shown to match very well (see e.g. [8]).

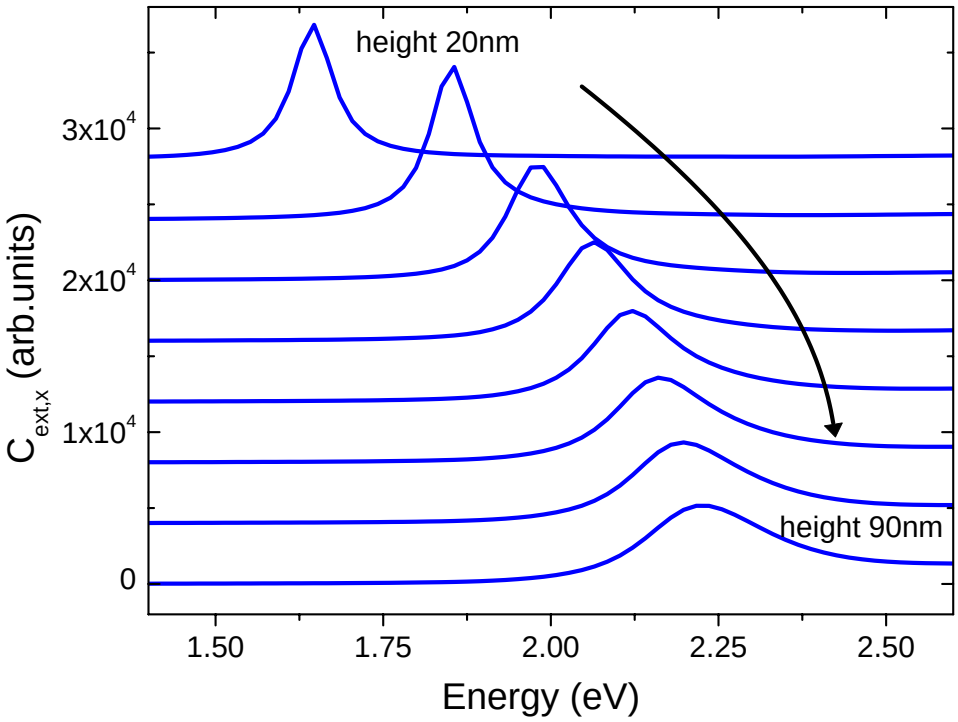

Figure 2.2: Extinction cross-section $C_{ext,x}$ of an ellipsoid made of gold in a medium with $\epsilon_m = 2.92$, calculated by the electrostatic approximation. The radii $r_x = r_y = 100$ nm were kept fixed, the height r_z of the particle was increased from 20 nm to 90 nm. The individual spectra are shifted upwards for clarity.

So far, we only calculated the optical properties of metallic nanoparticles. However, from the presented theory it is not yet made clear what happens on a microscopic level inside the particles. A simple oscillator model helps to clarify the effects [17]. In the Drude-Lorentz-Sommerfeld model we assumed the conduction electrons to be able to move freely in the solid whereas the positively charged ionic background is assumed to be spatially fixed. An incident electromagnetic field can displace the electrons with respect to the ions, resulting in polarization charges at the particle surface. Such a polarization is connected with restoring forces between the ions and the electrons. In particles, the electrons behave like an oscillator, its eigenfrequency w_0 is determined both by the restoring force and the Drude plasma frequency w_p, see Eqn. (2.4). These oscillations of the conduction electrons in metallic nanoparticles are called *particle plasmons*. While the resonance frequency in bulk metal is $w_0 = w_p$, it is given in ellipsoids by $w_0 = w_p L_j$ and in spherical particles by $w_0 = \frac{w_p}{\sqrt{3}}$ $(L_x = L_y = L_z = 1/\sqrt{3})$ [17]. Figure 2.3 visualizes the particle plasmon in a spherical particle. It should be noted that according to the Mie theory particle plasmons are better described by multipoles rather than by dipoles [18].

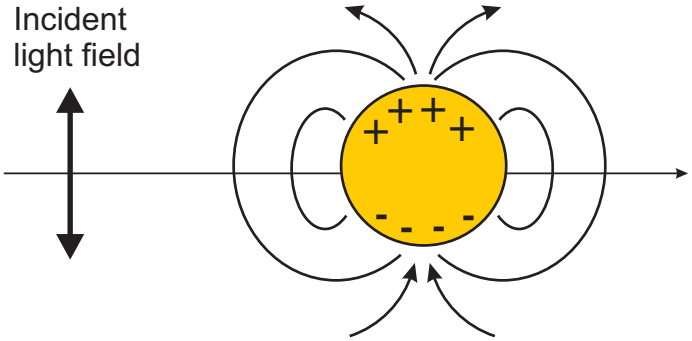

Figure 2.3: The incident light field excites an oscillation of the surface electrons in metallic nanostructures. This oscillation is called particle plasmon.

2.1.4 Additional remarks

One important result of the above presented theory is the fact that the optical properties of an ensemble of metallic nanoparticles only depend on the geometric sizes of the particles and the dielectric functions of the involved materials. The theory does not include the distance between the particles. However, this is not correct because the particles can interact with each other and the interaction strongly depends on the interparticle distance. As mentioned above, plasmons are described in the Mie theory by oscillating dipoles or even higher multipoles. Therefore, an oscillating radiating dipole field of the plasmon can be observed [18]. As a consequence, an electromagnetic interaction of the emitted radiative field of a plasmon with the other plasmons is expected. Since the emitted intensity decreases with increasing distance from the radiation source, also this interaction should depend on the distance of adjacent nanoparticles. Typically, two types of interaction are distinguished: *near-field* coupling and *far-field* dipolar interaction [22]. Near-field coupling is relevant for particle distances on the order of a few tens of nm because of the short range of the electromagnetic near-fields. These fields decline with $1/r^3$ with r being the distance from the dipole. Far-field coupling appears for larger inter-particle distances since the far-field drops with $1/r$.

It was observed experimentally, that near-field coupling of metallic nanoparticles influences the extinction of the ensemble [23]. Depending on the polarization of the exciting light field, a red- or blue-shift of the spectral resonance associated with the particle plasmon was observed. This effect was explained by an influence of the electromagnetic fields on the restoring forces of the electron oscillation in neighboring nanostructures. To quantify the near-field coupling of metallic nanoparticles, one can use e.g. the boundary-element method [24] to calculate the electromagnetic near-field in the surrounding of the particles.

Far-field coupling of the nanoparticles arises due to scattered dipolar light fields and not by the direct field [22]. Here, the scattered dipolar light fields from the nanostructures lead to an interaction of the ensemble of the nanostructures. These scattered fields interfere to form a collective radiation. Lambrecht *et al.* also found a shifting of the particle plasmon resonance depending on the particle-distance [22]. The scattered fields of neighboring particles are superimposed with their respective phase shifts to interact on the individual particles. Therefore, the particle-distance determines the amplitude of this collective radiation and thus the plasmon resonance of the individual particles.

An interaction of the nanoparticles was also observed for a coupling of nanostructures to an electromagnetic surface mode, see e.g. [25].

To conclude this section, the optical properties of individual metallic nanoparticles can be well described and calculated by the electrostatic approximation. However, this theory completely neglects the interaction of the particles in an ensemble. Therefore, the optical properties of ensembles of metallic nanoparticles can deviate from the above presented results.

2.2 Waveguide mode

A waveguide layer consists of a dielectric medium sandwiched between other dielectric materials. These layers are characterized by their dielectric constants ϵ_S (substrate), ϵ_M (waveguide medium) and ϵ_C (cover layer), the waveguide layer has the thickness L_z (see Fig. 2.4).

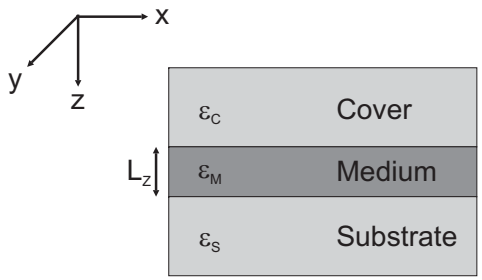

Figure 2.4: Setup of a waveguide system consisting of substrate, waveguide film and cover, characterized by their dielectric constants ϵ_S, ϵ_M, and ϵ_C.

If L_z is above a critical thickness and if

$$\epsilon_M > \epsilon_S, \quad \epsilon_M > \epsilon_C, \tag{2.22}$$

a guided mode can propagate inside the waveguide layer. In a simplified picture, this can be understood by considering the path of a light beam by means of geometrical

optics. A beam inside the waveguide medium is totally reflected at the surfaces to the other media, if the angle to the surfaces is above the critical angle of total reflection [26]

$$\alpha_{TR} = \arcsin\left(\sqrt{\frac{\epsilon_j}{\epsilon_M}}\right), j = S, C. \tag{2.23}$$

The beam is reflected at the surfaces to the surrounding media and trapped inside the waveguide layer. Such light fields inside a slab are referred to as *guided modes* [27, 28]. They are bound modes in the sense that they are infinitely extended within the slab and decay exponentially into the surrounding of the slab. In a planar waveguide layer $m = 0, 1, 2, \ldots$ transverse electrical (TE) and transverse magnetical (TM) resonances exist [29]. However, we restrict the experiments to the visible spectral region, where only the first TE and TM guided mode with $m = 0$ can be excited. We refer to them as TE_0 and TM_0 mode.

The modes in such a configuration are characterized by a wavevector $\mathbf{k}$ with $k = \sqrt{k_x^2 + k_y^2}$ and an energy $E(k)$. With the dielectric constants of the waveguide layer and the substrate, the dispersion of the guided modes can be calculated with the *empty-lattice approximation* [29]. Here, the slab structure is assumed to consist of homogeneous layers. Possible distortions of the homogeneity like grating couplers (see below) are taken into account as a modification of the dielectric constant of the corresponding layer. $E(k)$ is given by the solutions of the transcendental equations

$$\tan(\bar{\beta} L_z) = \frac{\bar{\beta}(\beta_S + \beta)}{\bar{\beta}^2 - \beta_S \beta} \tag{2.24}$$

for TE modes and

$$\tan(\bar{\beta} L_z) = \frac{\epsilon_M \bar{\beta}(\beta_S + \epsilon_S \beta)}{\epsilon_S \bar{\beta}^2 - \epsilon_M^2 \beta_S \beta} \tag{2.25}$$

for TM modes [30]. Here, $k = \sqrt{k_x^2 + k_y^2}$, $k_0 = \omega/c = E/(\hbar c)$, $\beta = \sqrt{k^2 - k_0^2}$, $\beta_S = \sqrt{k^2 - \epsilon_S k_0^2}$ and $\bar{\beta} = \sqrt{\epsilon_M k_0^2 - k^2}$. Often, a different version of this equation containing the same information is found in literature

$$\begin{aligned} 2d\sqrt{\omega^2\epsilon_M/c^2 - k^2} &= \arctan\left(A\sqrt{\frac{\omega^2(\epsilon_f - \epsilon_c)/c^2}{\omega^2\epsilon_f/c^2 - k^2} - 1}\right) \\ &+ \arctan\left(B\sqrt{\frac{\omega^2(\epsilon_f - \epsilon_s)/c^2}{\omega^2\epsilon_f/c^2 - k^2} - 1}\right) \end{aligned} \tag{2.26}$$

with $\omega = E/\hbar$, $A = B = 1$ for TE polarization and $A = \epsilon_M/\epsilon_c$ and $B = \epsilon_M/\epsilon_s$ for TM polarization [29]. Equation (2.26) is used in Chapter 5 to determine the dispersion $E(k)$ of the quasiguided mode. It can be seen that for an asymmetric waveguide layer ($\epsilon_M \neq \epsilon_C$) only modes above a certain frequency can be guided. This cut-off frequency is given by

$$\omega_m^{(Cutoff)} = \frac{c_0}{L_z\sqrt{\epsilon_M - \epsilon_S}}\left(\arctan\left(\sqrt{\frac{\epsilon_S - \epsilon_C}{\epsilon_M - \epsilon_S}}\right) + m\pi\right) \tag{2.27}$$

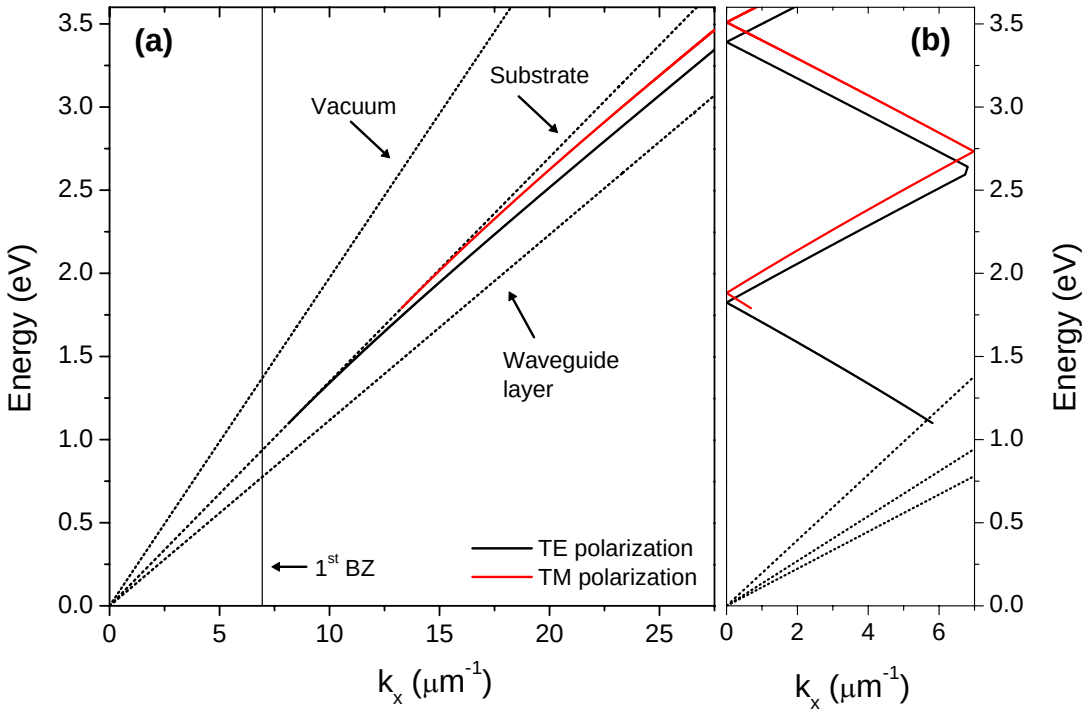

Figure 2.5: Waveguide dispersion calculated with the empty-lattice approximation. (a) Dispersion for a guided mode, (b) dispersion for a quasiguided mode. The parameters of the calculation are: $\epsilon_{Substrate} = 2.14$, $\epsilon_{ITO} = 3.2$, ITO thickness 140 nm, period $d_x = 450$ nm. The slight discontinuity in (b) for TE polarization is a numerical artefact.

with c_0 the vacuum speed of light [31]. For simplicity we assume the propagation direction to be along the x-axis with $k = k_x$ (see Fig. 2.4). Typical dispersions of guided modes for TE and TM polarization are shown in Fig. 2.5(a) together with the light lines of vacuum, substrate, and medium. These are given by the propagation of light in a medium with dielectric constant ϵ as

$$E = \frac{\hbar c_0}{\sqrt{\epsilon}} k_x. \tag{2.28}$$

To be able to excite a guided mode, energy, momentum and polarization of the incoming light field have to be conserved [32]. As can be seen from Fig. 2.5(a), the dispersion of the guided modes lies below the vacuum light line and below the substrate line. For a given k_x, the energy $E(k_x)$ of the guided mode is always smaller than the energy of light fields coming from substrate or vacuum. This means that it is not possible to directly excite a guided mode in a waveguide layer by light beams coming from the surrounding of the waveguide. Two methods are usually employed to overcome this problem. Both make use of changing the momentum of the incoming light field. A prism coupler excites an evanescent field that is coupled into the waveguide [33]. This field has an additional

momentum that prevents the violation of momentum conservation. Another possibility is to use a grating coupler [34]. This introduces a periodic surface corrugation with period d_x on the waveguide medium that adds a momentum $K_\pm = \pm 2\pi/d_x$ to a given k_x. Both methods allow to work above the light line and to couple directly to a guided mode. In the following, we will make use of grating couplers to excite modes inside the waveguide layer.

Introducing a periodic surface corrugation to the waveguide layer can be interpreted as a folding of the dispersion from the empty-lattice approximation into the first Brillouin zone (BZ) with boundaries at $\pm\pi/d_x$. The grating allows to couple the guided modes to the photon continua in the surrounding [30]. The modes in such systems are therefore no longer purely guided but loose energy through radiation into the surrounding. They are called leaky or *quasiguided modes*. The dispersions for both the pure waveguide layer and for one with a periodic surface corrugation with period d_x are shown in Fig. 2.5. Due to the periodic surface corrugation on top of the waveguide layer, the dispersion of the quasiguided mode consists of allowed bands that are separated by stop-bands. These stop-bands do not appear in the results of the empty-lattice approximation because it does not include an interaction between different quasiguided modes (see next section).

Such a quasiguided mode is characterized in transmission experiments by a highly asymmetric Fano resonance [28, 35, 36]. This form was first found in atomic systems, when a configuration with discrete levels couples to a continuum of states via a mutual ground level [37]. The interference of the discrete state with the continuum gives rise to this characteristic asymmetric absorption resonance. In our system, the discrete levels are formed by the quasiguided modes. Because of their long lifetimes, they have a high quality factor Q of typically a few 1000 [28] and hence a small bandwidth, similar to discrete systems. The quasiguided mode then couples to the directly transmitted light, a fact that causes the asymmetric resonance [36]. The resonance form of the quasiguided mode can be described by a Fano-type lineshape [9]:

$$\alpha^{TE}(E) = -\ln(T) = I\frac{\left(\frac{2(E-E_0)}{\gamma} + q\right)^2}{\left(\frac{2(E-E_0)}{\gamma}\right)^2 + 1} \tag{2.29}$$

(see [37]). The parameters I and E_0 determine amplitude and energy of the resonance, respectively. The interaction of discrete and continuum states is given by γ, q describes the transition probability of a given state into a discrete or a continuum state. γ and q are responsible for shape and width of the asymmetric resonance. Typical extinction spectra ($-\ln(T)$, T: transmission) of quasiguided modes are plotted in Fig. 2.6 for different periods d_x, the data were taken from [9]. A 140 nm thick ITO-layer on a quartz substrate acted as waveguide layer. A grating coupler that consisted of a periodic arrangement of gold nanowires on top of the ITO layer excited the quasiguided mode inside the ITO. The period d_x of the grating was increased in steps of 25 nm from 375 nm to 575 nm. The light polarization was oriented along the wires (TE polarization). For such a polarization, no

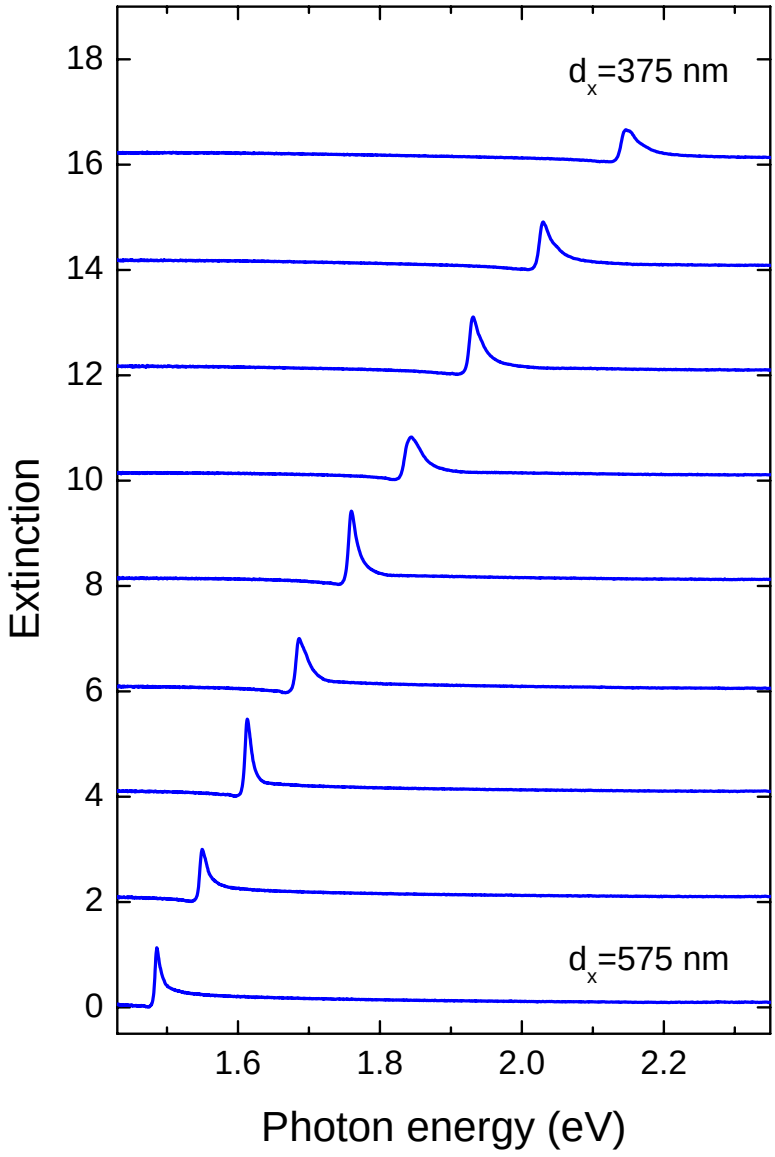

Figure 2.6: Measured extinction ($-\ln(T)$, T: transmission) of a metallic photonic crystal slab consisting of a 1-dim gold grating on top of an ITO layer. The spectra were taken for TE polarization (polarization along the wires), the period d_x was increased from 375 nm to 575 nm. The individual spectra are shifted upwards for clarity. Data taken from [9].

resonances within the metallic nanowires are excited [35]. For each period a single sharp resonance at a specific energy is excited. Its highly asymmetric form is of the typical Fano form, see Eqn. (2.29). As expected, a variation of the period shifts the resonance peak of the quasiguided mode, according to the dispersion $E(k = 2\pi/d_x)$.

Varying the angle of incidence φ reveals some further insight into the physics of quasiguided modes. For an oblique angle, a quasiguided mode changes its energy and splits

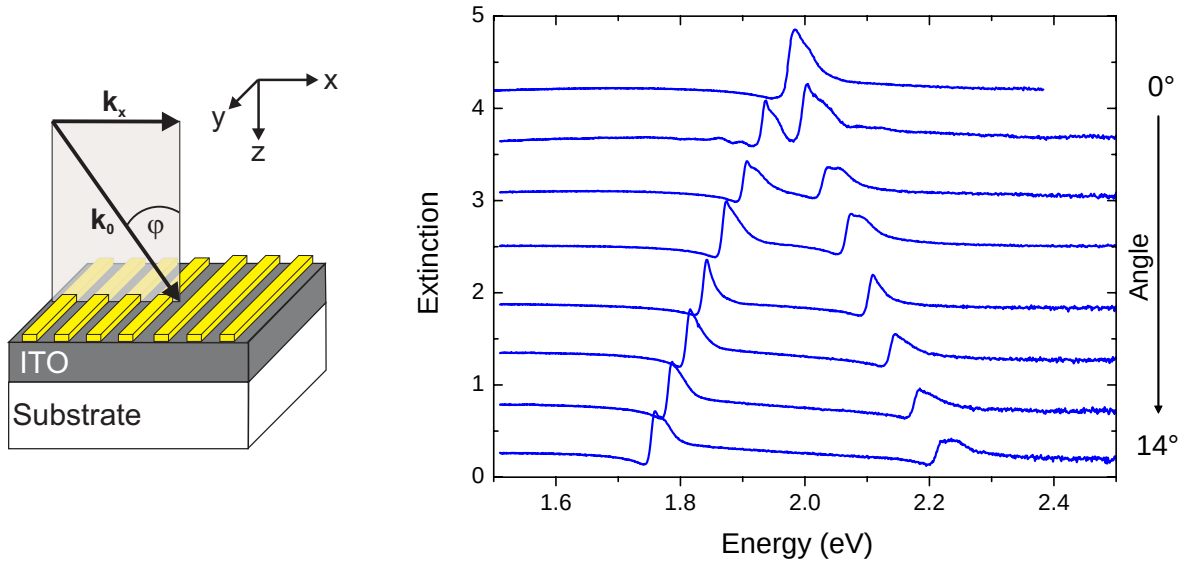

Figure 2.7: Left panel: sketch of the angle-resolved measurement with angle of light incidence φ. Right panel: Angle-resolved extinction spectra in TE polarization. The individual spectra are shifted upwards for clarity.

into two spectral resonances, see Fig. 2.7. Increasing the angle of incidence separates these two resonances further in energy [30, 35, 38]. Symmetry reasons are responsible for the non-appearing of the second resonance at normal light incidence. It was shown, that the quasiguided mode in slab structures is degenerated at the center of the first BZ ($k_x = 0$) [35]. We find a symmetric and an antisymmetric mode. Thus, only the symmetric mode can interact with the incoming symmetric light field, the antisymmetric mode is not excited [38]. Changing the angle of light incidence and hence varying k_x allows to move away from the center of the first BZ. Symmetric and antisymmetric mode both become visible in the spectrum and can be probed by angle-resolved measurements. Their energies are determined by the dispersion of the quasiguided mode. From this dispersion it becomes clear that increasing k_x leads to an excitation of the modes at different energies, their separation becomes larger for increasing k_x, see Fig. 2.5(b).

2.3 Coupling of plasmon and waveguide mode

In this chapter we are concerned with the compound system of particle plasmons and quasiguided mode. It was found that in such systems the optical resonances can be tailored by an appropriate design of the sample geometry [8]. Arranging the metallic nanostructures periodically on top of the waveguide material acts as a grating coupler: an incoming light field can excite a quasiguided mode in the waveguide layer. Additionally, particle plasmons inside the nanostructures are excited by the incoming light field. The electrical and the optical resonances (particle plasmon and quasiguided mode) can couple strongly to form a new quasi-particle, a so-called *plasmon-waveguide-polariton* [9]. This

polariton shows interesting properties such as a pronounced bandstructure, large coupling energies of up to 30 meV [9], and enhanced dephasing times [39]. Especially an enhanced transmission inside the plasmon resonance was observed [8]. In the following, this coupled system will be explained in more detail.

The dispersion of the coupled system of particle plasmon and waveguide mode can be calculated with an effective Hamilton operator H given in [9]. We start the calculation by assuming that the wavefunction Ψ of the polariton is constructed of the wavefunctions of the symmetric and antisymmetric quasiguided mode (φ_1 and φ_2) and of the wire plasmon (φ_{Pl}). The stationary Schrödinger equation is given by

$$H\Psi = \begin{pmatrix} H_{11} & H_{12} & H_{13} \\ H_{21} & H_{22} & H_{23} \\ H_{31} & H_{32} & H_{33} \end{pmatrix} \begin{pmatrix} \tilde{\varphi}_1 \\ \tilde{\varphi}_2 \\ \tilde{\varphi}_{Pl} \end{pmatrix} = E \begin{pmatrix} \varphi_1 \\ \varphi_2 \\ \varphi_{Pl} \end{pmatrix}. \tag{2.30}$$

The non-diagonal components describe the interaction of the quasiguided modes and the plasmon. H_{12} and H_{21} describe the coupling of the two quasiguided modes, H_{13} and H_{31} the coupling of the symmetric quasiguided mode with the plasmon, and H_{23} and H_{32} the interaction of plasmon and antisymmetric quasiguided mode.

We have to distinguish between two cases: normal ($k_x = 0$) and non-normal ($k_x \neq 0$) light incidence. Near the center of the first Brillouin zone, H can be replaced by an effective Hamiltonian [9]. It describes the situation for non-normal light incidence, i.e. $k_x \neq 0$:

$$H_{eff} = \begin{pmatrix} E(K_+ + k_x) & V_1 & V_2 \\ V_1 & E(K_- + k_x) & V_2 \\ V_2 & V_2 & E_{Pl} \end{pmatrix}. \tag{2.31}$$

Here, $E(k)$ are the energies of the bare TM_0 guided modes with momenta $K_\pm + k_x$, E_{Pl} is the energy of the individual wire plasmons, V_1 is the stop-band half-width in the 1-dim photonic crystal slab (see previous section), and V_2 is the coupling energy of quasiguided mode and wire plasmon. Near $k_x = 0$, $E(K_\pm + k_x)$ can be replaced by a linear function. At $k_x = 0$ the TM_0 modes have the energy E_0, and the slope of the dispersion is given by the group velocity $\tilde{c}$. We get $E(K_\pm + k_x) \approx E_0 \pm \tilde{c}k_x$.

This Hamiltonian describes an ideal system. In our structures, however, the light is absorbed by the metal and the guided modes are lossy due to the periodic surface corrugation. Taking this into account leads to a modified Hamiltonian for the polaritonic system. The absorption introduces finite half-widths to the resonances of plasmon and guided modes. With Γ as half-width of the plasmon, its energy E_{Pl} is replaced by $E_{Pl} - i\Gamma$. The same holds for the quasiguided modes, whose half-width γ modifies their energies to $E_0 \pm \tilde{c}k_x - i\gamma$. In [30], the radiative losses of the quasiguided modes are modelled with a complex photonic band gap. With γ_1 being the radiative damping, V_1 is replaced by $V_1 - i\gamma_1$.

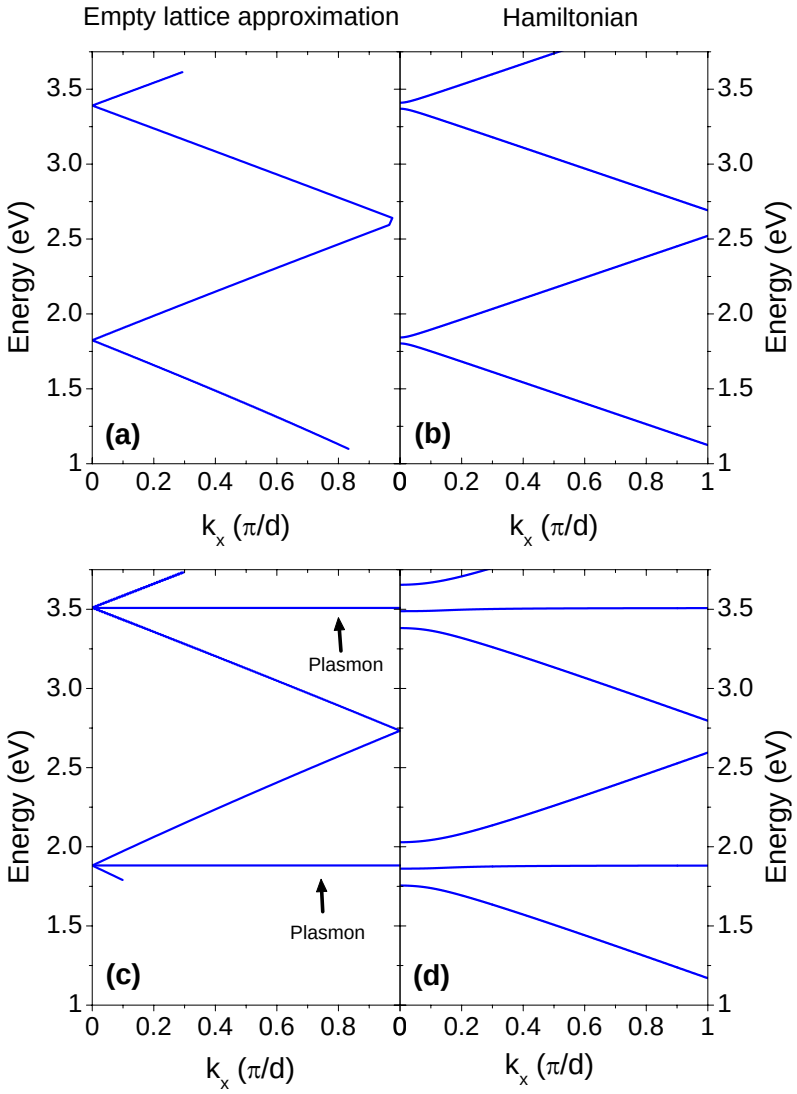

Figure 2.8: Dispersion $E(k_x)$ calculated for non-normal light incidence with the empty-lattice approximation and by diagonalizing the polariton Hamiltonian. (a) and (b) for TE polarization, (c) and (d) for TM polarization. (a) and (c) show $E(k)$ in the empty-lattice approximation, (b) and (d) in the polariton-type model. The period d was 450 nm.

Using these modifications, we end up with a non-Hermitian matrix for describing the energies of the polariton:

$$H_{eff} = \begin{pmatrix} E_0 + V_1 - i(\gamma + \gamma_1) & \tilde{c}k_x & \sqrt{2}V_2 \\ \tilde{c}k_x & E_0 - V_1 - i(\gamma - \gamma_1) & 0 \\ \sqrt{2}V_2 & 0 & E_{Pl} - i\Gamma \end{pmatrix}. \tag{2.32}$$

The energies $E(k_x)$ of the polariton systems are plotted in Fig. 2.8(b) and (d) in comparison with the results obtained with the empty-lattice approximation [(a) and (c)]. Furthermore, (a) and (b) show the dispersion in TE polarization, (c) and (d) in TM polarization. The TM case in empty-lattice approximation additionally contains the flat

dispersion of wire plasmon resonances at 1.88 eV and 3.51 eV as an example. Due to the non-interaction between photonic and electronic resonances in this model, the center of the first BZ shows threefold degenerated bands at the plasmon energies in TM polarization. In the simple polariton picture, this degeneracy is lifted as well as the twofold degeneracy in TE polarization, giving raise to bands separated by gaps.

The parameters in the polariton simulation are: $E_0^{TM}, E_0^{TE}, E_{Pl} = 1.882, 1.823, 1.882$ eV for the bands at 1.88 eV and $E_0^{TM}, E_0^{TE}, E_{Pl} = 3.508, 3.390, 3.508$ eV for the bands at 3.51 eV. The other parameters were chosen according to [9] to be $\Gamma, \gamma, \gamma_1, V_1, V_2 = 100$, 20, 5, 20, 100 meV and $\tilde{c} = 10^{-4}$ meV·m.

As discussed above, for normal light incidence ($k_x = 0$) only the symmetric quasiguided mode can be excited, the antisymmetric mode is not visible in the optical properties. In Eqn. (2.30), we get $\varphi_2 = \tilde{\varphi}_2 = 0$, the same holds for the coupling coefficients H_{12}, H_{21}, H_{23}, and H_{32}. Equation (2.30) can then be reduced to the simple form

$$H\Psi = \begin{pmatrix} H_{11} & H_{13} \\ H_{31} & H_{33} \end{pmatrix} \begin{pmatrix} \tilde{\varphi}_1 \\ \tilde{\varphi}_{Pl} \end{pmatrix} = E \begin{pmatrix} \varphi_1 \\ \varphi_{Pl} \end{pmatrix}, \tag{2.33}$$

that connects the wavefunctions of the symmetric quasiguided mode φ_1 and of the particle plasmon φ_{Pl}. We get a coupling of only these two resonances. The non-Hermitian

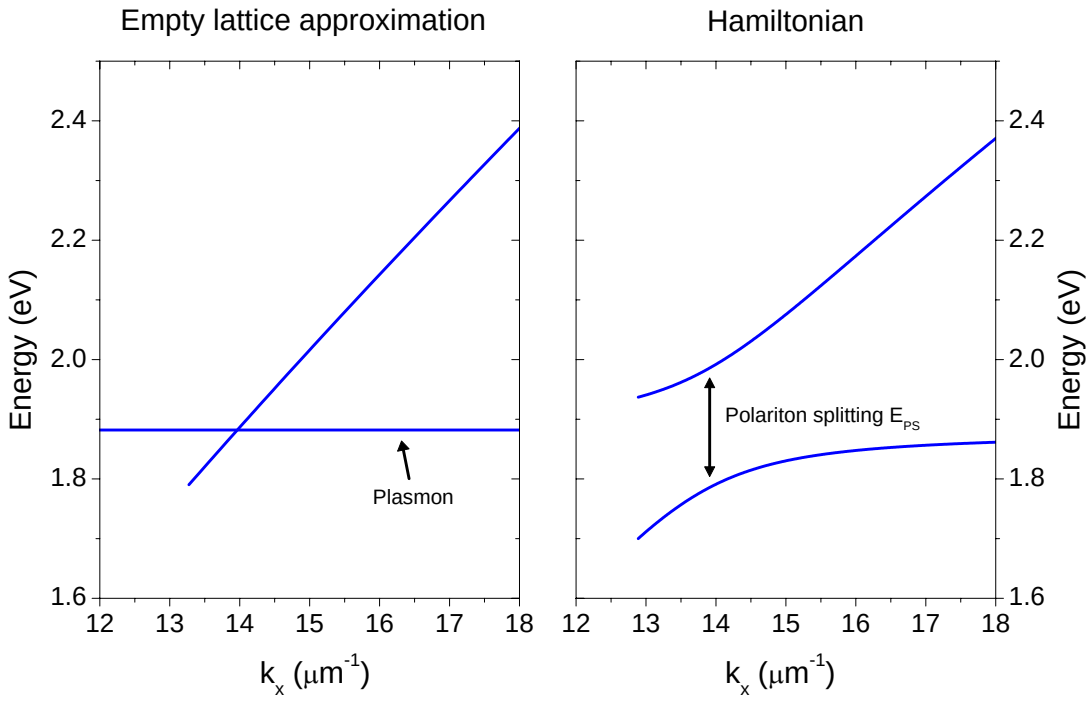

Figure 2.9: Dispersion $E(k)$ calculated for normal light incidence with the empty-lattice approximation and by diagonalizing the polariton Hamiltonian. The parameters are as in Fig. 2.8.

matrix for the case $k_x = 0$ reads as:

$$H_{eff} = \begin{pmatrix} E_0 & V_2 \\ V_2 & E_{Pl} \end{pmatrix}. \tag{2.34}$$

The dispersion $E(k)$ reveals a basic property of the plasmon-waveguide-polariton, see Fig. 2.9. Changing the period of the slab structure allows to tune the electronic resonance into the photonic resonance and vice versa. In the $E(k)$-diagram, this effect can be deduced from the anti-crossing behavior of the polariton branches and the polariton splitting E_{PS} as the minimum energy separation between the branches (see Fig. 2.9). In the empty-lattice approximation, where a coupling was not included, the dispersions of particle plasmon and quasiguided mode cross at a specific momentum and energy. This degeneracy is lifted when calculating $E(k)$ by solving Eqn. (2.33) with Eqn. (2.34). The splitting E_{PS} between the bands is determined by the coupling parameter V_2.

Measuring the optical properties of such compound structures reveals interesting spectral resonances. In the following, we will focus on metallic *nanowires* on top of an ITO layer. It was found that in such systems the extinction ($-\ln(T)$, T: transmission) depends strongly on the polarization of the incoming light [9]. In TM polarization, the light is polarized perpendicular to the nanowires. Particle plasmon and symmetric quasiguided mode are excited simultaneously and form the polariton. Two resonances appear in the extinction spectrum, as presented in Fig. 2.10 (taken from [9]). One resonance can be attributed to the plasmonic branch of the polariton, the other polariton branch is the excited quasiguided mode. Changing the period d_x of the metallic grating allows to tune the photonic resonance into the optical resonance and vice versa according to the dispersion $E(k)$ [9]. For a period of 375 nm, the lower polariton branch shows the characteristic plasmon form, while the upper branch has the Fano form of the quasiguided mode. However, increasing the period changes the appearance of both branches. The plasmonic branch resonance becomes less intense and shifts to lower energies, for a period of 575 nm it has completely transformed into the quasiguided mode part of the polariton. Contrary, the upper polariton branch becomes plasmonic-like. For a polarization along the wires (TE polarization), only the TE quasiguide mode is excitable, no polariton is formed. The extinction spectra for this configuration were already discussed in Fig. 2.6. Varying the angle of light incidence excites symmetric and antisymmetric quasiguided mode simultaneously. Both can couple strongly to the plasmonic resonance in TM polarization, the extinction spectra reveal three peaks [9]. Angle-resolved extinction measurements allow to probe the dispersion $E(k_x)$ of the polariton (see Fig. 2.8).

Due to the polariton formation in such metallic photonic crystals, the extinction spectra in TM polarization show rather complex resonance forms. The lineshape of the resonances at normal light incidence can be modeled by a coupled oscillator model [40]. Here, the particle plasmon resonance is described by a Lorentz oscillator that couples to the Lorentz-type quasiguided mode resonance. Starting from the equations of motion of two

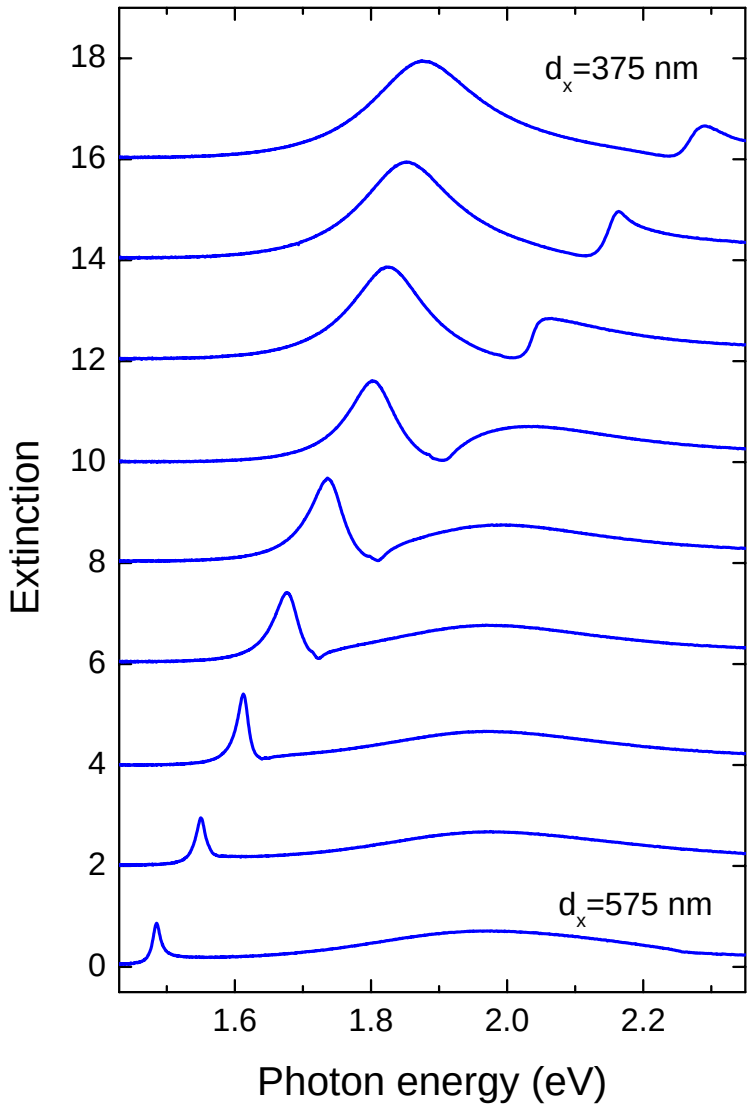

Figure 2.10: Measured extinction ($-ln(T)$, T: transmission) of a metallic photonic crystal slab consisting of a 1-dim gold grating on top of an ITO layer. The spectra were taken for TM polarization, the period d_x was increased from 375 nm to 575 nm. The individual spectra are shifted upwards for clarity. Data taken from [9].

coupled harmonic oscillators, the absorption coefficient is given by

$$\alpha^{TM}(\omega) = \alpha_{Pl} \frac{4\gamma_{Pl}^2\omega^2\left[\omega^2 - \Omega_{WG}^2 - (q_{WG}/q_{Pl})\Omega_C^2\right]^2}{\left[(\omega^2 - \Omega_{Pl}^2)(\omega^2 - \Omega_{WG}^2) - \Omega_C^4\right]^2 + 4\gamma_{Pl}^2\omega^2(\omega^2 - \Omega_{WG}^2)^2}. \tag{2.35}$$

α_{Pl} is the maximum absorption coefficient of the uncoupled plasmon oscillation. The resonance frequencies, the (homogeneous) half widths at half maximum, and the oscillator strengths of the uncoupled system are denoted by Ω_j, γ_j, and q_j (j = Pl, WG),

respectively. Ω_C^2 represents the coupling strength between the oscillators. We will use Eqn. (2.29) and Eqn. (2.35) to describe and calculate several lineshapes in TE and TM polarization later on.

So far, we considered only a single quasiguided mode to couple with the particle plasmon (at normal light incidence with $k_x = 0$). We have seen in Chapter (2.2) that a waveguide layer supports an infinite number of TE and TM quasiguided modes. In principle, each of these TM quasiguided modes can couple to the plasmon and to all other modes. Therefore, we can extend Eqn. (2.33) to describe a coupled system consisting of a single plasmon and an infinite number of TM quasiguided modes. Each mode is defined by a momentum k and energy $\epsilon(k)$. With the wavefunctions φ_{Pl} of the plasmon and φ_i of the i-th mode, the stationary Schrödinger equation for describing the system can be written as

$$H\Psi = \begin{pmatrix} \epsilon_{Pl} & V_{Pl,1} & V_{Pl,2} & V_{Pl,3} & \cdots \\ V_{1,Pl} & \epsilon_1 & V_{1,2} & V_{1,3} & \cdots \\ V_{2,Pl} & V_{2,1} & \epsilon_2 & V_{2,3} & \cdots \\ \vdots & \vdots & \ddots & \ddots & \ddots \end{pmatrix} \begin{pmatrix} \tilde{\varphi}_{Pl} \\ \tilde{\varphi}_1 \\ \tilde{\varphi}_2 \\ \vdots \end{pmatrix} = E \begin{pmatrix} \varphi_{Pl} \\ \varphi_1 \\ \varphi_2 \\ \vdots \end{pmatrix}. \tag{2.36}$$

The coupling between the plasmon and the i-th quasiguided mode is given by $V_{Pl,i}$ and $V_{i,Pl}$, the coupling between the i-th and j-th mode is expressed by V_{ij} and V_{ji}. These parameters correspond to V_2 and V_1 in Eqn. (2.32), respectively. The energies ϵ_i follow the dispersion of the quasiguided TM mode. This Schrödinger equation is the generalized form of Eqn. (2.33), presented above. It includes Eqn. (2.34) as special case with $\epsilon_i = V_{i,k} = V_{k,i} = V_{Pl,i} = V_{i,Pl} = 0$ for $i \neq 1$, except for a single resonance at $\epsilon_1 = \epsilon(2\pi/d_0)$. Hence, only a single quasiguided mode is excited that interacts with the plasmon. Equation (2.36) is extendable in a similar way for the case of non-normal light incidence, where both symmetric and antisymmetric quasiguided mode are excitable, see Eqn. (2.32). However, in a configuration where the quasiguided mode is excited by a perfect grating coupler, usually only a single mode couples to the continuum of the incoming light field. As a result, in a system with a perfect grating on top of the waveguide layer we will deal with Eqn. (2.33) rather than with Eqn. (2.36). However, we will see that the last equation can be used to describe disordered systems.

2.4 Introduction to disorder

2.4.1 Perfectly ordered systems

When talking about disorder we always deal with deviations from a perfectly ordered system. Crystals show the highest degree of order in nature (except for vacuum) [41]. As

perfect systems are necessary for introducing disorder, we will start this section with a description of perfect crystals.

A crystal consists of two contributions: a *lattice* and a *basis* [16]. The lattice is simply a regular periodic array of points in space. It is defined by three fundamental translation vectors $\mathbf{a}_1$, $\mathbf{a}_2$, $\mathbf{a}_3$. The periodic arrangement is identical in all directions when viewed from points $\mathbf{r}$ and $\mathbf{r}'$ that are defined by

$$\mathbf{r}' = \mathbf{r} + \mathbf{l} = \mathbf{r} + u_1\mathbf{a}_1 + u_2\mathbf{a}_2 + u_3\mathbf{a}_3. \tag{2.37}$$

The parameters u_1, u_2, and u_3 are arbitrary integers. The set of points $\mathbf{r}'$, as defined by Eqn. (2.37) for all u_1, u_2, and u_3, defines the lattice. Hence, any two lattice points are connected by a lattice vector

$$\mathbf{l} = u_1\mathbf{a}_1 + u_2\mathbf{a}_2 + u_3\mathbf{a}_3. \tag{2.38}$$

In a perfectly ordered crystal, all observable quantities $F(\mathbf{r})$ must obey the translational operation

$$F(\mathbf{r}) = F(\mathbf{r} + \mathbf{l}) \tag{2.39}$$

for all lattice vectors $\mathbf{l}$ and for any $\mathbf{r}$. Equation (2.39) plays a crucial role in the physics of crystals. It specifies the quantity $F(\mathbf{r})$ to be invariant under a translation. Hence, $F(\mathbf{r})$ is a periodic function of $\mathbf{r}$. F could be the charge concentration, the electron number density, or the magnetic moment density. The volume defined by $\mathbf{a}_1$, $\mathbf{a}_2$, $\mathbf{a}_3$ is called a cell. A primitive cell is a cell with minimum volume, the corresponding translation vectors are the primitive translation vectors.

The basis is defined as a group of atoms that belongs to exactly one lattice point in space. In perfect crystals, every basis is identical in composition, arrangement and orientation. It can consist of $s = 1, 2, \ldots$ atoms, it is not necessarily restricted to a single atom. The positions of the atoms are given by

$$\mathbf{r}_j = x_j\mathbf{a}_1 + y_j\mathbf{a}_2 + z_j\mathbf{a}_3, \tag{2.40}$$

with x, y, and z between 0 and 1 and $j = 1, 2, \ldots s$. Additionally, the basis can be composed of different atoms or molecules. An example is sodium chloride (salt) whose basis consists of a pair of single Na^+ and Cl^- ions.

With these definitions, we can finally define the crystal as a basis attached to every point of the lattice. Typically, the crystalline structure can be carried into itself by symmetry operations such as translation, rotation and reflection. The crystal structure can be directly imaged by using scanning tunneling microscopy.

2.4.2 Types of disorder

The aim of this section is to present different disorder types. Several examples illustrate the different types. However, they are just a small representation and numerous other important examples are not mentioned. They can be found in special literature on disorder, see e.g. [41, 42].

The appearance of disorder in a system means deviations in any form from the perfect system. This deviation is connected with the breaking of symmetry [41]. One class of disorder is the *cellular disorder*, where the physical properties are varied from cell to cell while the lattice is perfectly orderer [41]. This happens in systems where the configuration of the cells is not identical. In some cells the atoms are replaced by atoms from a different type (defects) or by vacancies. When the replaced atoms do not form a regular lattice by themselves, the system is said to have *substitutional disorder* which is a special type of cellular disorder. Looking at Eqn. (2.39) it becomes clear that the composition of the cells is no longer invariant under a translation operation. This disorder type is of great technical interest due to the possible formation of defect states within energy bandgaps. For example, adding doping atoms into semiconductors is used to fabricate n- and p-doped materials [43].

A different type of cellular disorder is *magnetic disorder*. Here, the disorder is not related to the kind of the atoms but to their spins. Usually, the l-th site of a regular crystal carries a magnetic moment that is related to a localized spin variable. In systems with magnetic disorder, this moment varies randomly from site to site. As a result, macroscopic effects such as ferromagnetism, antiferromagnetism, and paramagnetism can include magnetic disorder on a microscopic scale due to thermal fluctuations [41].

In real systems however, perfect cellular disorder is rarely achieved. Usually, interactions between neighboring cells occur that affect the disordered physical property (magnetic moment, defects, etc.) in the system. As a result, the disordered properties on neighboring lattice sites are not completely independent. They are rather correlated which introduces an order on a short length-scale (so-called short-range order) within the disordered system. A typical example are the Bloch walls in ferromagnetism. They form regions in a crystal that separate domains magnetized in different directions. Correlation effects cause the change of the corresponding spin orientations not to happen in a discontinuous jump from one lattice point to the next. The spin rather changes gradually in a number of steps over many atomic planes [16].

A disorder class that is different from cellular disorder is given in systems, where the cells are identical but the lattice deviates from perfect order. The spatial arrangement of the cells can no longer be described by Eqn. (2.37). This type of disorder is called *positional disorder*. Figure 2.11 shows a comparison of cellular and positional disorder, where the cells and the lattice are disordered, respectively. In this work, we will focus on positional disorder. Positional disorder can appear in a lot of different configurations. A classical example is given in hot solids whose atoms move around their equilibrium

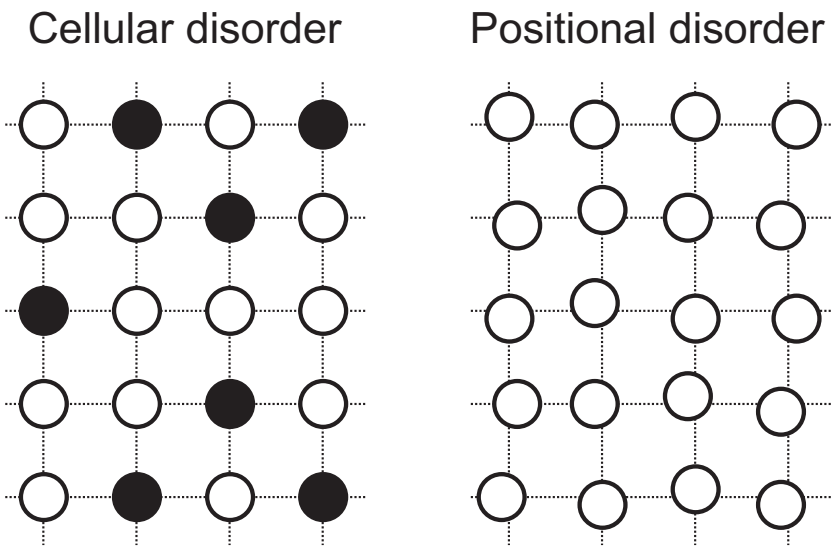

Figure 2.11: Cellular and positional disorder. In cellular disorder, the cells (white) can contain different kinds of atoms or molecules (here: black), the cells are located at the perfect lattice. In systems with positional disorder, identical cells are no longer arranged on the perfect lattice.

positions due to thermal fluctuations [16]. These lattice vibrations are called phonons and play a crucial role e.g. in semiconductor physics [44]. Looking at them in more detail reveals their close relation with the perfect lattice. The lattice vibrations originate from the perfect lattice by simple shifts of the atomic positions. Therefore, the positions of the lattice points shifted by phonons and the perfect lattice are topologically identical. Phonons leave the crystal topologically ordered. This is not the case in materials with topological disorder. In such systems, the disordered lattice can not be transformed into an ordered system by means of topological operations [41]. Topological disorder appears in amorphous materials, in liquids, or in systems with dislocations where complete cells are missing. Another example for topological disorder are solids with microcrystalline disorder. Different regions of these crystals show perfect order according to Eqn. (2.39). Their boundaries, however, are shifted with respect to each other causing Eqn. (2.39) not to be applicable to the total crystal. A different class of materials with positional disorder are quasicrystals [45]. They are materials whose crystal lattice is both periodic and amorphous simultaneously. While quasicrystals show ordering on a local scale, their global structure is aperiodic. Hence, their lattice is a combination of solids and liquids, and we classify them to have both topological order and topological disorder. It should be noted that 1-dim systems can never show topological disorder [41]. It is always possible to transform such systems by topological operations into ordered systems.

Figure 2.12 presents the discussed classification of disorder with the mentioned exam-

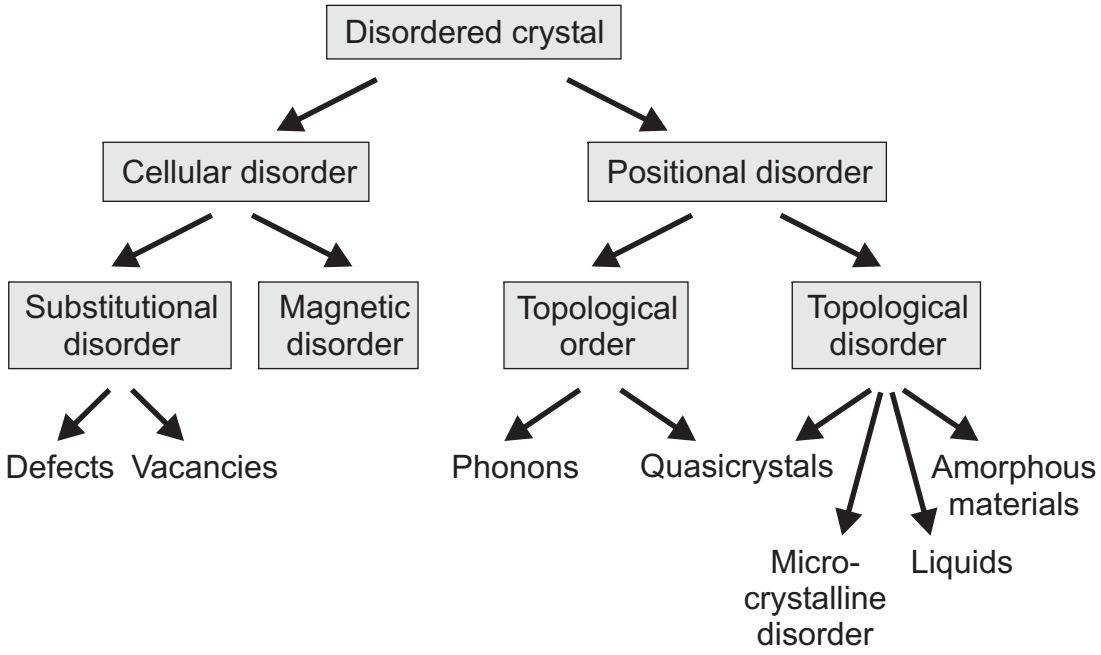

Figure 2.12: Overview about the presented disorder classification.

ples as an overview. In the following, we will deal with excitations in disordered systems and introduce the important aspect of localization.

2.4.3 Excitations in disordered systems

The considerations presented in this section follow the book of Ziman [41]. We will start with a 1-dim system and then discuss results for a 3-dim system. A 1-dim linear chain serves as model system for describing disorder. The calculation of the excitations of such chains is done by determining eigenvalues and eigenfunctions of the Hamiltonian that describes the system. In general, ones solves the equations

$$(\varepsilon_l - \lambda)u_l + \sum_{l' \neq l} V_{ll'} u_{l'} = 0, \tag{2.41}$$

with ε_l and $V_{ll'}$ as diagonal and off-diagonal matrix elements of the Hamiltonian, respectively, λ as spectral variable, and u_l as the amplitude of the excitation. The variable $l = 1 \ldots N$ runs over the N sites of the chain. Possible disorder in the system affects the elements of the Hamiltonian. For anisotropic systems, the system consists of different states with different energies. Such systems show disorder in the energies ε_l or so-called *site-diagonal disorder*. Disorder in the interaction energy of different states is apparent in *off-diagonal disorder*, that affects $V_{ll'}$. Depending on the considered system, λ stands for the frequency of phonons, for the quantized energy $\hbar\omega$ of a magnon or exciton, for the energy ε of an electron eigenstate, or for some other excitation. It is a big advantage

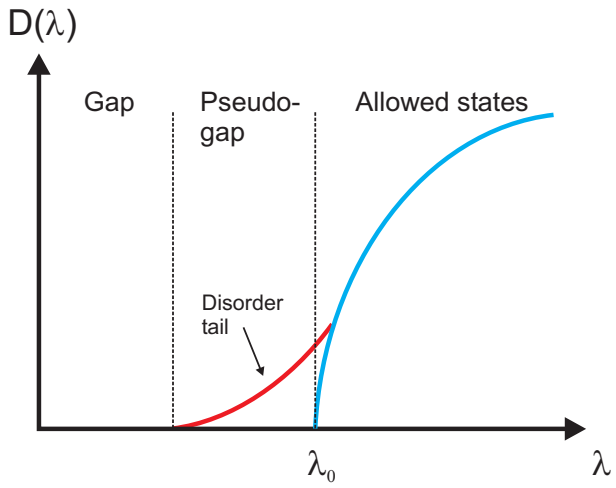

Figure 2.13: Density of states $D(\lambda)$. The scheme shows the allowed states in a perfectly ordered system, the disorder-induced tail in the pseudo-gap region, and the gap.

of this formalism that it can be used for many different situations. Equation (2.41) can be solved easily for perfectly ordered systems by using the Bloch theorem. This theorem states that the eigenfunctions $\psi(\mathbf{r})$ of the wave equation for a periodic potential are plane waves whose amplitudes $u_k(\mathbf{r})$ contain the periodicity of the potential:

$$\psi(\mathbf{r}) = u_k(\mathbf{r}) \exp(i\mathbf{k} \cdot \mathbf{r}). \tag{2.42}$$

Expanding the potential into a Fourier series and using the Bloch theorem yields

$$\left[(\varepsilon_0 - \lambda) + \sum_{\mathbf{h}\neq 0} V(\mathbf{h}) e^{i\mathbf{q}\cdot\mathbf{h}}\right] U(\mathbf{q}) = 0. \tag{2.43}$$

As a result, we receive a typical band of states with energies

$$\lambda(\mathbf{q}) = \varepsilon_0 + \sum_{\mathbf{h}\neq 0} V(\mathbf{h}) e^{i\mathbf{q}\cdot\mathbf{h}}. \tag{2.44}$$

The spectrum of a perfect system consists of allowed excitation bands that are separated by gaps containing no allowed states. Introducing disorder modifies this spectrum. Typically, a transfer-matrix method with $V_{ll'}$ as next-neighbor interaction is used to determine the spectrum of disordered linear chains. Exponential tails at the allowed bands appear in the density of states that reach into the gap regions of the unperturbed system [46]. The density of states $D(\lambda)$ in the tails is no longer zero but relatively low, and the tail regions are therefore called pseudo-gaps. Such tails are e.g. the well-known Urbach-tails in semiconductors [43], for example in amorphous materials [47]. Figure 2.13 presents a scheme of the density of states where the disorder-induced tail appears in the gap, creating a pseudo-gap.

It was found in such disordered 1-dim systems that all eigenfunctions and normal modes are localized [48]. As a consequence, no eigenfunction is allowed to propagate

through the system, as they are localized to certain regions of the chain from where the amplitudes decay exponentially in all directions. They are even localized in spectral regions where the Bloch functions of an ordered system would be extended. This is a very strong observation in 1-dim systems and requires a closer look. In fact, one has to distinguish between eigenfunctions in the gap region, in the pseudo-gap region, and in the allowed bands. In the gap region, no extended waves can exist, the eigenfunctions decay exponentially along the chain. In the pseudo-gap region, the eigenfunctions are strongly localized. But within the allowed bands of the systems, the range of localization $1/\gamma(\lambda)$, where $\gamma(\lambda)$ is the localization constant, becomes very long and tends to the mean free path of a propagating excitations in the ordered system [49, 50]. In the disordered system, the eigenfunctions scatter at the deviations from perfect order.

The major advantage of the 1-dim linear chain is the possibility to calculate the eigenfunctions with the transfer-matrix method. The situation becomes more difficult for higher dimensional systems where Eqn. (2.41) reads as

$$(\varepsilon_{\mathbf{l}} - \lambda)u_{\mathbf{l}} + \sum_{\mathbf{l}' \neq \mathbf{l}} V_{\mathbf{l}\mathbf{l}'} u_{\mathbf{l}'} = 0. \tag{2.45}$$

Now, the site labels $\mathbf{l}$ and $\mathbf{l}'$ represent vectors and run over a regular lattice in real, 3-dim space. Typically, the Green function formalism is applied to solve the disordered problem [41]. It turns out that, like in the 1-dim system, disorder-induced exponential tails appear in the excitation spectrum. However, localization shows important differences to the 1-dim case. Again, the eigenfunctions themselves are no Bloch waves. The major difference to the eigenfunctions in the 1-dim case is that the eigenfunctions are localized only if the strength W of the disorder exceeds a certain critical value W_c. This fundamental property for the excitation of a lattice of more than one dimension is referred to as *Anderson-localization*. Anderson found that in the propagation of electrons a phase transition from the classical diffusion regime to localization occurs - the material becomes an insulator [51]. Similarly, light localization was observed theoretically and experimentally [52, 53], especially in photonic crystals [3]. The origin of this phenomenon is the constructive interference of waves that are scattered multiply at defects in the material. To explain the effect, we consider wave propagation inside a scattering medium (see Fig. 2.14). Starting at point A, a wave can be scattered multiply to follow a random path that causes the wave to return to this origin A. Therefore, the wave propagates on a closed loop. However, this loop can be followed in two directions. Two waves that propagate in opposite directions along this loop will acquire the same phase so that they can interfere constructively in point A. This interference leads to a higher probability that waves return to A instead of propagating away from it [52].

Localization due to disorder can only occur when the wave is scattered within the coherence length $l < 1/k$ being related to the wave number $k = 2\pi/\lambda$ and l as the

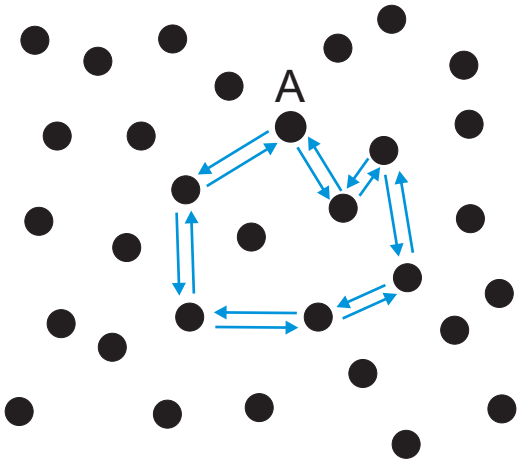

Figure 2.14: Localization in disordered media is caused by multiple scattering of waves. They propagate in opposite directions and interfere constructively in point A.

transport mean free path. This is the Ioffe-Regel criterion [54]

$$2\pi l < \lambda, \tag{2.46}$$

saying that in strongly scattering media the wave can not perform a single oscillation before it is scattered again. In terms of wave interference, this criterion is reasonable. Reducing the mean free path l increases the probability for such closed loop paths. If the scattering is strong enough, waves starting in point A can only follow closed loops and are localized. Moreover, it was discovered that the critical disorder strength W_c depends on the spectral variable λ. This means that propagating waves only occur for certain spectral regions, others are restricted to localized states. The regions are divided by so-called mobility edges, see Fig. 2.15. For absent disorder, all states are extended, no localization occurs. Disorder produces tails of localized states at the edges of the original band being separated by mobility edges from the still-existing extended states. Increasing disorder enlarges these tails, for a certain disorder amount the bands approach and melt together: no extended states are observable anymore.

Because the occurrence of localization is a wave interference phenomenon, it can occur for classical waves, for matter waves as well as for photons. As will be discussed in Chapter 5.8, correlations in the matrix that describes the system play an important role for the appearing of localization and can even lead to the vanishing of localization (delocalization).

One interesting consequence of the transition from extended to localized states is the vanishing of level-repulsion which is an energetical anticrossing effect. In systems with extended states, delocalized wavefunctions have a non-negligible spatial overlap. If the wavefunctions have (nearly) identical energies, the quasidegeneracy of the energies is lifted, resulting in bonding and antibonding combinations of the states, connected with

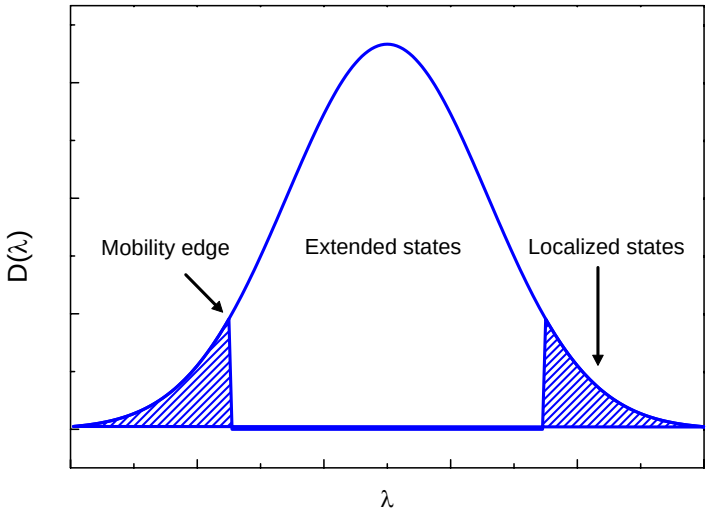

Figure 2.15: Density of states $D(\lambda)$, showing mobility edges separating extended and localized states.

a level splitting of the energy. This anticrossing of the energies is called level repulsion: the probability to find levels that are energetically nearby is reduced. Level repulsion was observed experimentally for example in semiconductors [55, 56]. The situation changes in disordered systems. Because the eigenfunctions are localized at different spatial positions, they do not spatially overlap, which means that the degeneracy of their energies will not be lifted. No level repulsion can be observed then. It was found that the energy level spacing function $P(S)$ experiences a transition from a Wigner distribution for extended states

$$P(S) = \frac{\pi}{2}\frac{S}{D^2}\exp(-\pi S^2/4D^2) \tag{2.47}$$

to a Poisson distribution for localized states

$$P(S) = \frac{1}{D}\exp(-S/D) \tag{2.48}$$

with S as energy level spacing between nearest levels and D as the mean energy spacing [57, 58]. These functions are plotted in Fig. 2.16. The crossover from Wigner to Poisson distribution in disordered system was explained with the localization of wave functions. As described above, this localization reduces their spatial overlap and hence the repulsion between the levels [57]. These distributions were used for example to describe the transition from metals to insulators [58].

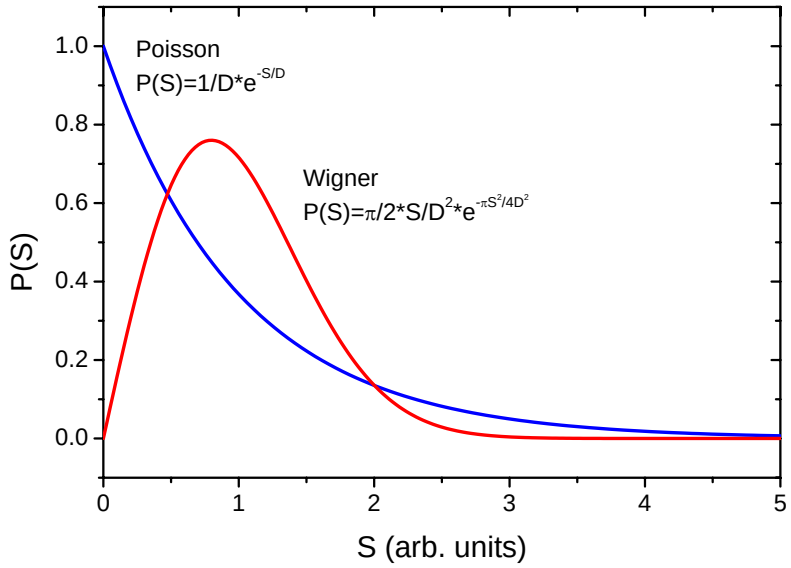

Figure 2.16: Wigner distribution [Eqn. (2.47)] and Poisson distribution [Eqn. (2.48)], showing the energy level spacing function $P(S)$ for localized and extended states, respectively.

Chapter 3

Experimental considerations

This chapter describes the fabrication of the metallic photonic crystal slab structures. Special demands are made for the processes that are necessary to fabricate such nanoscaled materials. Additionally, the experimental setup that was used to measure the optical properties of the samples is presented.

3.1 Sample fabrication

We consider metallic nanostructures that have a width of 100 nm and a height of 20 nm, and their distance is on the order of the wavelength of light. The nanostructures are deposited on top of a waveguide layer that has a typical thickness of 140 nm. For the disorder experiments, an indium-tin-oxide (ITO) layer on a quartz substrate was utilized as waveguide layer. This material is available from a number of companies in large amounts and at low cost (e.g. PGO or Laser Components). The group of Satyen K. Deb at the National Renewable Energy Laboratory in Golden/Colorado provided us with tungsten oxide layers on glass substrates that were used in the hydrogen sensor experiments as dielectric waveguide layer.

We used electron-beam lithography to fabricate the samples. The basic fabrication sequence is the following: a two-layer system of a photoresist is stuctured with an electron-beam and acts in the gold evaporation process as mask. The mask is then removed, leaving over a metallic structure on top of the waveguide material. An overview about the fabrication process is presented in Fig. 3.1 and will be discussed now in more detail. Further details about the fabrication process can be found in [32].

To remove dirt and dust from the surface of the waveguide layer, the samples are cleaned by washing them in several baths of acetone. In the next step, two layers of a photoresist are spin-coated on the substrate and prebaked. We used polymethylmethacrylate (PMMA) which is a positive photoresists. The layers differ in their electron sensitivities: the bottom layer has a molecular weight of 200 K at a concentration of 3.5%, the top layer 950 K at 1.5%. The samples are then structured with the electron-beam. Due to the higher electron sensitivity of the bottom layer, the exposed area is larger than in

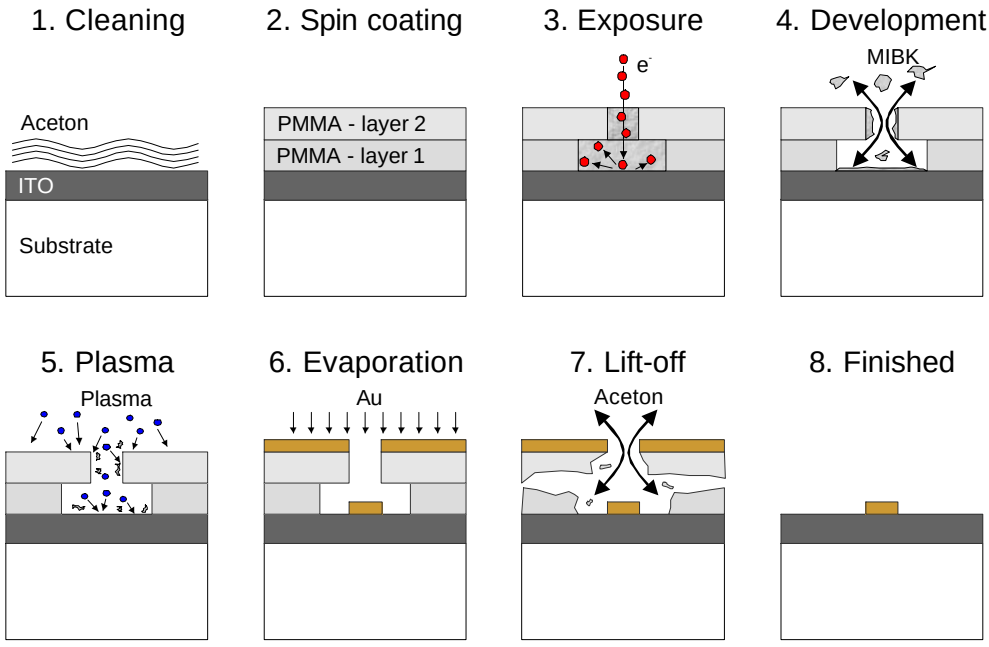

Figure 3.1: Sample fabrication with electron beam lithography: (1) Cleaning with acetone, (2) spin-coating of the photoresist, (3) exposure with electron-beam, (4) development, (5) cleaning with plasma cleaner, (6) gold evaporation, (7) lift-off, (8) final structure. Taken from [32].

the top layer. In the next step, the photoresist is developed with methylisobutylcetone (MIBC) and propanol in relation 1 : 3 and additionally cleaned with a plasma. Because PMMA is a positive resist, the developing process removes it in the exposed areas. Due to the two-layer system of PMMA, the system shows a so-called undercut: the removed area in the bottom layer is larger than in the top layer. This influences the gold evaporation process, where the top layer acts as a mask. As a result, we are able to write pronounced metal structures with defined shapes and positions. Especially the last point is very important for the disorder experiments, where we introduce a well-defined type and amount of positional disorder into the arrangement of the nanowires. In the last step, the photoresist mask is removed in a lift-off process, leaving the metallic structures on the waveguide material. This method is able to fabricate nanostructures on an area of 100 μm x 100 μm.

Figure 3.2 shows a scheme of a typical metallic photonic crystal slab structure. The picture demonstrates the different layers of the structure, namely the substrate, the waveguide layer and the arrangement of the gold nanowires. Additionally, a picture of a metallic photonic crystal slab is presented, that was taken with a scanning electron microscope (SEM). It shows gold nanowires on top of an ITO waveguide layer. Note that the width of the nanowires is larger than in the typical samples.

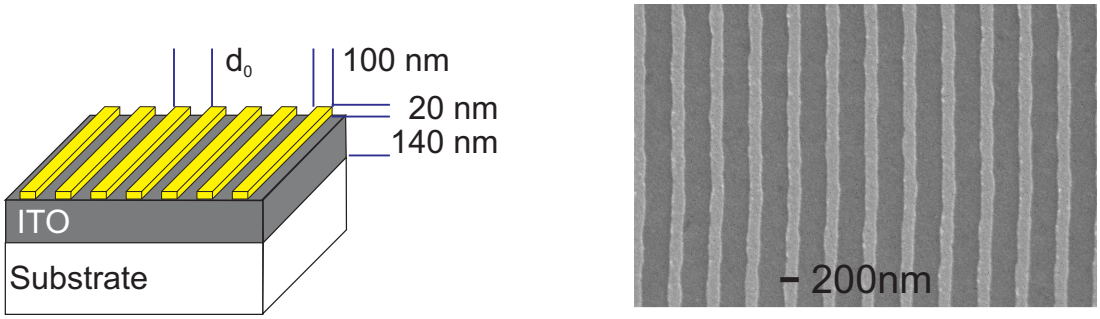

Figure 3.2: Left panel: Scheme of a metallic photonic crystal slab with period d_0. Right panel: SEM picture of gold nanowires on ITO, seen from the top.

3.2 Experimental setup

The measurements of the optical properties of the metallic photonic crystals are performed with a modified linear white-light absorption setup (see Fig. 3.3). We use a 50 W white-light halogen lamp as light source that produces a continuous spectrum from the blue to the near-infrared spectral range. Lens L1 (f = 50 mm) collimates the light to a slight divergent beam, which is then focused with lens L2 (f = 60 mm) to a small spot. An iris diaphragm in the focal point of L2 blocks part of the light and therefore acts as a point light source. Its light is recollimated by lens L3 (f = 60 mm) to a nearly parallel beam. After passing through a rotatable polarizer, that allows to vary the polarization of the light, a microscope objective (Zeiss A-Plan 20x/0.2) focuses the light on the sample. Lens L4 (f = 40 mm) forms again a parallel beam of the transmitted light and sends it to the detector. A lens with f = 40 mm images the incoming light beam on the entrance slit of the detector. We use two monochromators, one with a liquid-nitrogen cooled CCD-camera and one with a liquid-nitrogen cooled InGaAs-OMA as detectors for the visible and the near-infrared spectral range, respectively. All of the above mentioned lenses are achromatic, since light with a broad spectral distribution is used in the experiment. As it is necessary to work with small angles of incidence (see [9]), a pinhole with 600 μm diameter in front of the objective and one with 100 μm diameter after L4 are needed to reduce the angle below 0.2°.

The samples are mounted on a holder which is fixed in a rotation stage. This configuration is necessary for angle resolved experiments because it allows measurements with different angles of incidence. The rotation axis is normal to the optical table, the rotation resolution is 0.2°.

This setup allows to measure the absorption and the transmission of a sample. Additional modifications make possible the application of an external laser as light source by simply flipping a mirror between L3 and the polarizer. It is also possible to measure the reflection of samples by inserting a beam-splitter between L3 and the polarizer and sending the reflected light to the detectors. The whole data acquisition is controlled by a computer program written in LabView.

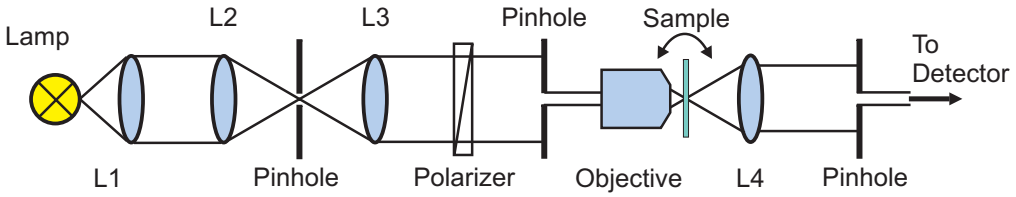

Figure 3.3: Linear absorption and transmission setup.

A measurement is performed by taking the background signal I_{Back} in a first step. The reference signal I_0 is measured by passing the light through substrate and waveguide material, the signal I is taken by transmitting the light through substrate, waveguide material and nanostructures. In the following chapters we will deal with the extinction of the samples, which is defined as the negative logarithm of the transmission T:

$$Extinction = -\ln(T) = -\ln\left(\frac{I - I_{Back}}{I_0 - I_{Back}}\right). \tag{3.1}$$

Therefore, the extinction considers the losses due to absorption, reflection and scattering by the nanostructures. A typical measurement with this setup takes 0.4 s exposure time to guarantee a good signal-to-noise ratio, averaging is not necessary in general.

Chapter 4

Disorder models

This chapter contains a description of the considered models of disorder and their characterization. In this context, disorder means a variation of the position of the nanostructures on top of the waveguide material (positional disorder), where next-neighbor positions are either correlated or uncorrelated. A variation of the size or the material of the nanostructure will not be considered here. Therefore, the considered disorder models belong to the class of positional disorder with topological order, according to the classification scheme presented in Chapter 2. As we are using electron-beam lithography to fabricate the samples, we are able to control the nanostructures' positions and shapes with a very high accuracy. This process provides us with a powerful tool to introduce artificial disorder with a well defined type and strength into the crystals [59]. In the following, the different disorder models will be described and presented in more detail. Various characterization methods and their results clarify the differences of the disorder models.

4.1 Frozen-phonon disorder (uncorrelated disorder)

In this disorder model, the positions of the nanostructures are shifted with respect to their positions in the perfectly ordered system. The positions x_i and x_{i-1} of neighboring nanostructures are therefore uncorrelated. The model is related to oscillations in solids, where atoms and ions perform movements around their equilibrium position due to thermal fluctuations [16]. These quantized oscillations are called phonons. As our model resembles a static arrangement of such phonons, we call this disorder model *frozen-phonon disorder*. With respect to the positions of neighboring nanostructures, we can also call this model *uncorrelated disorder*. The position of the i-th nanostructure is given by

$$x_i = x_0 + i \cdot d_0 + \Delta x_i, \tag{4.1}$$

where d_0 is the lattice period, x_0 the position of the zeroth nanostructure and Δx_i is the displacement of the i-th nanostructure with respect to the original grid position. The disordered arrangement with $N + 1$ lattice points can be described by the following

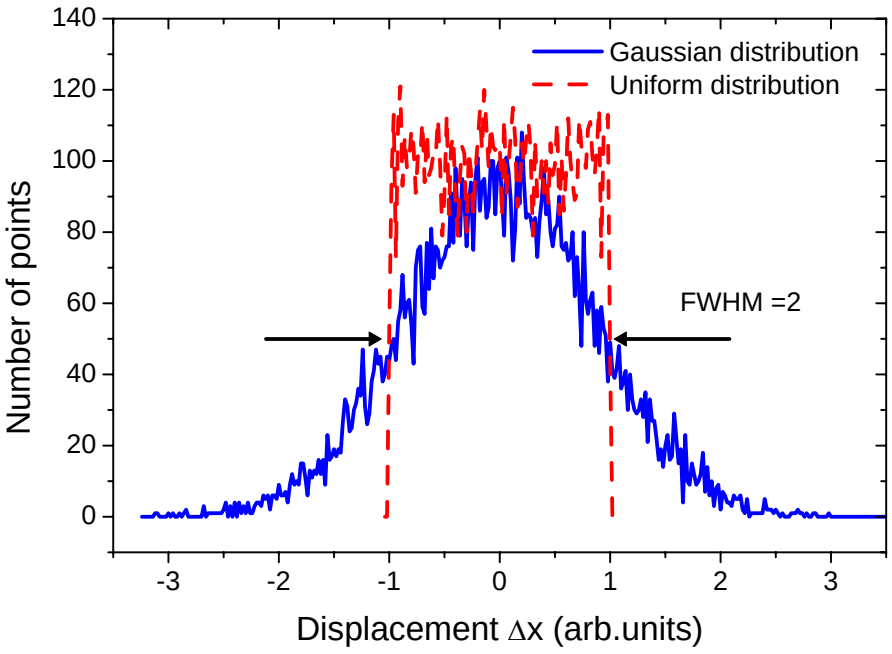

Figure 4.1: Comparison of Gaussian and uniform distribution, both with FWHM = 2. They cover the same area (here: 200 arb.units).

function:

$$comb_1(x) := \sum_{i=0}^{N} \delta(x - x_0 - i \cdot d_0 - \Delta x_i). \tag{4.2}$$

The displacements follow certain distribution functions $D(\Delta x)$. Here, we are considering two different distributions, both a uniform and a Gaussian distribution. The disorder is characterized by the amount U of disorder, which relates the full-width-at-half-maximum (FWHM) w of the distribution $D(\Delta x)$ to the period d_0 of the arrangement:

$$U[\%] = w/d_0 \cdot 100. \tag{4.3}$$

For example, a FWHM of $w = 100$ nm for the disorder distribution at a period of $d_0 = 400$ nm corresponds to an amount of disorder of $U = 25\%$. By considering the FWHM, we have a measure for comparing the distribution functions. It can be shown that a Gaussian and a uniform distribution with the same FWHM cover the same area. This makes sure that in our situation both distributions are comparable. Figure 4.1 shows such contributions with the same FWHM. Clearly, they cover the same area.

4.2 Long-range disorder (correlated disorder)

Another way of introducing disorder into the arrangement is to relate the position of a nanostructure no longer to the original grid, but rather to the position of the neighboring nanostructure. As a result, the positions x_i and x_{i-1} of these nanostructures are correlated. The implementation is done as follows. One nanostructure is set and the location of the next one is set at a distance from the first one, which corresponds to one lattice period with some variation. The position of the preceding one is then referred to the second one, and so on. Hence, the position of the i-th nanostructure is given by

$$x_i = x_0 + i \cdot d_0 + \sum_{n=1}^{i} \Delta x_n \tag{4.4}$$

with x_0 being the position of the zeroth nanostructure, d_0 being the lattice period, and Δx_n being the n-th variation. The total arrangement can be described by the following comb of δ-functions:

$$comb_2(x) := \sum_{i=0}^{N} \delta(x - x_0 - i \cdot d_0 - \sum_{n=1}^{i} \Delta x_n). \tag{4.5}$$

Since shifting the position of nanostructure i influences the positions of all nanostructures $j > i$, x_j includes all variations Δx_k with $k = 1 \ldots j-1$ of the preceding nanostructures. Hence, the uncertainty in determining x_j is larger than in the first model. We therefore call this disorder model *correlated disorder* or *long-range disorder*. Similar methods are used to model disorder in amorphous materials [60]. Again, the variations are either Gaussian or uniformly distributed, and the characterization of the disorder strength is given by the amount U of disorder.

To clarify the differences of the two disorder models we want to point out that they differ in the next-neighbor correlation. In the uncorrelated / frozen-phonon disorder model the positions of neighboring nanostructures are uncorrelated, whereas they are correlated in the correlated / long-range disorder model. Visually spoken, the first model only reduces the quality of the grating arrangement with N structures. Considering the zeroth and the last grating structure, their spatial distance is $\Delta x_0 + \Delta x_N + N \cdot d_0$. The second model additionally influences the long-range order of the grating, the distance between the nanostructures 0 and N is here $\sum_{i=1}^{N} \Delta x_i + N \cdot d_0$. In the following, we will use the terms *frozen-phonon disorder* and *long-range disorder*.

With these different disorder models and distributions, four different disorder types can be implemented:

- Uniform frozen-phonon disorder
- Gaussian frozen-phonon disorder
- Uniform long-range disorder

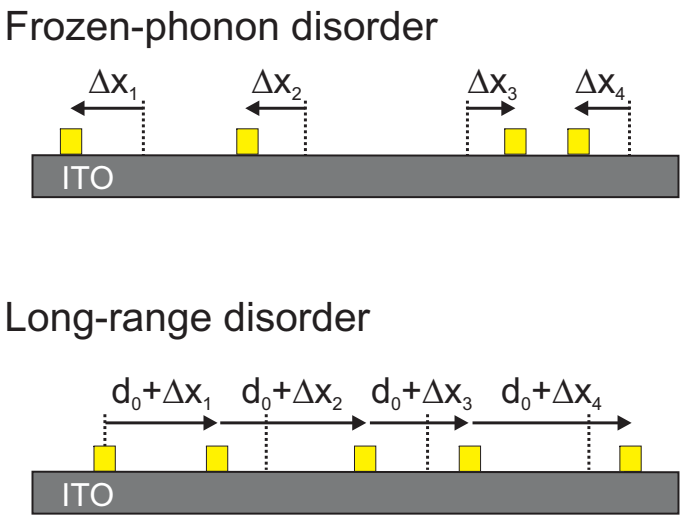

Figure 4.2: Scheme of frozen-phonon (uncorrelated) and long-range (correlated) disorder, respectively. Dotted lines indicate the perfect grating with period d_0.

- Gaussian long-range disorder

Figure 4.2 sketches the realization of the disorder structures. The dotted lines symbolize the perfect periodic grating, and the arrows indicate the movement of the electron-beam. In the case of frozen-phonon disorder, the starting point is always the perfect grating. In the long-range model the beam is moved from the preceding point to the new position.

4.3 Standard characterization of the disorder models

Simple statistical methods already allow to characterize the different disorder models. We assume a system with N nanoscatterers. According to the definition of the positional variations, the distribution of the Δx_i $(i = 1 \dots N)$ is centered around 0:

$$\overline{\Delta x} = \frac{1}{N} \sum_{i=1}^{N} \Delta x_i = 0. \tag{4.6}$$

Therefore, the mean value of all variations of the positions is $\overline{\Delta x} = 0$. To get some statistical data for each disorder model, we consider n different realizations of frozen-phonon (FP) and long-range (LR) disorder. The mean value for the position x_N of nanowire N for frozen-phonon disorder can be calculated by using Eqn. (4.1) to

$$\begin{aligned}\overline{\Delta x_N^{FP}} = \frac{1}{n}\sum_{j=1}^{n} x_{N,j}^{FP} &= \frac{1}{n}\sum_{j=1}^{n}(x_0 + N\cdot d_0 + \Delta x_{N,j}) \\ &= x_0 + N\cdot d_0 + \frac{1}{n}\sum_{j=1}^{n}\Delta x_{N,j} \\ &= x_0 + N\cdot d_0,\end{aligned}$$

and for long-range disorder, using Eqn. (4.4)

$$\begin{aligned}\overline{\Delta x_N^{LR}} = \frac{1}{n}\sum_{j=1}^{n} x_{N,j}^{LR} &= \frac{1}{n}\sum_{j=1}^{n}\Big(x_0 + N\cdot d_0 + \sum_{i=1}^{N}\Delta x_{i,j}\Big) \\ &= x_0 + N\cdot d_0 + \frac{1}{n}\sum_{j=1}^{N}\sum_{i=1}^{N}\Delta x_{i,j} \\ &= x_0 + N\cdot d_0.\end{aligned}$$

We find that the mean position $\overline{x_N}$ of nanowire N in both disorder models is identical

$$\overline{x_N^{FP}} = \overline{x_N^{LR}} = x_0 + N\cdot d_0. \tag{4.7}$$

But the standard deviations are different for frozen-phonon disorder

$$\begin{aligned}\sigma_N^{FP} = \sqrt{\frac{1}{n}\sum_{j=1}^{n}\big(x_j - \overline{x_N^{FP}}\big)^2} &= \sqrt{\frac{1}{n}\sum_{j=1}^{n}(x_0 + N\cdot d_0 + \Delta x_{N,j} - x_0 - N\cdot d_0)^2} \\ &= \sqrt{\frac{1}{n}\sum_{j=1}^{n}(\Delta x_{N,j})^2} \\ &= \sqrt{\overline{(\Delta x_N)^2}},\end{aligned}$$

and for long-range disorder

$$\begin{aligned}\sigma_N^{LR} = \sqrt{\frac{1}{n}\sum_{j=1}^{n}\big(x_j - \overline{x_N^{FP}}\big)^2} &= \sqrt{\frac{1}{n}\sum_{j=1}^{n}\Big(x_0 + N\cdot d_0 + \sum_{i=1}^{N}\Delta x_{i,j} - x_0 - N\cdot d_0\Big)^2} \\ &= \sqrt{\frac{1}{n}\sum_{j=1}^{n}\Big(\sum_{i=1}^{N}\Delta x_{i,j}\Big)^2}.\end{aligned}$$

Therefore $\sigma_N^{FP} \neq \sigma_N^{LR}$. To prove these results, numerical simulations are shown in Fig. 4.3. Here, 2000 different gratings with $N = 251$ nanowires and a period of 400 nm where simulated. The averaged grating length $\overline{x_N}$ together with the standard deviation

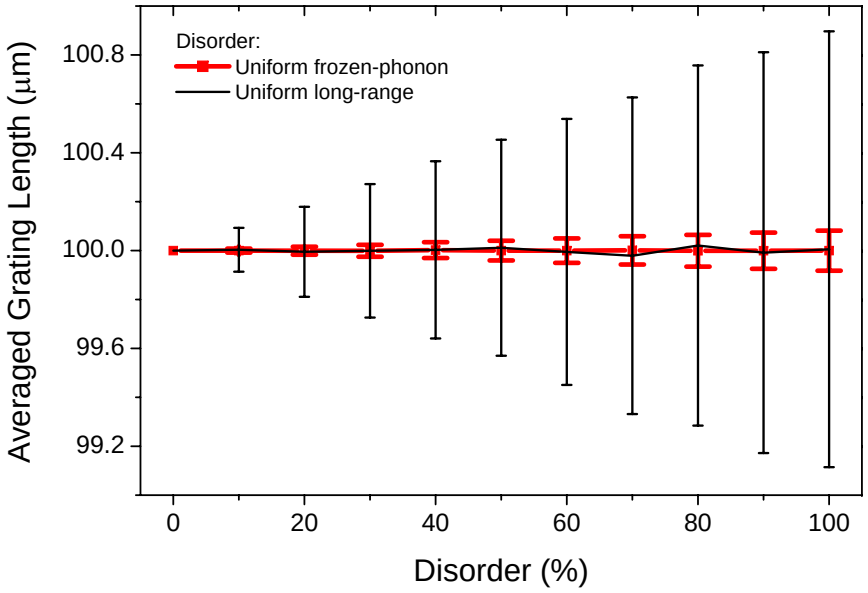

Figure 4.3: Averaged grating length $\overline{x_N}$ of samples for different amounts of uniform frozen-phonon and uniform long-range disorder. The simulations were performed for 251 nanowires and a period of 400 nm, the statistics was performed for 2000 different arrays.

σ_N as error bars are plotted for different disorder types and amounts. The results clearly show that frozen-phonon and long-range disorder cause the same averaged grating length, whereas the standard deviation is larger for long-range disorder. A system with frozen-phonon disorder only reduces the grating quality. The length of a grating with long-range disorder can deviate stronger from the averaged length. This indicates that the long-range order is reduced.

4.4 Two-point correlation function

Another possibility to characterize different models of disorder is to calculate the so-called *two-point correlation-function* (TPCF)

$$D(d) = \sum_{i=0}^{N} \sum_{j=0}^{N} \delta(d - (x_j - x_i)). \tag{4.8}$$

$D(d)$ gives the statistics of the distance d between any two nanostructures in the arrangement [61] and is the autocorrelation of the positions x of the nanostructures (see Appendix A, also for the other TPCF-calculations).

The calculation is done as follows: Starting at a certain nanowire, the distances to all other structures are calculated and plotted in a histogram. The same is then done for all other structures, resulting in a modified histogram, giving the aforementioned statistics.

For a perfect periodic arrangement, the distance between neighboring points is exactly one lattice period, the distance between any two points is a multiple integer of the lattice period. Hence, the TPCF consists of δ-peaks at multiple integers of the lattice period. With $N+1$ nanostructures and d_0 being the lattice constant,

$$D(x) = \sum_{i=0}^{N} \sum_{j=0}^{N} \delta(x - (j-i)d_0). \tag{4.9}$$

That means that the TPCF of a perfect grating is simply the sum of perfectly ordered combs of δ-peaks, centered at different points and resulting in a perfectly ordered comb. Since the size of a real array with nanostructures is finite, the δ-peaks do not have the same amplitudes: they rather decrease their height for larger distances. Therefore, the resulting comb appears in a triangular shape. Figure 4.4 shows the calculated TPCF for a perfect periodic assembly of nanostructures. The TPCF is plotted for different scales of the x-axis. In the top figure that shows all occurring distances, the peaks form a broad band due to their large density. Clearly, a reduction of the amplitudes towards the sides can be seen. Zooming into the TPCF reveals their character of single δ-peaks as mentioned above.

If we perform the TPCF-calculation for disordered structures, the characteristics of frozen-phonon and long-range disorder become clearer. In the frozen-phonon model, the positions of the nanostructures are varied around their original grid positions. Hence, the distance between two certain nanostructures i and j has increased by $\Delta x_i + \Delta x_j$, when compared with their distance $(j-i)d_0$ in the perfect grid. As a result, the TPCF-peak at $(j-i)d_0$ shows some broadening that is determined by their positional variation. This holds for all nanostructures, which means that the TPCF-peaks at multiple integers of the lattice period are simply broadened homogeneously by the sums of the variations of all nanostructures. At the same time, the amplitudes of the peaks reduce. The TPCF is given by

$$D(x) = \sum_{i=0}^{N} \sum_{j=0}^{N} \delta(x - (j-i)d_0 + \Delta x_i - \Delta x_j). \tag{4.10}$$

The result describes the summation of combs whose δ-peaks at $(j-i)d_0$ are shifted by $\Delta x_i - \Delta x_j$ with respect to each other. The TPCF of a structure with frozen-phonon disorder is therefore a comb of broadened δ-peaks. Since the FWHM of the distribution of Δx_i and Δx_j increases for increasing disorder, the broadening of the δ-peaks increases and the amplitudes decrease. Figure 4.5 shows the calculated TPCF for a structure with increasing uniform frozen-phonon disorder. Again we observe broad bands containing peaks, but their amplitudes decrease and their widths increase for increasing disorder as assumed above. Visually spoken, the band of δ-peaks is squeezed together when compared to the case of perfect order.

The TPCF of a crystal with long-range disorder looks quite different. Due to the

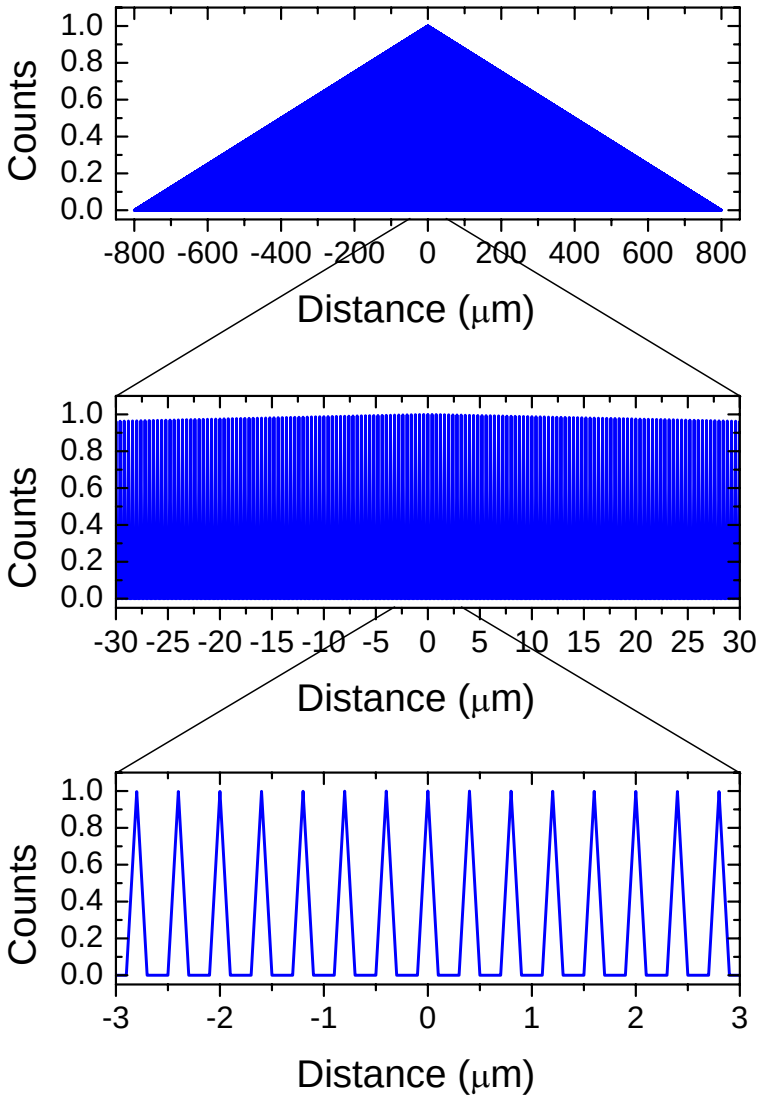

Figure 4.4: Two-point correlation function for a perfect periodic stucture with period d_0 = 400 nm. From top to bottom the scale of the x-axis is decreased to reveal details. Calculation for 2000 grating points; the period was set to $d_0 = 400$ nm.

correlation of the positions of neighboring structures, varying the position of a certain nanostructure influences the positions of all following structures. Hence, starting at a certain nanostructure, the distance to following nanostructures includes the variations of all nanostructures in between. Therefore, we expect that the distance between two nanostructures i and j deviates stronger from their distance in the prefect crystal as more nanostructures lie between them (i.e., the larger the difference $j - i$ is). Calculating the TPCF for such a system should show that the TPCF-peaks broaden more strongly if the distances are larger. At the same time, the amplitudes for larger distances are decreased

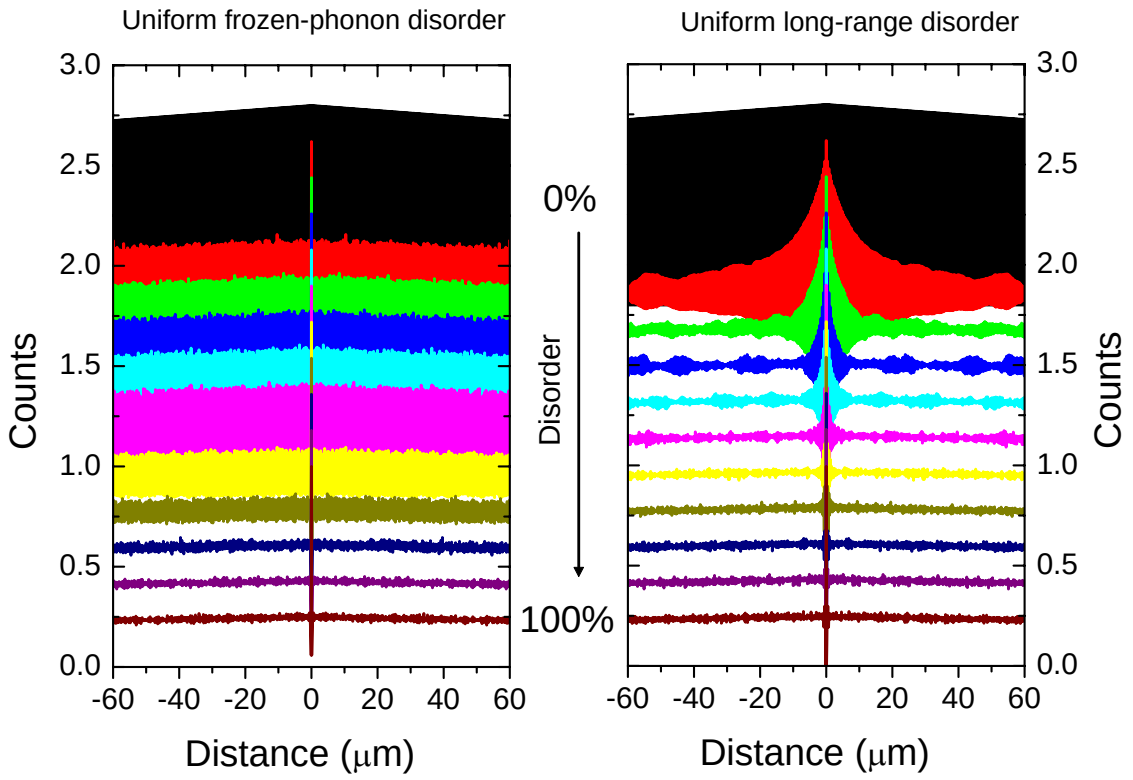

Figure 4.5: Two-point correlation function for structures with different amounts of uniform frozen-phonon and uniform long-range disorder. The calculation was done for structures with 2000 grating points, the period d_0 of the perfect crystal was 400 nm.

more strongly than those for smaller distances. The TPCF can be calculated as

$$D(x) = \sum_{i=0}^{N} \sum_{j=0}^{N} \delta\big(x - (j-i)d_0 + \sum_{n=1}^{i} \Delta x_n - \sum_{m=1}^{j} \Delta x_m\big). \tag{4.11}$$

Here, the positions of the δ-peaks at $x_0 + (j-i)d_0$ are shifted by the sums of the variations Δx_n and Δx_m, which are not constant but rather changing. Therefore, the δ-peaks are broadened and additionally shifted, which leads to a strongly modified TPCF of systems with long-range disorder.

The calculations shown in Fig. 4.5 confirm our ideas. The TPCF for a structure with long-range disorder shows a strong decline with large distances, and increasing the disorder causes this decline to become stronger. Due to the small period of $d_0 = 400$ nm, the single δ-shaped peaks can not be observed in the broad distance-range presented in this graph.

Comparing the TPCF for various disorder models clarifies the differences of these models. Peaks at small distances characterize short-range ordering, whereas peaks at long distances give information about the long-range arrangement of the grating structure. In the frozen-phonon model the peaks reduce their amplitudes homogeneously for small and large distances. Therefore, short-range and long-range characteristics are modified

equally. We can conclude that the frozen-phonon disorder only reduces the quality of the grating arrangement. The grating itself is not "destroyed", which means that the long-range order of the arrangement is preserved. This does not hold for the long-range disorder model, where the peaks at larger distances reduce their amplitudes stronger than those at smaller distances. Here, the long-range order is destroyed faster than the short-range order. The sharp peak at the origin of the TPCF arises from the distance of each point to itself. This peak therefore appears in both disorder models for all disorder strengths.

A further result of the TPCF analysis are the characteristics of different distributions in the same disorder model (not plotted here). Both uniform and Gaussian distribution have the same qualitative properties in a certain disorder model. But the TPCF for a Gaussian distribution has lower amplitudes at a certain amount of disorder than the uniform distribution. This can be understood intuitively as the Gaussian distribution has a larger range for a certain FWHM than the uniform distribution (see Fig. 4.1). This results in a larger broadening and smaller amplitudes of the TPCF-peaks for a given disorder amount when compared with the uniform distribution.

4.5 Fourier analysis

A very elegant method to characterize and to understand disordered systems is a Fourier analysis of the spatial arrangement of the nanostructures [32]. Only the positions of the nanostructures are considered. Their form and shape have no influence on the results as they are not taken into account here. We assume the system to consist of single δ-shaped peaks at the center of the position of the nanostructures. Calculating the Fourier transformation of this spatial distribution reveals further details about different disorder models.

Figure 4.6 shows the results for different disorder models. The calculations were performed for grating arrangements with 1000 wires at a period of 400 nm, and the different disorder amounts were varied in steps of 10%. For simplicity, we consider only the k-range around the first Fourier harmonic at $g_0 = 2\pi/d_0$, where d_0 is the period and g_0 a reciprocal lattice vector. It should be emphasized that the main effects are independent of the distribution of the variations Δx (uniform or Gaussian) and only depend on the disorder type (frozen-phonon or long-range disorder). For no disorder, a sharp δ-shaped peak at $k = g_0$ is formed. Increasing frozen-phonon disorder reduces the amplitude A_0 of this peak, and its width is nearly unaffected for disorder amounts of less than 50%. In the case of long-range disorder, the amplitude of the peak at $k = g_0$ is also reduced. Additionally, an inhomogeneous broadening of the peak is observed already for small disorder amounts. This broadening is caused by further peaks at $k_j \neq g_0$ with amplitudes A_j as large as A_0. These peaks arise due to a reduced long-range ordering, where periods $d_j \neq d_0$ can appear in the arrangement. The peaks can be so pronounced that a whole group of Fourier components in a widespread k-range around g_0 with $k_j \neq g_0$ are typical for this disorder model.

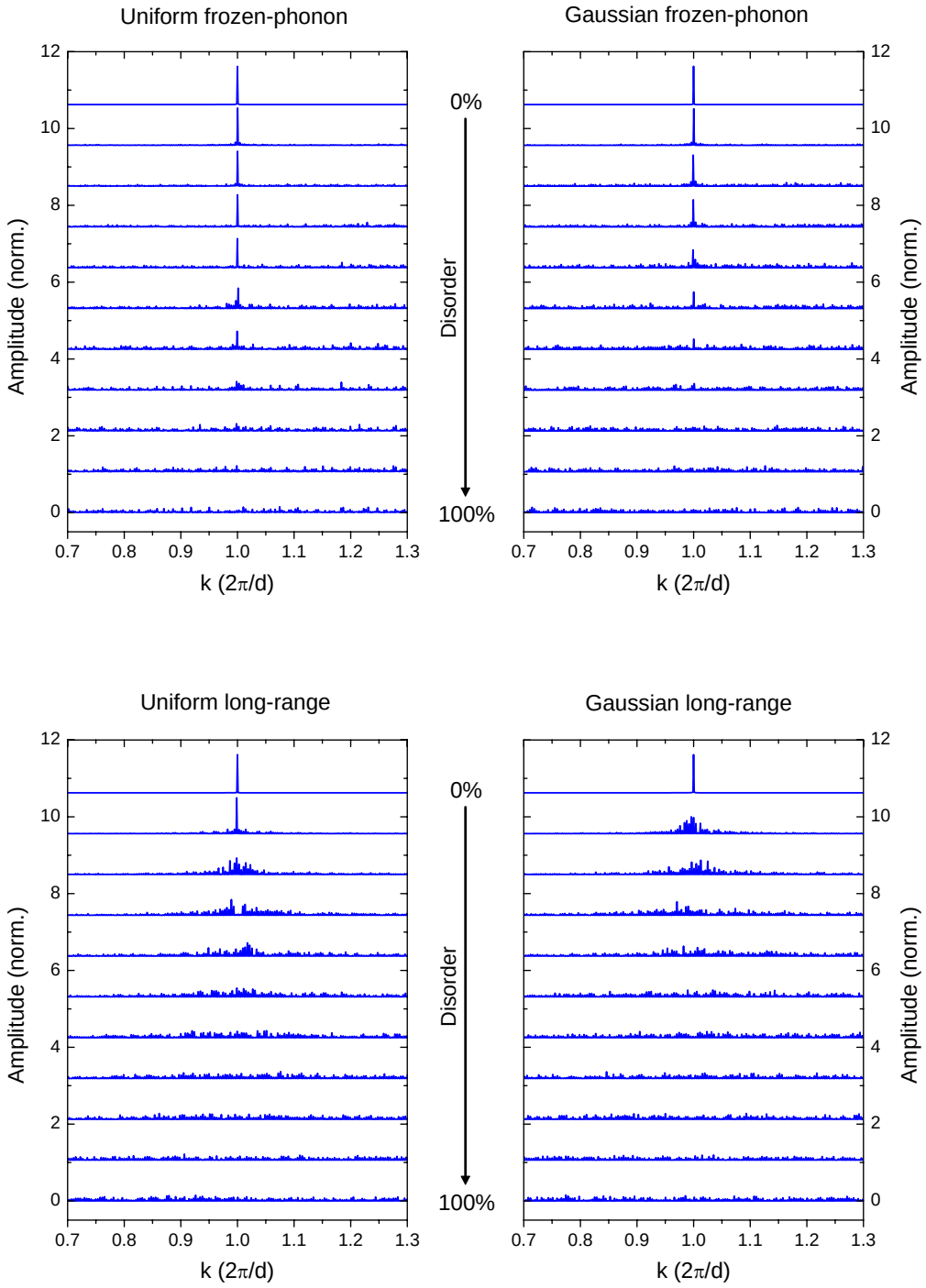

Figure 4.6: Fourier-analysis of gratings with different disorder types and amounts. Each grating consisted of 1000 wires with a period of 400 nm, and the disorder was increased in steps of 10%. Upper panel: Analysis of uniform frozen-phonon and Gaussian frozen-phonon disorder. Lower panel: Analysis of uniform long-range and Gaussian long-range disorder.

The effect of different distributions is to change the disorder amount that reduces A_0 to a certain amplitude, while qualitative effects are independent of the distribution. For

frozen-phonon disorder, the peak at g_0 vanishes for an amount of 70-80% in the case of a uniform distribution. For a Gaussian distribution, this peak disappears already for an amount of 60-70%. Taking long-range disorder, the vanishing takes place for smaller amounts of disorder, i.e., for an amount of 40% in a uniform and of 30% in a Gaussian distribution. Therefore, a Gaussian distribution requires a smaller disorder amount than a uniform distribution to produce a certain effect. This is reasonable, because according to the definitions of uniform and Gaussian distributions larger deviations from the mean value can appear in the latter distribution if both have the same FWHM. However, the distributions are not responsible for the broadening of the peak.

To better understand these results, we make use of the similarity between a Fourier analysis of a spatial arrangement of nanostructures and the results from diffraction experiments on these nanoscatterers [16]. We can use these results to explain the Fourier analysis of the disorder types. The diffraction pattern of perfect crystals with period d_0 shows sharp peaks at multiple integers of the reciprocal lattice vector $g_0 = 2\pi/d_0$. This corresponds to the Fourier peak at $k = g_0$. In a thermal hot solid, the positions of the atoms are varied around their original grid positions. As a result, the diffraction peaks decrease their amplitudes. This behaviour can be modelled with the Debye-Waller factor in solid state physics [16] and was already transferred to metallic photonic crystals [62]. For the variation Δx^2 of the nanowires' positions, the scattered intensity I_{Sca} for the reciprocal lattice vector k is given by

$$I_{Sca} = I_0 \exp\Big(-\frac{1}{3}\langle \Delta x^2 \rangle k^2 \Big). \tag{4.12}$$

I_0 is the scattered intensity without disorder. The phenomena observed in the Fourier analysis of long-range disordered samples resemble diffraction experiments with liquids and amorphous materials. These are systems in which some ordering takes place on a short-range scale; they are disordered on a long-range scale [41]. Their diffraction patterns show broad maxima that are not clearly separated from each other [63, 64]. Similar observations can be made in the Fourier analysis of systems with long-range disorder (see Fig. 4.6). The scattered intensity is given by [16]

$$I_{Sca} = N f^2 \Big[1 + \sum_{m \neq n} \Big(\sin(k x_{mn}) \Big) / k x_{mn} \Big]. \tag{4.13}$$

I_{Sca} contains the number N of atoms and the atomic form factor f.

These results indicate that our models describe in fact systems with different disorder types. Frozen-phonon disorder is similar to thermal phonons in a solid, long-range disorder resembles liquid systems. The models differ especially in the correlation of their next-neighbor positions. Long-range disorder shows a pronounced next-neighbor correlation, whereas in the frozen-phonon disorder these next-neighbor positions are uncorrelated.

Chapter 5

Measurements on disordered systems

In this chapter, experimental measurements of disordered samples are presented. After a description of the samples, measurements for normal light incidence and results from angle-resolved measurements are shown for all types and strengths of disorder (see Chapter 4). The measurements were performed with a transmission setup as described in Chapter 3. These results are compared with data obtained from a straightforward theory.

5.1 Sample description

We consider samples that consist of gold wires on top of an ITO layer. The wires have a height of 20 nm, a width of 100 nm, and the thickness of the ITO-layer is 140 nm. The parameters were chosen such that the excited resonances lie in the visible spectral range. The extinction spectrum in TM polarization then reveals the coupled system of particle plasmon and quasiguided mode (see Fig. 2.10). These measurements allow the determination of the influence of disorder on the optical properties of the polariton system. The specific sample parameters are given in Table 5.1.

Sample	**Disorder Type**	**Period**
#95	Uniform frozen-phonon	400 nm
D11	Gaussian frozen-phonon	430 nm
D12	Uniform long-range	450 nm
#117	Gaussian long-range	475 nm
#126	Gaussian long-range	450 nm

Table 5.1: Parameters of the disordered samples.

A comparison of the optical properties of disordered samples with respect to several aspects is possible. The samples #95 and D11 have the same disorder type (frozen-phonon), but different distributions $D(\Delta x)$ of the position variation. Samples #95 and D12 differ in the disorder type but not in the distribution $D(\Delta x)$, that is uniform. D12 and #117 exhibit the same disorder type (long-range) but different distributions, #117

and #126 have identical disorder type (Gaussian long-range) but different periods.

It should be emphasized that the electron-beam machine that was used to fabricate the nanowires was not always working with perfect reproducibility. Fabricating two samples with identical grating arrangements and optical properties was rather difficult. Therefore, samples with identical fabrication parameters do not necessarily exhibit identical structures and optical properties in the end. This explains why the polariton branches and quasiguided modes of the samples do not lie at the same energies: The samples differ with respect to detuning from the waveguide-plasmon crossing point. This has to be taken into account when studying the following extinction spectra.

5.2 Extinction spectra at normal light incidence

Measured extinction spectra of sample #95 (uniform frozen-phonon disorder) are plotted in Fig. 5.1. The individual spectra are shifted upwards for clarity in each panel, also in the following graphs. In TM polarization, two resonances appear in the case of no disorder. They can be identified as the lower and upper polariton branches [35]. Increasing uniform frozen-phonon disorder causes the peak at high energy to decrease its amplitude further, whereas the peak at lower energies is nearly unaffected. For disorder amounts of more than 80% only one broad peak is observable in the extinction. A slight broadening of the lower polariton branch resonance is attributed to near-field coupling effects of approaching nanowires [23] in the disordered system. The spectral separation between lower and upper polariton branch (polariton splitting) decreases slightly for increasing disorder. Note that the detuning between plasmon and waveguide mode is quite large for this sample. Starting at 420 meV for no disorder, this splitting reduces to about 340 meV for 70% disorder. For larger amounts the splitting can not be determined due to the vanishing of the upper polariton peak. A detailed analysis and interpretation of this reduced polariton splitting is given later in this chapter. In TE polarization, the typical Fano-like resonance of the quasiguided mode can be observed for no disorder [9, 35]. Increasing disorder reduces the amplitude of this peak, while its width is kept nearly unaffected. For a disorder amount of 90% the peak has completely vanished, indicating that the quasiguided mode is no longer excited. A slight shift of the resonance peak to lower energies is caused by the disorder-influence on the TE-bandstructure [59], as discussed later in this chapter.

These results can be compared with the extinction of sample D11 because both samples have the same disorder type but different distributions $D(\Delta x)$. For this reason, the influence of the *distribution variation* on the optical properties can be directly examined. As will be shown later, the different periods of the samples (400 nm vs. 430 nm) only slightly affect the principal observations.

The extinction of sample D11 with Gaussian frozen-phonon disorder is plotted in Fig. 5.2. The spectra are similar to the ones from sample #95, except for the different energies of the resonances. Especially the polariton branches in TM polarization show a stronger coupling because their energy separation is smaller than for sample #95.

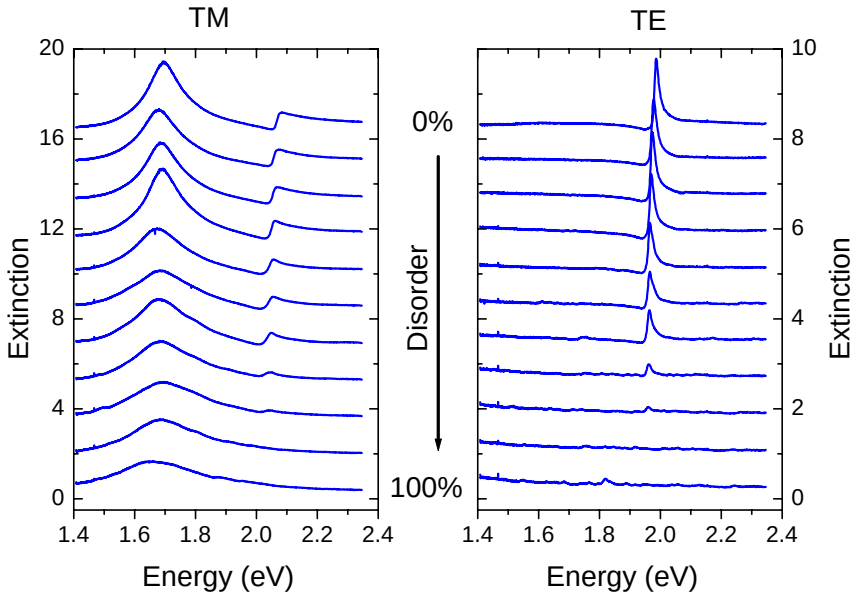

Figure 5.1: Measured extinction of a sample with uniform frozen-phonon disorder (sample #95) at normal light incidence, both in TM and TE polarization.

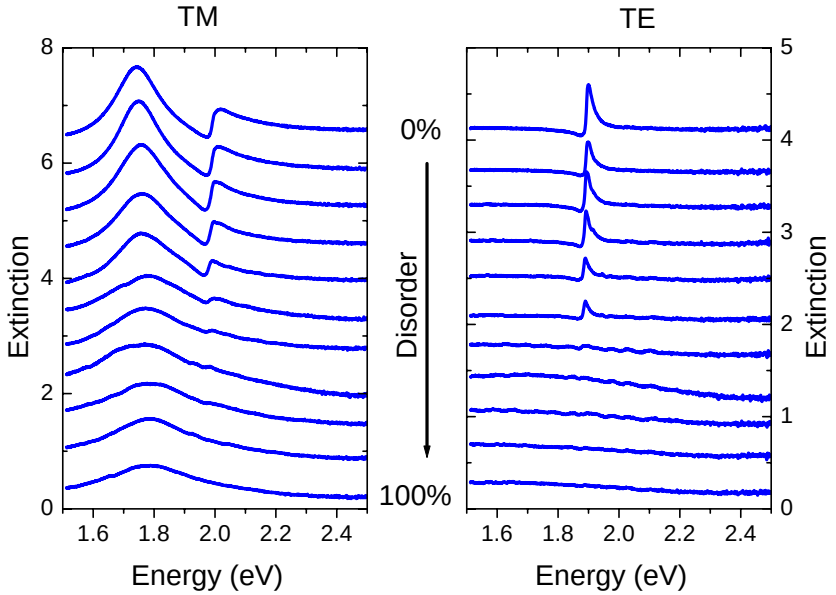

Figure 5.2: Measured extinction of a sample with Gaussian frozen-phonon disorder (sample D11) at normal light incidence, both in TM and TE polarization.

However, increasing Gaussian frozen-phonon disorder also reduces the amplitudes of the upper polariton branch in TM polarization and of the quasiguided mode in TE polarization. These resonances vanish for a disorder amount of 60-70% which is less than for sample #95 with uniform frozen-phonon disorder. Additionally, upper and lower TM resonance also decrease their energy separation due to a shift of the resonances to lower and higher energies, respectively.

Now we want to discuss the influence of the *disorder type* on the optical properties of the structures. The extinction of sample D12 with uniform long-range disorder is pre-

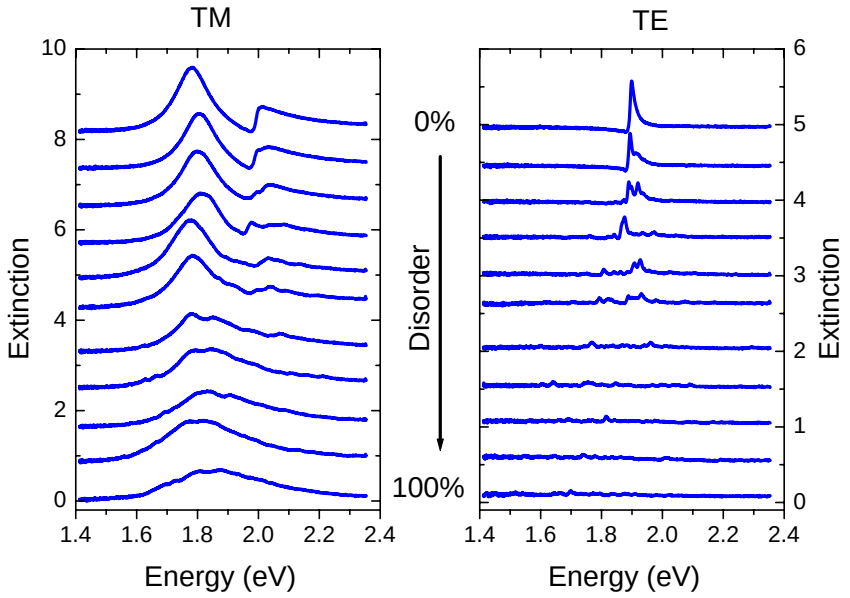

Figure 5.3: Measured extinction of a sample with uniform long-range disorder (sample D12) at normal light incidence, both in TM and TE polarization.

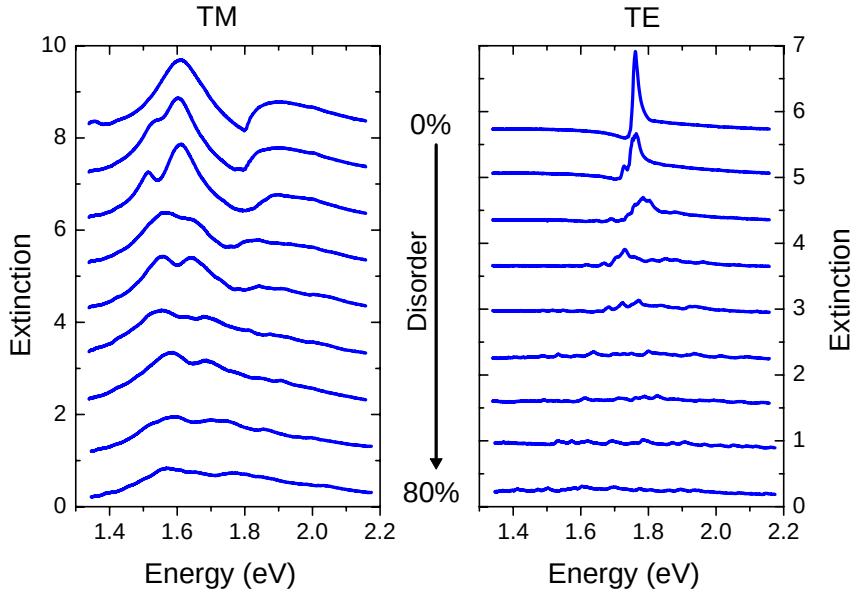

Figure 5.4: Measured extinction of a sample with Gaussian long-range disorder (sample #117, period $d_0 = 475$ nm) at normal light incidence, both in TM and TE polarization.

sented in Fig. 5.3. The spectrum for no disorder in TM polarization shows again the polariton signature. Contrary to the results of samples #95 and D11, both polariton branches are influenced by rising uniform long-range disorder: they are broadened inhomogeneously. Both resonances feature a substructure of several maxima and minima that becomes stronger when the disorder is further increased. The substructure is more pronounced at the upper polariton branch and only hardly visible at the lower polariton branch. This inhomogeneous broadening does not allow the determination of the polariton splitting as a function of disorder anymore. The broadened resonances make a clear

determination of the peaks for large disorder amounts difficult. At very large disorder amounts, again only one broad peak is observable. In TE polarization, the resonance peak of the quasiguided mode is also affected by this disorder type. The reduction of the peak's amplitude is stronger when compared with the spectra of sample #95. It results in a complete vanishing of the peak for an amount of 50-60%, in comparison with an amount of 90% in the frozen-phonon model. Again, the missing of the resonance indicates the missing of the quasiguided mode. Additionally, a strong inhomogeneous broadening of the resonance can be observed. For a disorder amount of only 20% it is not possible to excite a single resonance at the former spectral positions. Rather two pronounced maxima appear in the extinction, and their number is rising for even higher disorder amounts. This modification is not just a simple broadening of the original peak. The emphasis of the resonance rather shifts to smaller and higher energies for different disorder amounts. At first sight, we can speculate about the origin of the additional peaks. One possibility could be localized states [3, 41] that may appear in this disorder model. Later it will be shown in more detail that the excitation of multiple resonances at slightly different energies is the responsible mechanism of the inhomogeneous broadening.

The observed inhomogeneous broadening indeed originates specifically from long-range disorder. This becomes obvious when looking at the extinction of sample #117 with Gaussian long-range disorder in Fig. 5.4. Increasing the disorder shows a similar broadening in TE and TM polarization. The substructure on lower and upper polariton branches in TM polarization is more pronounced than that in Fig. 5.3. This also holds for the resonance in TE polarization. Moreover, the strong reduction of the amplitudes is even more drastic than for sample D12. The quasiguided mode in TE polarization vanishes for a disorder amount of 40-50%. The main spectral features and observations are identical with the ones in Fig. 5.3, indicating that long-range disorder affects the optical properties differently than frozen-phonon disorder. The observations are not governed by the distribution $D(\Delta x)$.

The main effect of the period d_0 is to determine the energies of the polariton branches and hence the detuning of plasmon and quasiguided mode (see Fig. 2.10). Therefore, the effects of disorder in samples with the same disorder type but different periods are comparable. Sample #126 only differs by a smaller period from sample #117, both have a Gaussian long-range disorder. The extinction spectra of sample #126 are presented in Fig. 5.5. Unfortunately, the disorder amounts in these samples are not identical. The spectra of sample #126 should be compared with the spectra for 0%, 10%, and 20% disorder in Fig. 5.4. The spectra are similar with respect to the reduced amplitudes and the broadening of the resonances for increasing disorder. As will be discussed later, the reductions of the energy separation between the polariton branches and of the gaps in the bandstructure crucially depend on the detuning. Consequently, the period has a dramatic influence in disordered systems.

To summarize, we have shown that disorder causes a reduction of the extinction of the

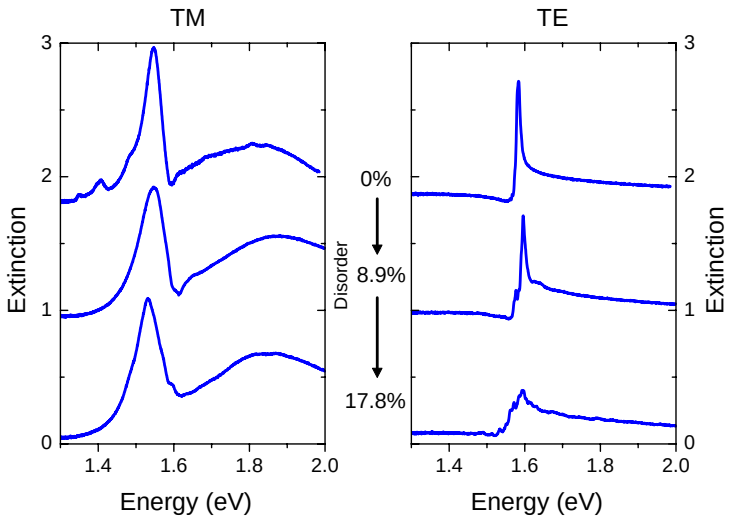

Figure 5.5: Measured extinction of a sample with Gaussian long-range disorder (sample #126, $d_0 = 450$ nm) at normal light incidence, both in TM and TE polarization.

quasiguided mode in TE polarization and of the quasiguided mode polariton branch in TM polarization. This reduction is stronger for long-range disorder than for frozen-phonon disorder. Long-range disorder additionally broadens the resonances inhomogeneously. These spectral effects are caused by the disorder type, neither by the distribution $D(\Delta x)$ of the position variation nor by the period d_0 of the grating arrangement. The energy separation between the polariton branches is reduced for increasing frozen-phonon disorder. This effect strongly depends on the period, see later on. A clear determination of this polariton splitting is not possible in systems with long-range disorder.

5.3 Scattering matrix results

In this section we compare the above presented experimental results with simulations from a scattering matrix method [65, 66]. This method showed a good description of experimental transmission spectra, especially in polaritonic systems [30, 35].

Figure 5.6 presents a comparison of the extinction spectra of samples #95 and #117 with scattering matrix simulations in TM polarization. It should be underlined that the simulations were performed for slightly different periods d_0. Therefore, the polariton peaks appear at different energies in experiment and theory. Additionally, the distribution $D(\Delta x)$ in the long-range model is different in experiment and theory. However, as shown above, the general spectral features from disorder effects are independent of d_0 and $D(\Delta x)$. The agreement for uniform frozen-phonon disorder is quite good. The experimentally observed reduction of the extinction of the upper polariton branch is nicely reproduced in the simulations. As in the experiment, the peak vanishes for a disorder amount of more than 80%. Also the shape of the peaks is mirrored well, no substructure appears. Some smaller peaks at around 1.65 eV and 2.07 eV are probably caused by using supercells in the

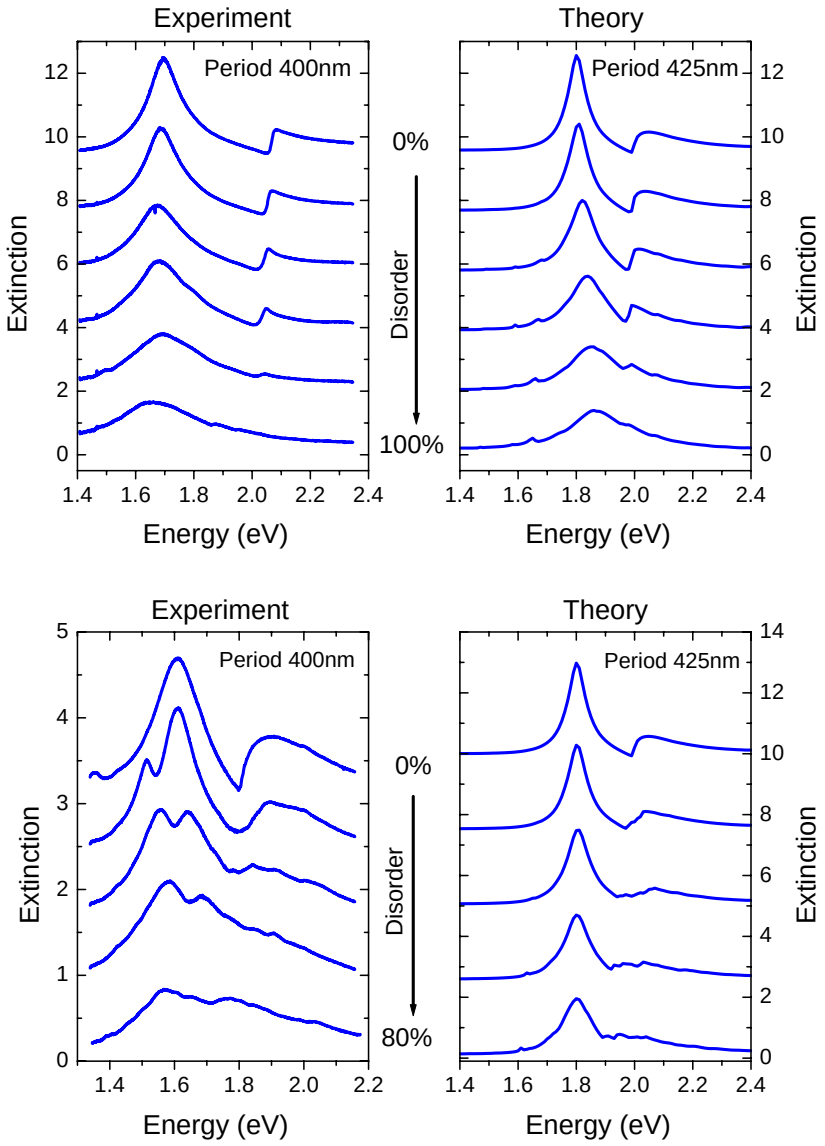

Figure 5.6: Comparison of experiment and scattering matrix theory in TM polarization. Upper panel: Frozen-phonon disorder, lower panel: Long-range disorder. Note, that period and distribution do not coincident, see text.

scattering matrix theory [62]. Interestingly, a strong shifting of the resonances' energies is observable in the simulations. The energy separation of the peaks reduces strongly for increasing disorder because the lower polariton branch shifts to higher and the upper polariton branch to lower energies. Similar observations are made in the experiment but the reduction of this energy separation is much smaller. This can be explained with near-field coupling effects of the metallic nanowires, see Chapter 2.

The experimental extinction spectra of sample #117 and the scattering matrix simulations do not match that well. Whereas the upper polariton branch vanishes for a disorder amount of 40-50% in the experiment, it is still excited for an amount of 60% in the simulation. Maybe the different distributions $D(\Delta x)$ are responsible for this slight discrepancy. Additionally, the strong inhomogeneous broadening of the resonances is not

reproduced in the simulation. Hence, scattering matrix calculations of this kind seem to be not adequate to determine the optical properties of metallic photonic crystal slabs with long-range disorder. The observed discrepancies are probably due to weaknesses of the numerical realization. Usually the scattering matrix method uses a Fourier decomposition of the periodic grating arrangement. As this method requires a high number of Fourier components in systems with positional disorder, a way to drop the computing time is to divide the grating arrangement into supercells. Unfortunately, this method does not work properly for long-rang disorder due to its periodicity. Therefore, we observe these large discrepancies between experimental and theoretical extinction spectra.

The disadvantage of the scattering matrix method is that it only allows to calculate spectra which does not necessarily yield a deeper understanding of the underlying physics. Hence, an alternative way of theoretically deriving and explaining the reducing amplitudes, the reducing energy separation of the polariton branches and the inhomogeneous broadening has to be found. All effects can and will be explained with simple models that are presented in the following sections.

5.4 Modelling the polariton splitting in disordered systems

To understand the reduction of the energy separation between lower and upper polariton branch for rising frozen-phonon disorder (see Fig. 5.1), we make use of the fact that this separation is caused by the polariton splitting E_{PS}, which was introduced in the dispersion $E(k)$ in Chapter 2. Contrary to the system without coupling of plasmon and quasiguided mode, $E(k)$ describes two dispersion curves with an anti-crossing behavior. The minimum energy separation at momentum k_{PS} is the polariton splitting E_{PS}, the separation in the k-range around k_{PS} is hence determined by E_{PS}. E_{PS} itself is caused by the interaction of particle plasmon and quasiguided mode [9]. It can be calculated by using the waveguide photon - wire plasmon coupling energy V_2, the half-widths of waveguide mode γ and plasmon resonance Γ and the radiative damping γ_1 of the optical mode [9] (see also Chapter 2):

$$E_{PS} \propto \sqrt{8V_2^2 - (\Gamma - \gamma - \gamma_1)^2}. \tag{5.1}$$

Since Γ, γ, and γ_1 are sample dependent constants that are determined by physical effects, the only way to vary E_{PS} is to change V_2. This coupling energy is described by the spatial overlap of the electrical fields of particle plasmon $\mathbf{E}_{Pl}(\mathbf{r})$ and waveguide mode $\mathbf{E}_{WG}(\mathbf{r})$:

$$V_2 \propto \int \mathbf{E}_{WG} \cdot \mathbf{E}_{Pl}\, d\mathbf{r}. \tag{5.2}$$

To quantitatively determine the decrease of V_2, we calculate V_2 in a very simple model.

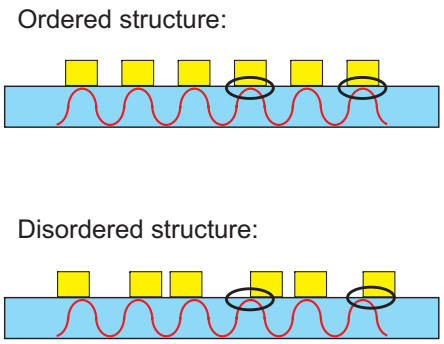

Figure 5.7: Visualization of the spatial overlap of E_{WG} (in the waveguide layer) and E_{Pl} (inside the metal structures) in ordered and disordered structures.

We restrict ourselves to a 1-dim case with $\mathbf{E}_{Pl}(\mathbf{r}) = E_{Pl}(x)$ and $\mathbf{E}_{WG}(\mathbf{r}) = E_{WG}(x)$. The x-direction is given along the direction of the modulation of the grating. Usually, the plasmon field E_{Pl} can be described by a multipole field that is localized mainly at the positions of the nanowires [17, 24]. The quasiguided mode E_{WG} as a standing wave inside the waveguide layer interacts with E_{Pl}. Introducing disorder shifts the positions of the nanowires and hence of the plasmonic fields along the x-axis (see Fig. 5.7). Therefore, the interaction area of E_{WG} and E_{Pl} is reduced, causing a reduction also of V_2. For simplicity, we describe E_{WG} and E_{Pl} with simple models in the following.

We assume E_{WG} to be a cos-type wave that can be described by a harmonic function

$$E_{WG}(x, \varphi) = \cos\Big((2\pi x - \varphi)/d_0\Big). \tag{5.3}$$

Here, x is the position in the direction of the waveguide layer, φ is the phase and d_0 the period of the grating. The argument of the cos-function is chosen such that its extrema are located at the positions of the nanowires in a perfect grating with period d_0. Therefore, Eqn. (5.3) describes the electrical field of the quasiguided mode and not its intensity.

The oscillation of the electrons and the corresponding electrical field of the particle plasmons E_{Pl} is set to be constant inside the nanostructures and zero outside:

$$E_{Pl}(x) = \begin{cases} 1 & : \quad x \in nanowire \\ 0 & : \quad x \notin nanowire \end{cases} \tag{5.4}$$

For simplicity, we completely neglect specific material parameters. The positions of the nanostructures are defined by disorder type and amount. Depending on the phase φ of E_{WG}, the spatial position of E_{WG} in the waveguide layer can be shifted. Therefore, we find V_2 to be a function of φ. We compute the coupling energy V_2^{Dis} in the disordered case as the maximum overlap of E_{WG} with E_{Pl}. In a first step, we calculate $V_2^{Dis} = \int E_{WG} \cdot E_{Pl}\, dx$ for $\varphi = 0$. Then, the calculation is repeated for different phases φ that shift E_{WG} inside the waveguide layer along the x-direction. After shifting of E_{WG} by a complete period 2π,

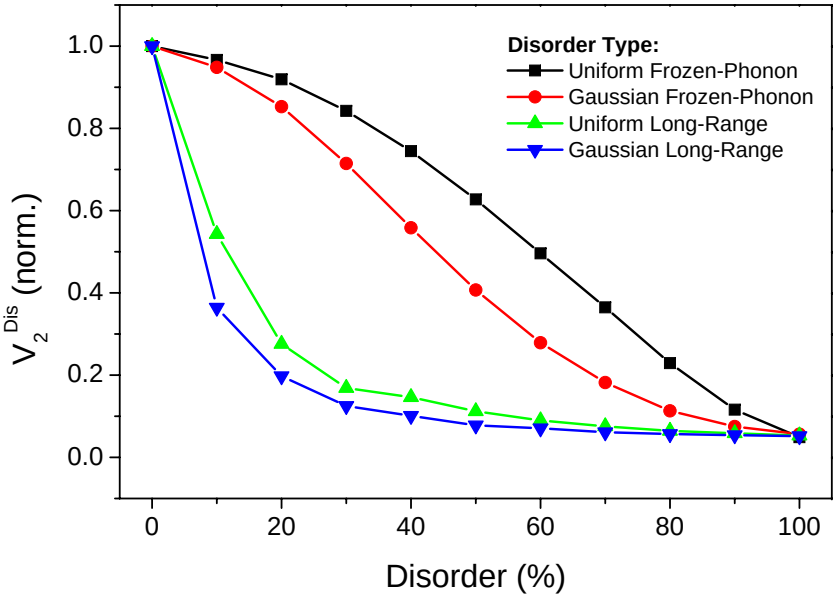

Figure 5.8: Normalized spatial overlap V_2^{Dis} as a function of disorder for different disorder types.

the maximum calculated result is taken as V_2^{Dis}. This procedure ensures that in a perfectly ordered sample the maximum spatial overlap of E_{WG} and E_{Pl} is given when the nodes of E_{WG} are positioned directly beneath the nanostructures. In systems with positional disorder where the nanostructures are no longer located at the original grid positions, this method shifts E_{WG} to get the maximum V_2^{Dis}. In the simulations presented here, d_0 was kept constant. In our simple picture, we receive

$$V_2^{Dis} = max\Big(\int\int E_{WG}(x,\varphi)\cdot E_{Pl}(x)\,dx\,d\varphi\Big)\cdot\frac{1}{V_2}. \tag{5.5}$$

By definition, $E_{WG}(x,\varphi)$ depends on the period of the system. Therefore, also V_2^{Dis} is a function of d_0. To get comparable results that can be used in the following calculations, we normalize V_2^{Dis} to V_2 from the perfect grating, see Eqn. (5.5). By doing this, we get $V_2^{Dis} = 1$ for the perfect system and $V_2^{Dis} < 1$ for disordered arrangements.

Figure 5.8 shows the normalized V_2^{Dis} as a function of disorder for different disorder types. The results were obtained by averaging over 200 different grating realizations for each disorder type and amount. Each grating consisted of 300 wires with a period of d_0 = 400 nm, and the wires' width was set to 100 nm. V_2^{Dis} is affected and reduced more by long-range disorder than by frozen-phonon disorder if the disorder amount is larger than 0. This can be understood easily because frozen-phonon disorder and long-range disorder have the same average grating length. However, the latter disorder type shows stronger deviations from this average length, see Fig. 4.3. Now we want to compare a Gaussian and a uniform distribution $D(\Delta x)$ of the variations Δx_i. For a given FWHM, the range of $D(\Delta x)$ is larger for a Gaussian than for a uniform distribution. Hence, the

spatial overlap of E_{WG} and E_{Pl} and therefore V_2^{Dis} is reduced for a Gaussian distribution $D(\Delta x)$, as shown in Fig. 5.8. For details see also appendix B.

The so-obtained results are used in the following calculations to describe the influence of disorder on the polariton coupling V_2. Taking the normalized V_2^{Dis} as a prefactor of V_2 of the perfect system allows to perform the calculations with a modified V_2^{mod}. This value is maximal for the perfect arrangement and reduced in disordered systems:

$$V_2^{mod} = V_2 \cdot V_2^{Dis}. \tag{5.6}$$

Of course, this is a simplified picture with lots of approximations. First, E_{WG} can not be exactly described by a harmonic function. In real systems, E_{WG} consists of a field with nodes under the center of the nanostructures [35, 67]. But to our knowledge, no work has yet been published about E_{WG} in disordered systems. Second, the electric field E_{Pl} of the particle plasmon is not localized within the nanostructures. The electron oscillation in the nanostructures can be simulated as a multipole with an electric field in free space [17, 24, 68]. As a result, the interaction area of E_{WG} and E_{Pl} is not restricted to the positions of the metallic nanostructures. The coupled system of particle plasmon and quasiguided mode shows a rather complex near-field distribution of the electromagnetic field, as was found by near-field optical microscopy [69]. Therefore, the interaction of E_{WG} and E_{Pl} is more complicated and requires a more detailed theory.

However, this model is able to describe the effects in our disordered systems in a good and reasonable approximation. Its results can be used to simulate the influence of disorder on the polariton splitting E_{PS} and will be used in the next sections. A schematic overview on the influence of V_2 for TM polarization is presented in Fig. 5.9. Here, the dispersion $E(k)$ was calculated for different V_2. Decreasing V_2 reduces E_{PS} at momentum k_{PS}, for $V_2 = 0$ the uncoupled system of plasmon and quasiguided mode is observed (for comparison see Fig. 2.9). Hence, we expect that increasing disorder reduces the splitting between the polariton branches. The energy shift of the dispersion depends on the detuning of plasmon and quasiguided mode. For strong deviations of k from k_{PS}, the energy shift due to the modified V_2 is smaller than for the k-range around k_{PS}. This should also hold for the observed reduction of the energy separation in TM polarization. According to Fig. 5.8, this effect should be stronger for long-range than for frozen-phonon disorder. Similarly, a Gaussian distribution $D(\Delta x)$ of the nanowires' variation influences the splitting stronger than a uniform distribution.

5.5 Theoretical modelling of the disorder results

In this section we want to develop a theoretical model that can reproduce the experimental results and that can help to gain a deeper insight into the physical effects. The theory is divided into three parts: the Fourier analysis of the spatial arrangement of the nanostructures, the dispersion $E(k)$ of the metallic photonic crystal slabs, and the typi-

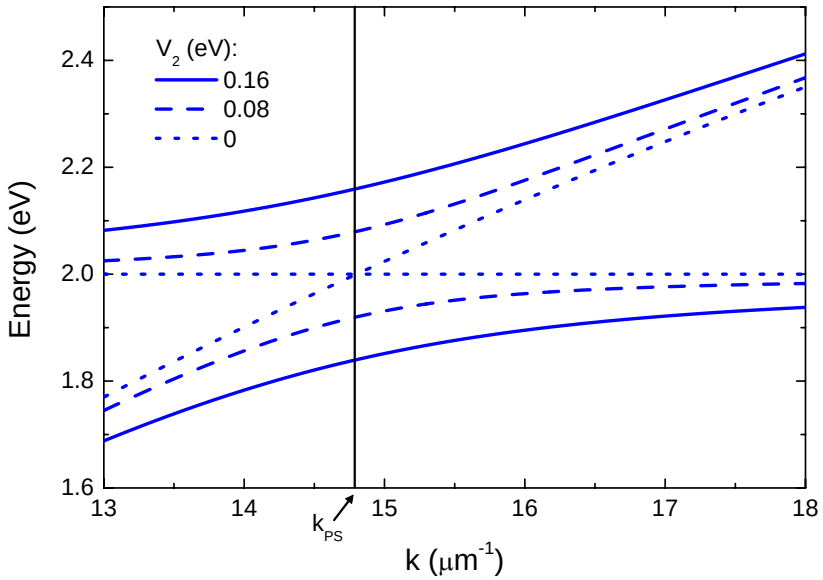

Figure 5.9: TM dispersion $E(k)$ for different coupling parameters V_2. $E(k)$ was calculated with Eqn. (2.26) and $E_{Pl} = 2.0$ eV. $k = 15\ \mu m^{-1}$ corresponds to a period of $d_0 \approx 420$ nm.

cal extinction lineshapes in TE and TM polarization. The dispersion $E(k)$ includes the disorder-dependent coupling parameter V_2 for TM polarization, according to Eqn. (5.6). Figure 5.10 can be used to follow the explanation of the following steps.

Given a periodically modulated waveguide without disorder, the coupling of modes in the waveguide and the surrounding media can be calculated [70, 71]. We have seen that the energy E of a quasiguided mode is a function of its momentum k; this relation is described by the dispersion $E(k)$. For a modulated waveguide, the incoming light field can couple to a mode inside the waveguide. For normal light incidence, the excited quasiguided modes have momenta k that are determined by the Fourier components at $k_n = \pm n \cdot 2\pi/d_0$ ($n \in \mathbb{N}$) and hence by the period d_0 of the system [62, 72]. Therefore, multiple quasiguided modes at different energies $E(k_n)$ can be excited in such a configuration.

A part of the incoming light is diffracted into the waveguide layer and excites the quasiguided mode. The amplitude of the diffracted beam is proportional to the amplitude A_j of the Fourier component at k_j [72]. From diffraction theory it is known that the intensity is given by $I_j \propto A_j^2$ [64]. Hence, combining Fourier analysis of the grating arrangement and dispersion $E(k)$ of the structure yields a transformation of the Fourier peaks from k-space into energy space: each Fourier component with momentum k_j and amplitude A_j excites resonances with energies $E_j = E(k_j)$ and strengths $I_j \propto A_j^2$. In TE polarization, each Fourier component excites a resonance with energy E_j^{TE} and amplitude I_j^{TE}. Due to the coupled system of plasmon and quasiguided mode in TM polarization, each Fourier component excites two resonances at E_j^{Pl} and E_j^{WG} with amplitudes I_j^{TM}. For simplicity we restrict to the k-range around the first Fourier component. This is reasonable as the energies of the resonances at $E(k_n)$ with $n > 1$ are outside the visible

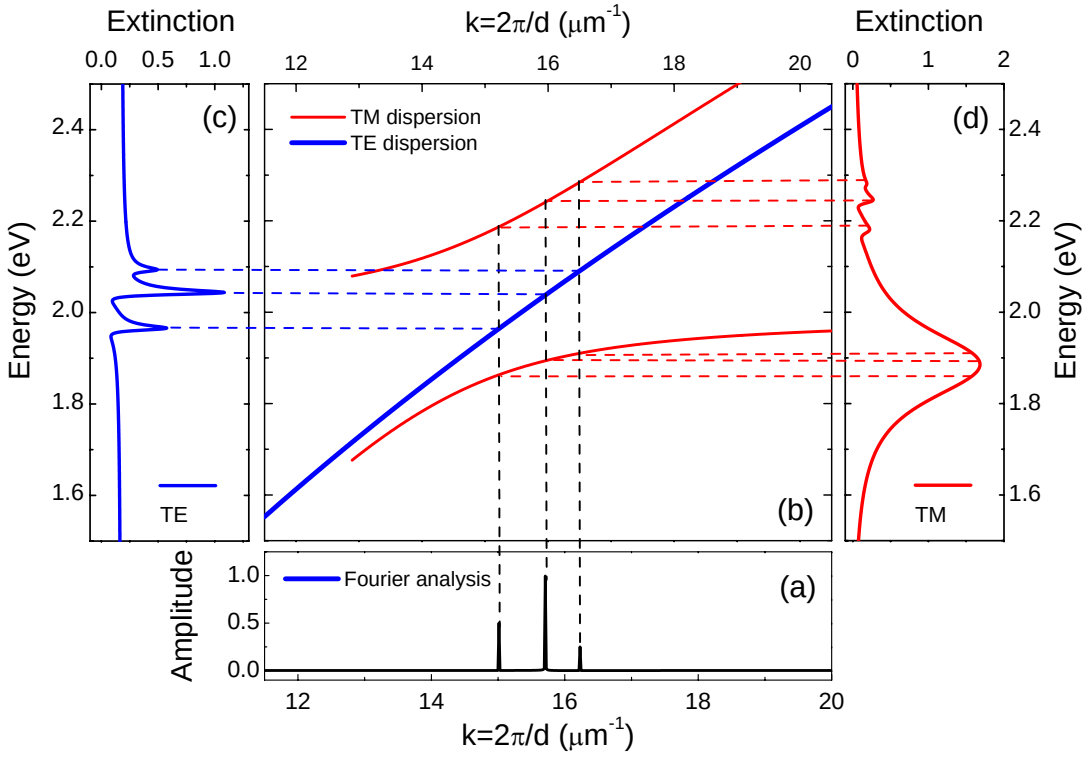

Figure 5.10: Scheme of the theoretical model for TE and TM polarization. (a) The Fourier analysis of the spatial grating arrangement shows components at k_j. (b) These momenta are transferred via the dispersion $E(k)$ from k-space into energy-space. Each Fourier component with momentum k_j and amplitude A_j yields resonances with energy E_j and amplitude $I_j \propto A_j^2$. (c),(d) Integrated TE and TM extinction, respectively.

spectral range that is considered in this work.

Let us discuss the consequences for a perfectly ordered system. Its Fourier decomposition in the visible spectral range consists of a δ-shaped peak at $g_0 = 2\pi/d_0$. Hence, this δ-peak in k-space is transferred into a δ-peak in energy-space. For a perfectly ordered system, a single resonance with energy E_n and amplitude $I_n \neq 0$ is excited in TE polarization. All other resonances have amplitudes $I_j = 0$ due to the Fourier components at k_j with $A_j = 0$. In TM polarization, two resonances are excited for this configuration.

We need an analytical function to compute the model results here. Therefore, we use the following expressions in the calculations, see Chapter 2. The typical extinction lineshape $\alpha_j(E)$ can be described by a Fano form in TE polarization

$$\alpha_j^{TE}(E) = I_j^{TE} \frac{\left(\frac{2(E-E_j^{TE})}{\gamma} + q\right)^2}{\left(\frac{2(E-E_j^{TE})}{\gamma}\right)^2 + 1}. \tag{5.7}$$

A coupled oscillator model gives the absorption in TM polarization [40]. For simplicity,

we identify the extinction with this absorption:

$$\alpha_j^{TM}(\omega) = I_j^{TM} \frac{4\gamma_{Pl}^2\omega^2\left[\omega^2 - (\Omega_j^{WG})^2 - (q_{WG}/q_{Pl})\Omega_C^2\right]^2}{\left[\left(\omega^2 - (\Omega_j^{Pl})^2\right)\left(\omega^2 - (\Omega_j^{WG})^2\right) - \Omega_C^4\right]^2 + 4\gamma_{Pl}^2\omega^2\left(\omega^2 - (\Omega_j^{WG})^2\right)^2}, \quad (5.8)$$

with $\Omega_j^{WG} = E_j^{WG}/\hbar$ and $\Omega_j^{Pl} = E_j^{Pl}/\hbar$. We therefore insert E_j^{TE} and I_j^{TE} as parameters in the Fano form, and E_j^{Pl}, E_j^{WG}, and I_j^{TM} in the lineshape function in TM polarization. Each Fourier component at k_j yields an extinction $\alpha_{Dis}^{pol}(E)$, where *pol* denotes the polarization (TE and TM). The total extinction $\alpha_{Dis}^{pol}(E)$ of the disordered sample is the summation over all lineshape functions $\alpha_j^{pol}(E)$

$$\alpha_{Dis}^{pol}(E) = \sum_j \alpha_j^{pol}(E). \quad (5.9)$$

E_j and A_j only determine energy and amplitude of the excited resonances, though. Form and shape are given by additional parameters in these equations. We determine these parameters by fitting the typical lineshapes to the measured extinction spectra of the perfect samples. These parameters are then used as constant, disorder-independent parameters in the calculation of $\alpha_j^{pol}(E)$ and $\alpha_{Dis}^{pol}(E)$. The steps of the model are drawn schematically in Fig. 5.10, see also Appendix C. Taking into account Fig. 5.9 it becomes clear in this simple model, that disorder reduces the energy separation between the TM polariton branches due to a modified V_2. This reduction depends on the detuning of plasmon and quasiguided mode. We should also mention that the coupling Ω_C could reduce with V_2. However, we leave this discussion open for future work.

On the following pages, several comparisons of measured and simulated extinction spectra are presented. We will start with the influence of the disorder-dependent coupling parameter V_2 on the extinction in TM polarization. Measured spectra of sample D11 (Gaussian frozen-phonon disorder) are compared to simulations with a constant and with a disorder-dependent V_2, respectively, see Fig. 5.11. The experimental data were already described and discussed above. We notice a nice agreement, the simulated results reproduce the experimental spectral features very well. For the case of no disorder, the coupled system of plasmon and TM quasiguided mode appears as two resonance peaks in the extinction. The influence of Gaussian frozen-phonon disorder on the extinction spectra of sample D11 is clearly reflected in the simulations. The polariton branch at lower energies is nearly unaffected, while the amplitude of the upper polariton branch reduces for increasing disorder and vanishes for 60-70% disorder - both in experiment and simulation. Both show no significant inhomogeneous broadening of the resonances.

In the experiments, a decrease of the energy separation between the polariton branches can be observed. It is caused by shifts of the lower polariton branch to higher energies and of the upper polariton branch to lower energies. When looking at the simulations it can be seen that both a constant V_2 and a disorder-dependent V_2 increase the energy of

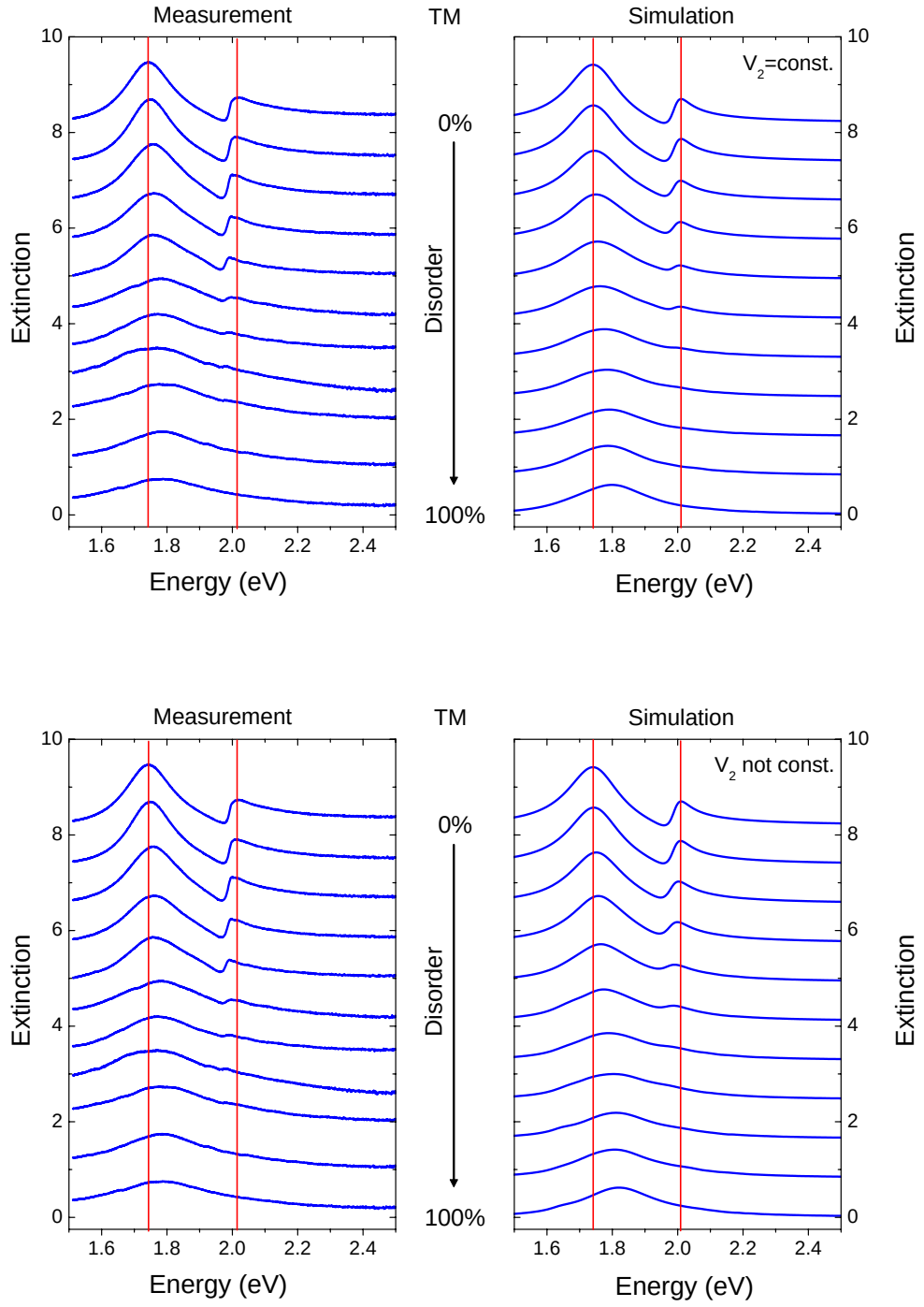

Figure 5.11: Comparison of measured and simulated TM extinction spectra of sample D11 (Gaussian frozen-phonon disorder) in TM polarization. Upper panel: Calculation with $V_2 = \text{const}$. Lower panel: Disorder-dependence of V_2 according to Eqn. (5.6). The vertical lines mark the resonance energies for no disorder.

the lower branch. The shift of the upper branch, however, is only reproduced by a non-constant V_2. This observation is confirmed by the data in Fig. 5.12, where the polariton splittings of Fig. 5.11 are plotted as a function of disorder. The results obtained with a

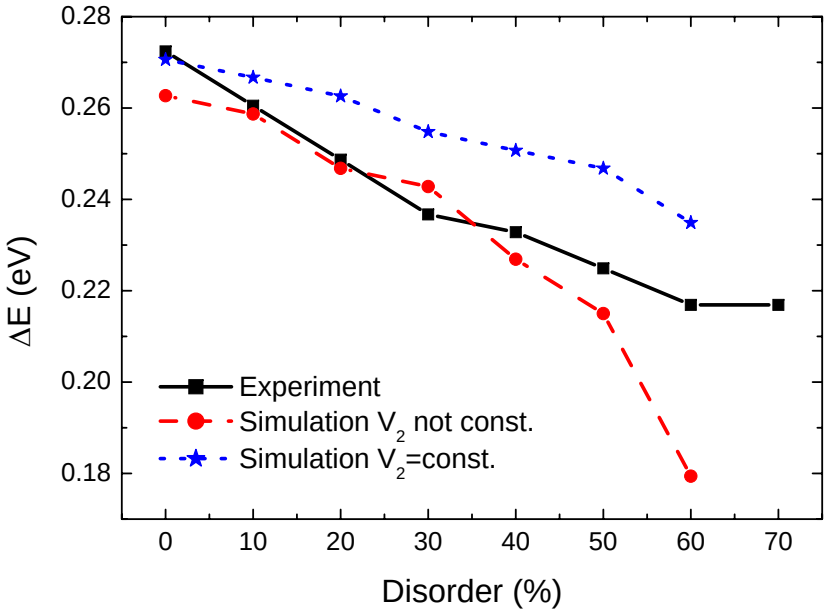

Figure 5.12: Comparison of measured and simulated polariton splitting of sample D11 (Gaussian frozen-phonon disorder). The data were obtained from Fig. 5.11.

disorder-dependent V_2 show a reduction of the splitting that is close to the experimental findings up to 50% disorder. Deviations at larger disorder amounts are caused by uncertainties in determining the energy of the hardly visible upper polariton branch. Contrary, the splitting derived from the model with a constant V_2 shows deviations nearly in the whole disorder range. We conclude that a disorder-dependent V_2 reproduces very well the experimental results concerning the influence of disorder on the polariton splitting in TM polarization. In the following, we will always include the disorder-dependent V_2 in the simulations.

The next figures show a comparison of experiment and simulation for TE and TM polarization, where different disorder types are considered. The results of sample #95 (uniform frozen-phonon disorder) are plotted in Fig. 5.13. In TE polarization, the typical Fano form of the quasiguided mode appears in the simulation, as determined by the calculation process. Increasing uniform frozen-phonon disorder reduces the amplitude of this resonance, as in the experiment. The peak vanishes for a disorder amount of about 90%, indicating that the quasiguided mode is no longer excited. The slight shift of the resonance to lower energies in the experiment is not reproduced in the simulations, because the disorder influence on the TE bandstructure [59] was not included in the theory. Also shown are the results for TM polarization. Again, the simulation agrees well with the experiment. Both the reduction of the amplitude of the upper polariton branch and the decreasing of the polariton splitting are nicely reproduced. The upper branch vanishes for a disorder amount of 80-90%, which is more than for Gaussian frozen-phonon disorder. Also the simulations indicate that a uniform distribution requires a larger disorder amount

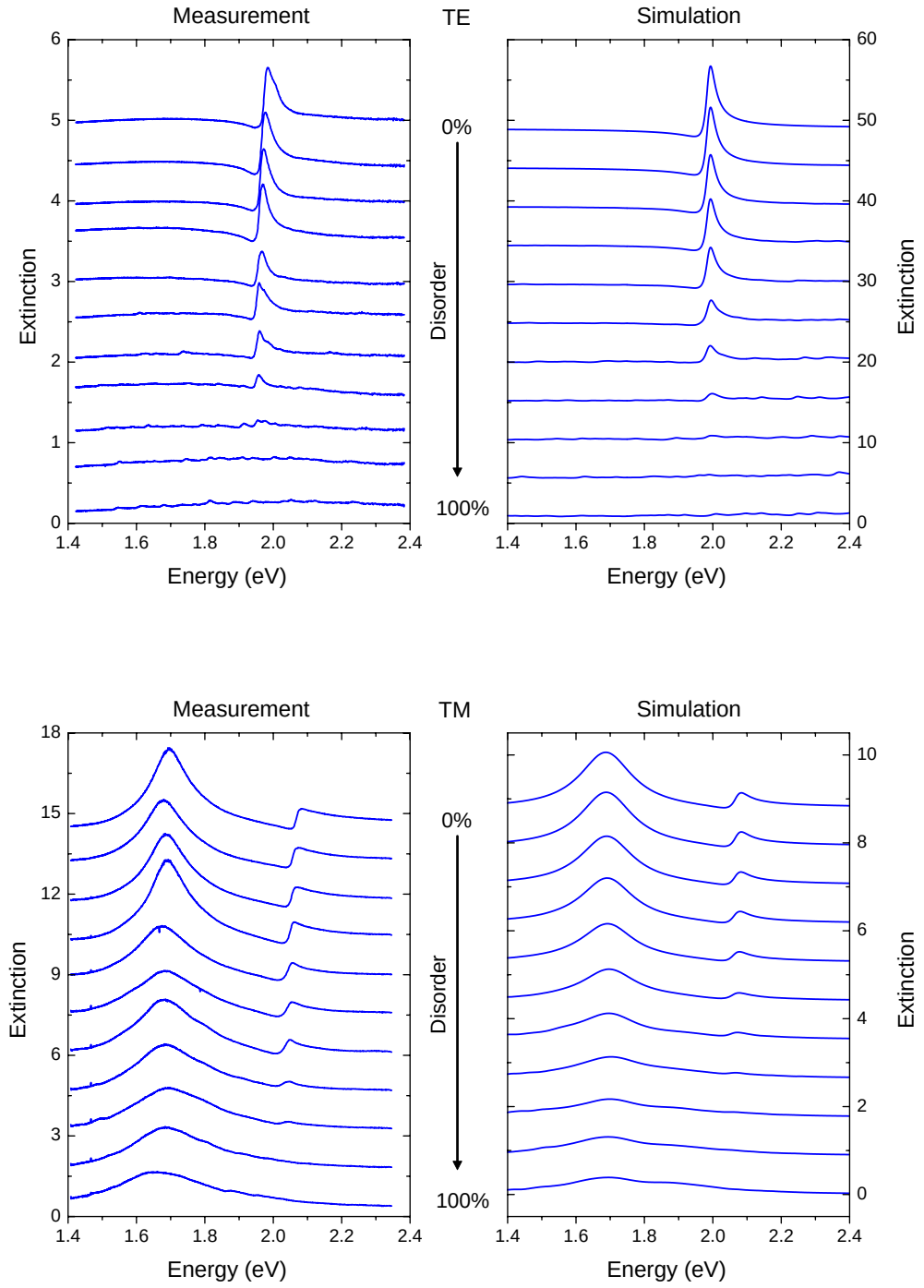

Figure 5.13: Comparison of measured and calculated extinction spectra of sample #95 (uniform frozen-phonon disorder). Upper panel: TE polarization. Lower panel: TM polarization.

than a Gaussian distribution for the same spectral effect.

In addition to the simulations for TM polarization (Fig. 5.11), also the model calculation for TE polarization for sample D11 (Gaussian frozen-phonon disorder) reflect the measurements as shown in Fig. 5.14. The vanishing of the TE quasiguided mode reso-

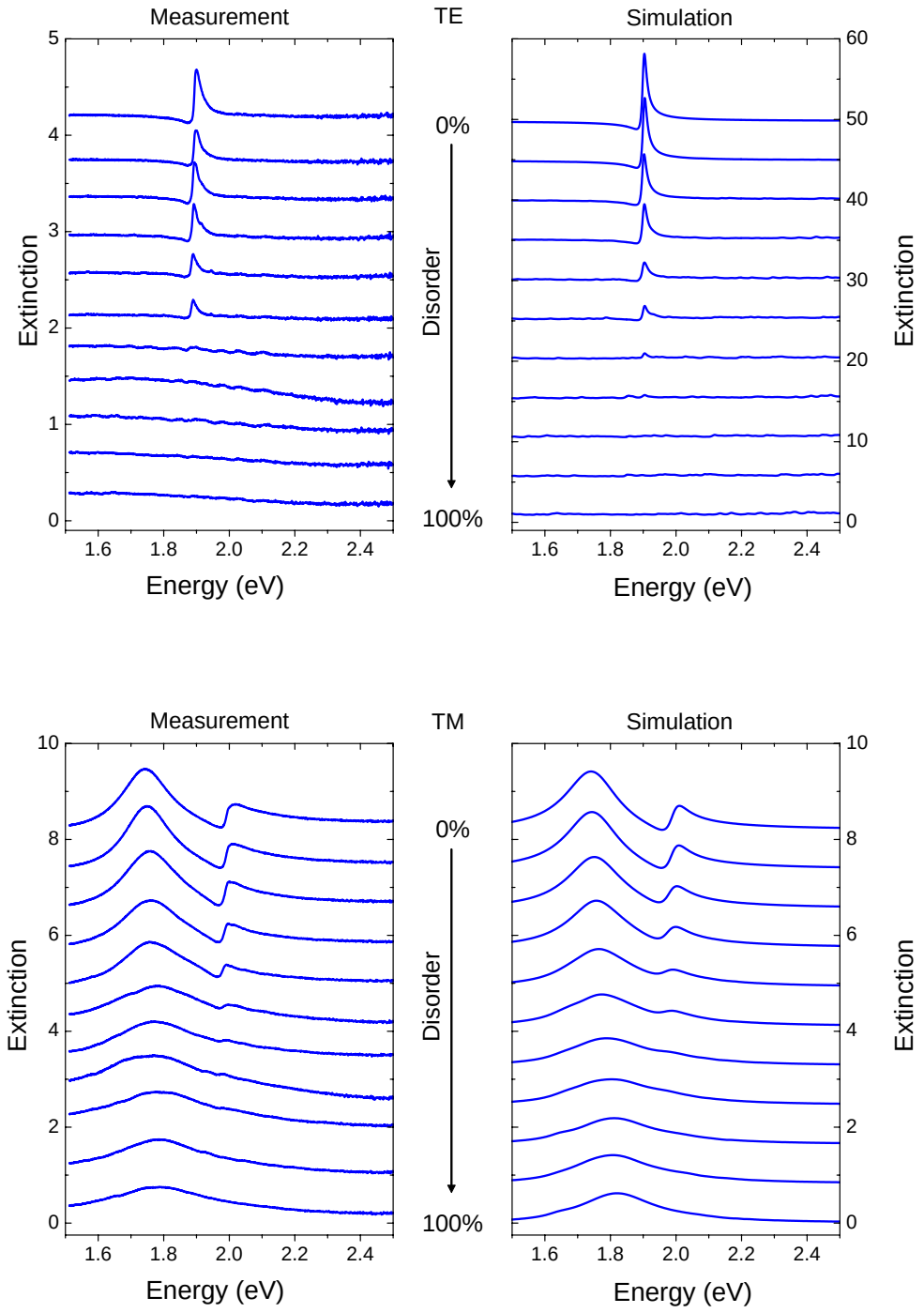

Figure 5.14: Comparison of measured and calculated extinction spectra of sample D11 (Gaussian frozen-phonon disorder). Upper panel: TE polarization. Lower panel: TM polarization.

nance appears for a disorder amount of 60-70%, which is again less than for a uniform distribution as expected.

Now, the results for the long-range disorder shall be analyzed. Here, an additional inhomogeneous broadening can be observed, contrary to the frozen-phonon disorder case.

Figure 5.15 presents the results for sample D12 (uniform long-range disorder), and Fig. 5.16 for sample #117 (Gaussian long-range disorder). The TE quasiguided mode reduces its amplitude for increasing long-range disorder and vanishes for 40-50% Gaussian and 60-70% uniform long-range disorder, respectively. The inhomogeneous broadening in experiment and simulation shows a good match. Not only the modified and irregular shapes of the resonance are reproduced nicely in the simulations, but also the correct shifts of the maximum to lower and higher energies can be observed. Both polariton resonances are influenced by long-range disorder in TM polarization. They show a substructure of maxima and minima in the experiment that causes an inhomogeneous broadening by this type of positional disorder. However, the simulated broadening does not describe the experimental results completely. For some reason, this substructure is more pronounced in the experiment.

The experimental and simulated observations can be understood when taking the Fourier analysis of different disorder types into account. A perfect grating arrangement shows pronounced δ-shaped peaks at multiple integers of the reciprocal lattice vector g_0, as described in Chapter 4. Increasing frozen-phonon disorder reduces the amplitude of this peak, whereas its width is kept unaffected. Long-range disorder also reduces the amplitude of the peak at $k = g_0$. Additionally, the Fourier transformation of the long-range disorder shows components in a widespread k-range around $k = g_0$, causing an inhomogeneous broadening of the resulting Fourier distribution. In order to simulate the extinction in our model, each Fourier component with momentum k_j and with amplitude A_j is expected to excite resonances at energies E_j and with amplitude $I_j \propto A_j^2$. Hence, frozen-phonon disorder only reduces the amplitude of the excited resonances. Multiple quasiguided modes in a wide energy range are excited by long-range disorder, causing the resulting resonance to be inhomogeneously broadened. As shown in Fig. 4.6, the effect is increased by a Gaussian distribution compared to a uniform distribution. For a given FWHM, the range of a Gaussian distribution is larger than the range of a uniform distribution. As a result, the positions of the nanowires can deviate stronger from the perfect grid at a certain disorder amount. This explains the unequal disorder amount that causes the same spectral effects in Gaussian and uniform distribution.

The inhomogeneous broadening is more pronounced in the experiment than in the simulations, see Figs. 5.15 and 5.16. Two possibilities may be the reason for the discrepancies. First, the substructure is an artefact from the sample fabrication that probably introduced some undesired disorder in the shape of the metallic nanowires. This would result in shifted plasmon energies and hence in changed polariton resonances. Second, our theoretical model does not describe the TM extinction spectra correctly in every detail. The considerations for transferring the Fourier decomposition of the spatial grating arrangement from k-space into energy-space were originally performed for the excitation of quasiguided modes. The correspondence of the results obtained with this model and the experimental data is very well in TE polarization. However, here we extend this model to the excitation of a coupled system of particle plasmon and quasiguided mode

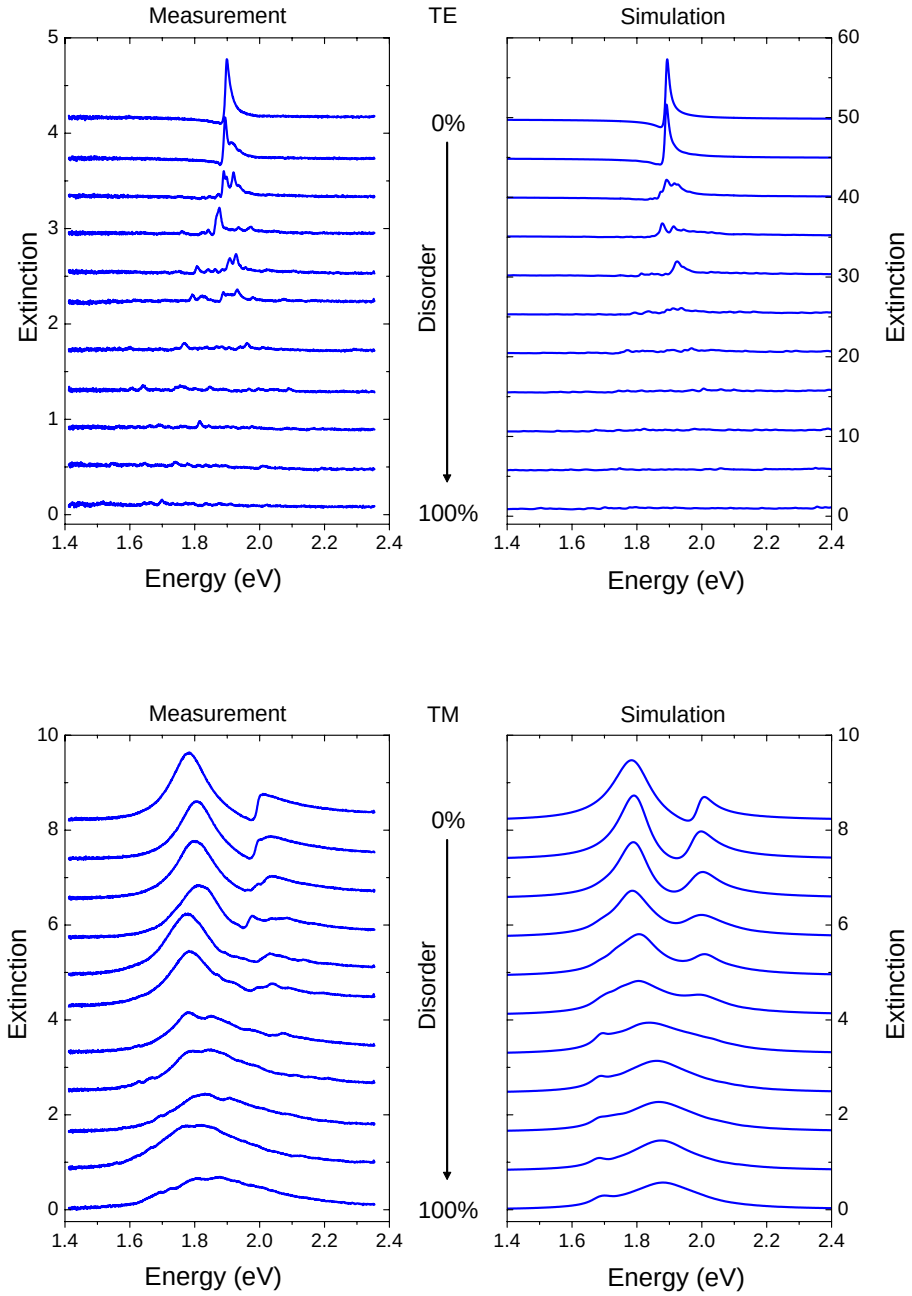

Figure 5.15: Comparison of measured and calculated extinction spectra of sample D12 (uniform long-range disorder). Upper panel: TE polarization. Lower panel: TM polarization.

in TM polarization. Especially the treatment of the plasmonic polariton branch should be considered critical, because the plasmon excitation is independent of the period and hence the Fourier decomposition of the grating. To give a final answer to the question of the validity of the model in TM polarization, a comparison of experiment and simulation for several different samples would be necessary.

To conclude, both the reduction of the extinction of the resonances as well as the

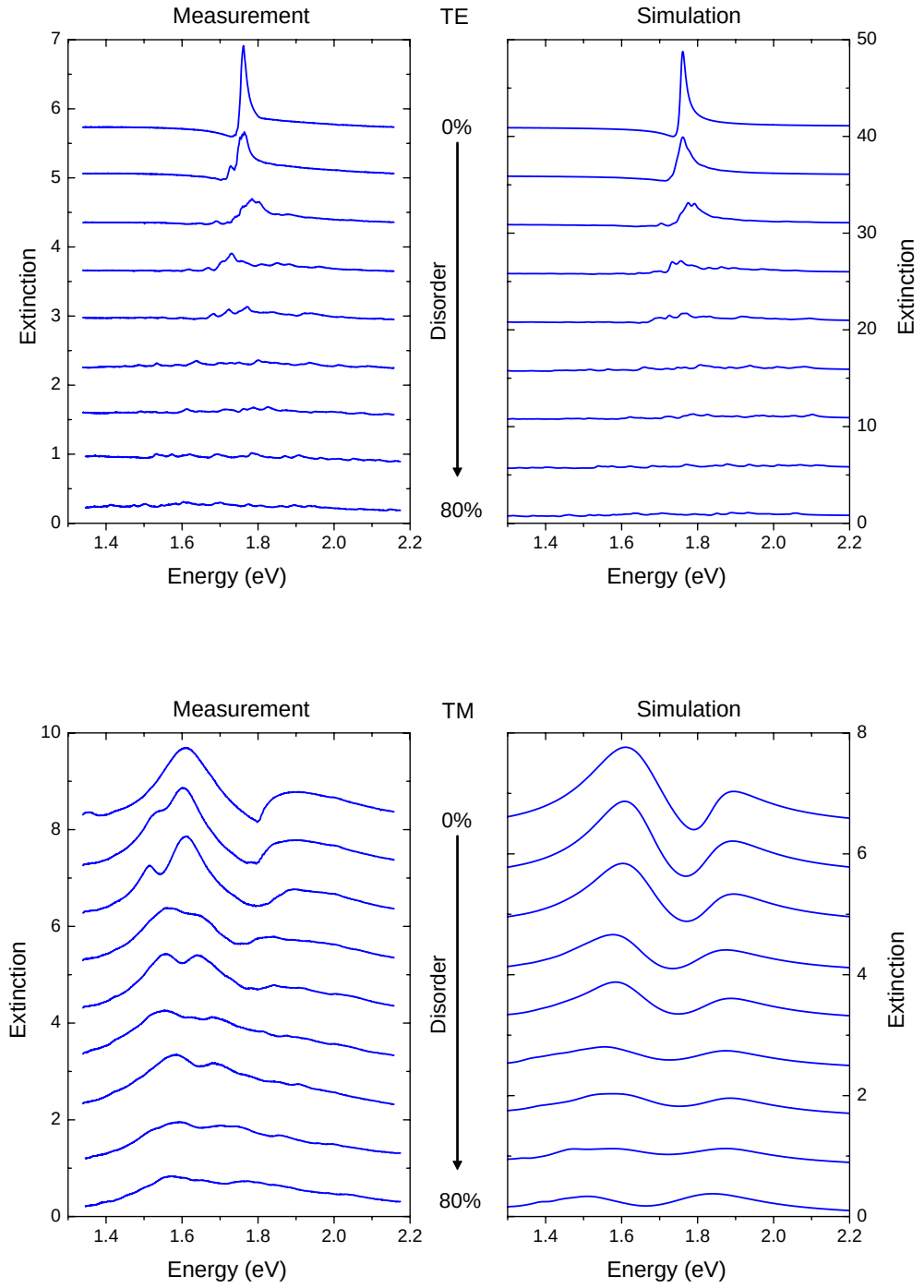

Figure 5.16: Comparison of measured and calculated extinction spectra of sample #117 (Gaussian long-range disorder). Upper panel: TE polarization. Lower panel: TM polarization.

inhomogeneous broadening are reproduced by our theoretical model. While the agreement is very well in TE polarization, not all details are not correctly simulated in TM polarization. However, the main differences between the disorder types can be identified clearly in the considered model results.

5.6 Angle-resolved extinction spectra

The dispersion of a sample can be probed by angle-resolved measurements. Rotating the angle of light incidence φ varies $k_x = k_0 \sin\varphi$ and hence the energy according to the dispersion $E(k_x)$, see Eqn. (5.10). The bandstructure of the samples is determined by plotting the energies of the resonances as a function of the angle of incidence φ or alternatively of k_x.

Figure 5.17 shows the dispersion of sample #95 (uniform frozen-phonon disorder) in TM polarization. Clearly, the bandstructure of the polariton can be observed in the case of no disorder. It consists of pronounced bands that are separated by gaps. The bands correspond to lower, middle, and upper polariton branch. Increasing uniform frozen-phonon disorder reduces the gaps between the bands. The splitting between the middle and upper polariton branch vanishes for a disorder amount of about 60%, and the splitting between upper and lower branch reduces continuously. The bandstructure itself is retained and not destroyed by this type of disorder. Even for large disorder amounts of up to 70% the bands of the different polariton branches are distinguishable. For still larger amounts (80% and more) the quasiguided modes are not excited any more, as was shown in Fig. 5.1. Thus, only the plasmonic polariton branch appears (not shown here).

The dispersion of sample #117 with Gaussian long-range disorder is plotted in Fig. 5.18. For no disorder, the polariton dispersion can be observed. Increasing disorder starts to wash out the bandstructure, an amount of 30% and higher completely destroys the polariton branches. No bandstructure is retained, and further structures appear, causing the original polariton branches to be inhomogeneously broadened. As for normal light incidence, we can attribute the excitation of multiple quasiguided modes at different energies to be responsible for this effect. Each mode leads to the formation of a polariton with slightly different energies and slightly shifted dispersion. The resulting dispersion of the sample leads to the complete vanishing of pronounced polariton branches.

Figure 5.19 presents the measured bandstructure of sample #95 together with simulations that were performed by using the effective energy Hamiltonian from Chapter 2

$$H_{eff} = \begin{pmatrix} E_0 + V_1 - i(\gamma + \gamma_1) & \tilde{c}k_x & \sqrt{2}V_2^{mod} \\ \tilde{c}k_x & E_0 - V_1 - i(\gamma - \gamma_1) & 0 \\ \sqrt{2}V_2^{mod} & 0 & E_{Pl} - i\Gamma \end{pmatrix}. \tag{5.10}$$

These simulations include the disorder-dependent coupling parameter V_2^{mod} in the effective energy Hamiltonian to describe the bandstructure of MPCS, see Eqn. (5.6). The bandstructure agrees well in experiment and simulation, as can be seen in Fig. 5.19. Increasing frozen-phonon disorder retains the dispersion branches of the polariton, the splittings between the bands is reproduced nicely by the simulations.

Determining the bandsplittings from Fig. 5.17 yields a direct comparison of experiment and simulation. The results are presented in Fig. 5.20, where the splittings between

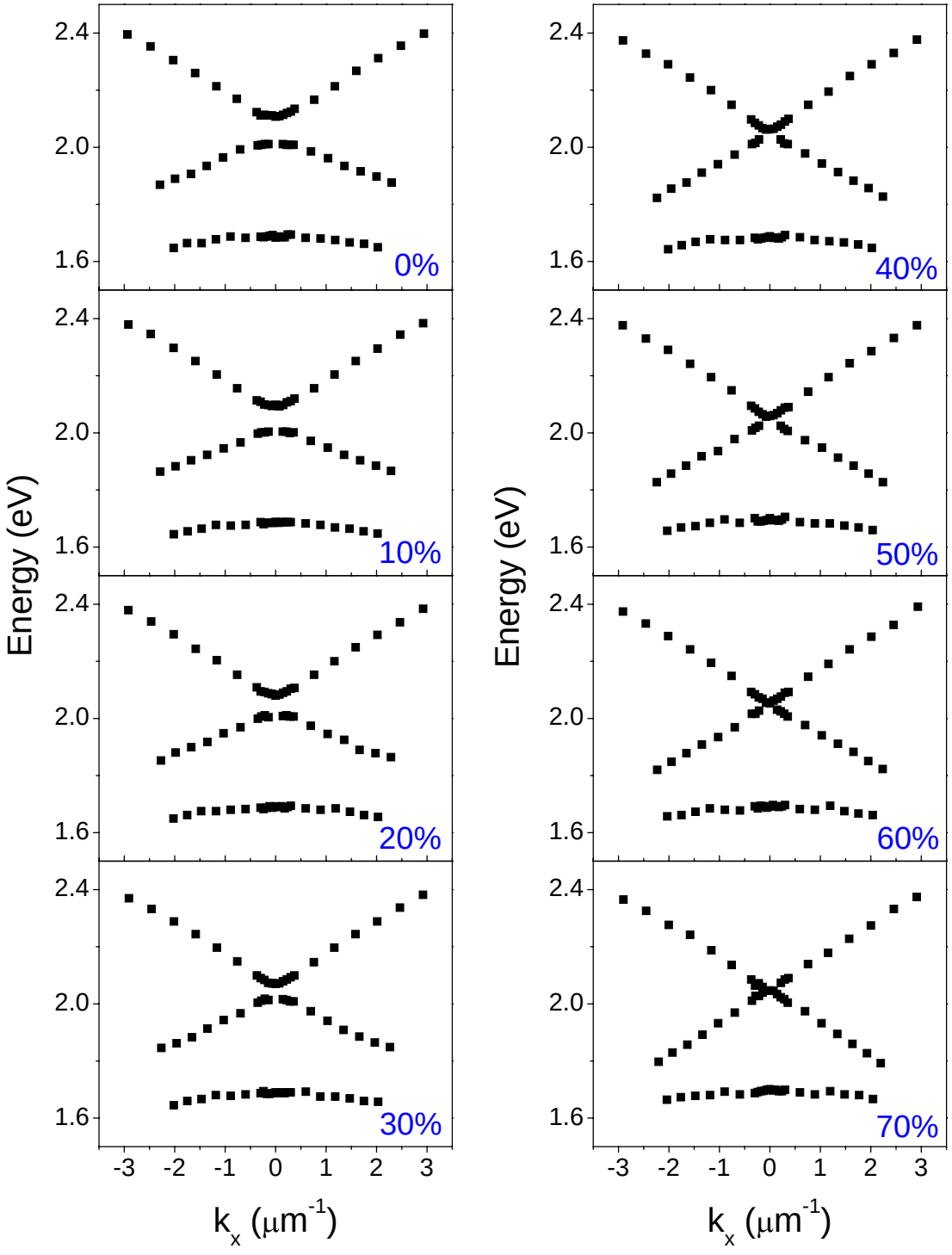

Figure 5.17: Dispersion of sample #95 with increasing uniform frozen-phonon disorder as determined by angle-resolved measurements in TM polarization.

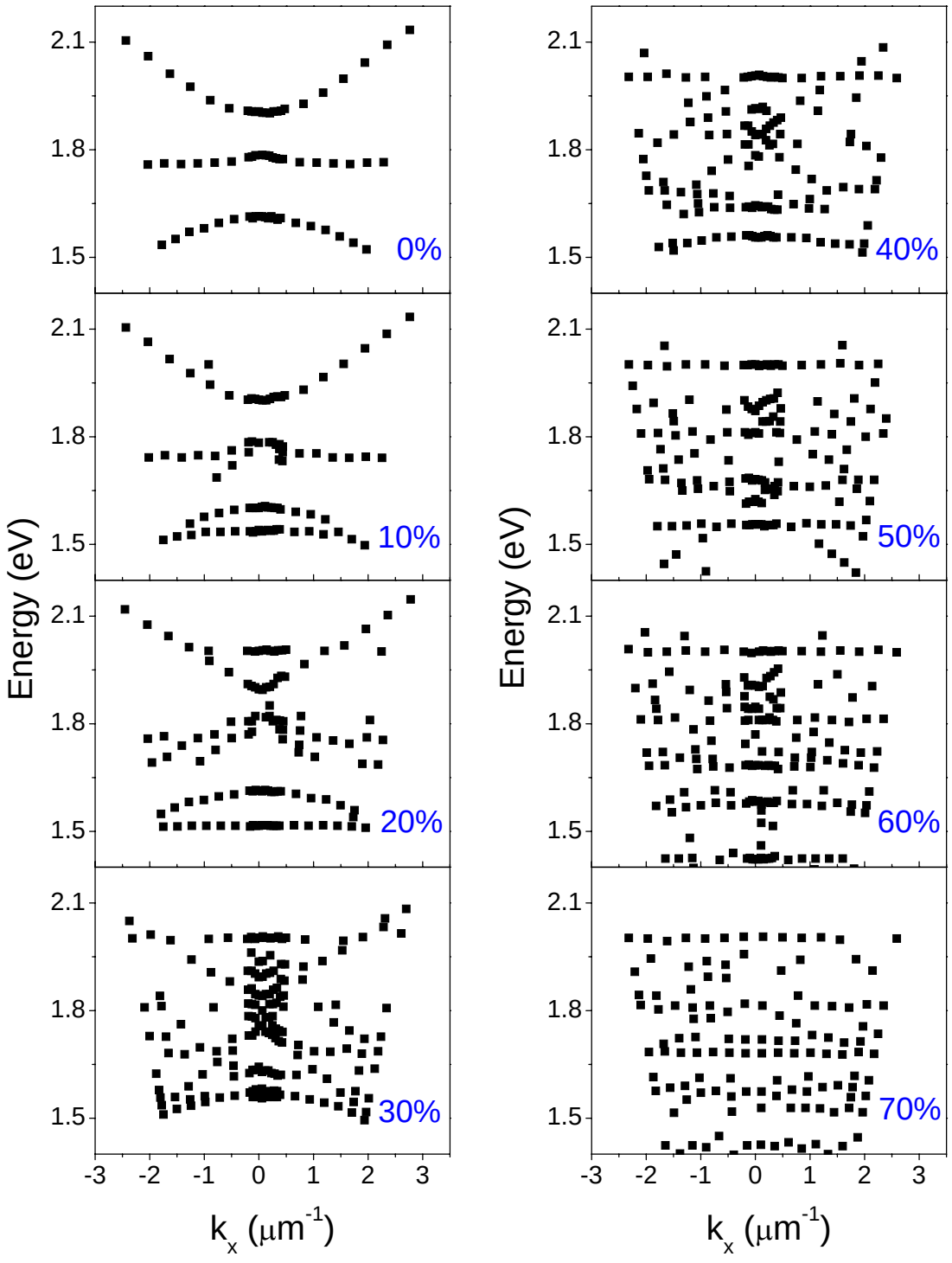

Figure 5.18: Dispersion of sample #117 with increasing Gaussian long-range disorder as determined by angle-resolved measurements in TM polarization.

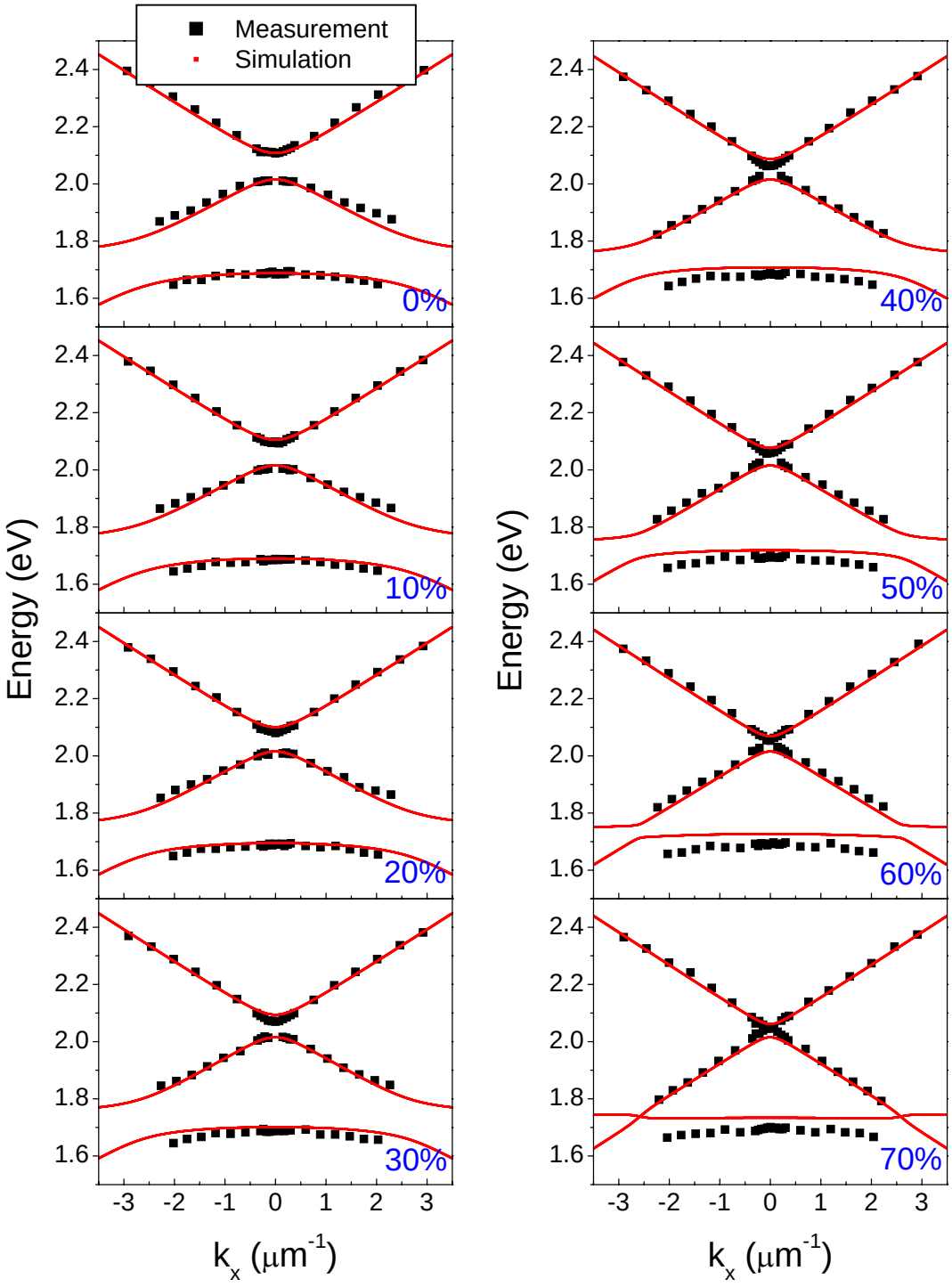

Figure 5.19: Dispersion of sample #95 with uniform frozen-phonon disorder: experiment and simulation in TM polarization. The bandstructure is plotted for increasing amounts of disorder. The simulations were performed by using Eqn. (5.10).

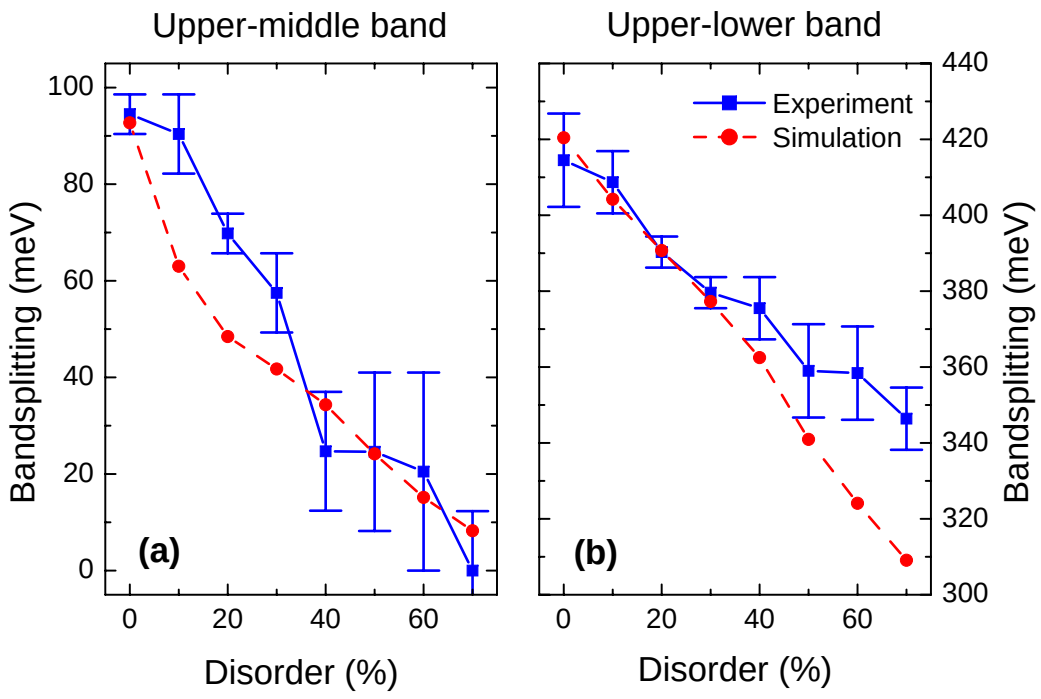

Figure 5.20: Splitting between upper and middle band (a) and between upper and lower band (b) in the dispersion of sample #95 with uniform frozen-phonon disorder in TM polarization. Experimental and simulated data were obtained from Fig. 5.19.

upper and middle and also between upper and lower band in the polariton dispersion are plotted. The simulated results do not show perfect agreement with the experimental data. On the one hand, the simulated splitting between *upper* and *lower* band agrees well with the experimental data for disorder amounts of less than 40%; the deviations become stronger for larger disorder amounts. On the other hand, we observe a good agreement of experiment and simulation for the splitting between *upper* and *middle* band at these large disorder amounts of more than 40%. Here, the discrepancies are larger for disorder amounts of less than 40%. This again proves that the presented model for calculating the bandstructure in disordered metallic photonic crystal slabs has some weaknesses, although the similarities between experiment and simulation in Fig. 5.20 are good. Besides the above mentioned simplifications in the calculation of V_2^{Dis}, we completely neglected the possible influence of disorder on the splitting between the branches of symmetric and antisymmetric quasiguided modes in TM polarization. To take this into account, we would have to describe V_1 as a function of disorder. But so far, no intuitive model exists to simulate this dependency.

So far, we only considered the bandstructure in TM polarization. Now we want to focus on TE polarization. For an angle of light incidence $\varphi \neq 0$, symmetric and anti-symmetric quasiguided mode appear in the extinction spectrum and allow to determine the bandstructure of the quasiguided mode. In the perfectly ordered system this consists of two pronounced bands corresponding to the dispersions of the two quasiguided modes [35, 38]. The results are qualitatively similar to the results obtained in TM polarization, as presented in Fig. 5.21. For sample #95 (uniform frozen-phonon disorder), the bandstructure is retained when the disorder is increased. Only the separation between the bands is reduced. This splitting is about 29 meV for the ordered system and vanishes for a disorder amount of 80%. Increasing Gaussian long-range disorder (sample #117) washes out the TE bandstructure. The Fourier decomposition of the spatial grating arrangement again explains that for this disorder type quasiguided modes at different energies and with different dispersions cause the inhomogeneous broadening of the resulting dispersion in TE polarization. As stated above, the parameter V_1 determines the separation of the bands in the dispersion of the quasiguided mode. As can be seen, V_1 decreases for increasing frozen-phonon disorder. A future model to describe the optical properties of metallic photonic crystals has to take this into account.

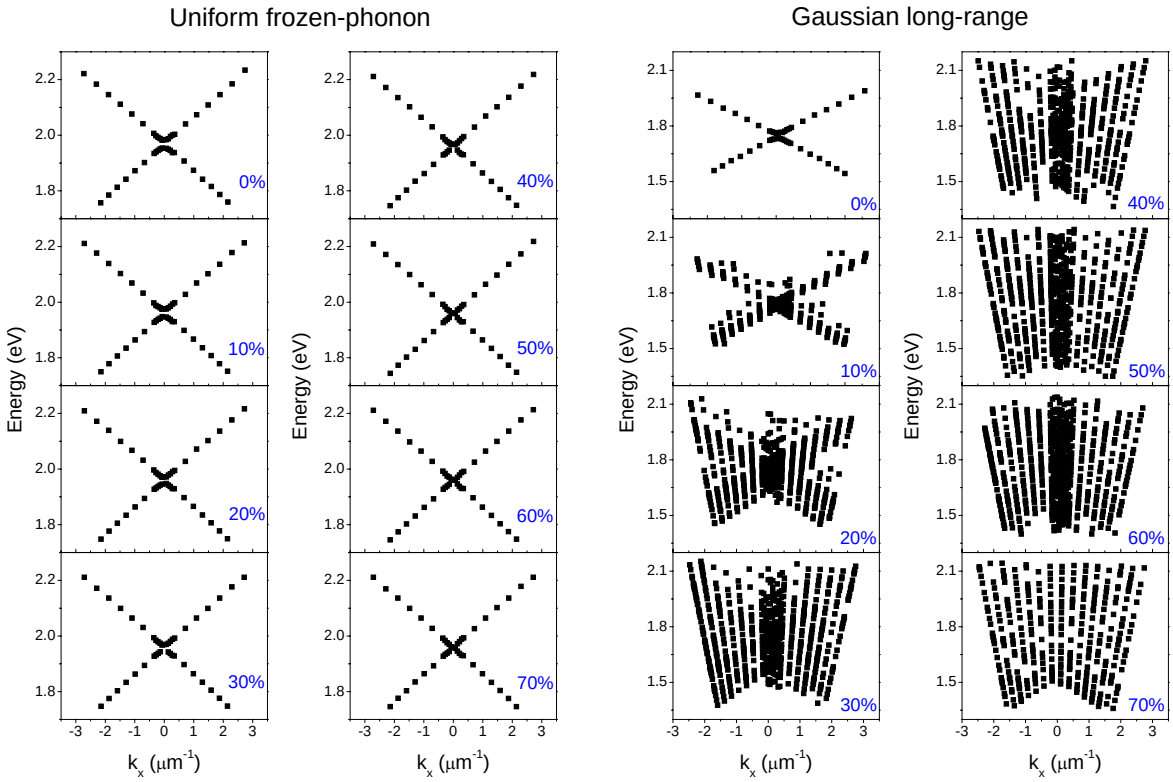

Figure 5.21: Experimentally determined dispersion in TE polarization. Left panel: sample #95 with increasing uniform frozen-phonon disorder. Right panel: sample #117 with increasing Gaussian long-range disorder.

5.7 Angular extinction spectra

A different method of coupling the transmitted light into the spectrometer enables a special way of mapping the extinction spectra. So far, we used pinholes in the light path to reduce the aperture angle on the sample surface to below 0.2°. Varying the angle of light incidence φ by rotating the sample in the focal point of the objective allows to scan the bandstructure. Removing one of the pinholes increases the aperture angle dramatically. For normal light incidence with an angle of aperture of about 3°, two quasiguided modes are excited simultaneously [8] (see also Ref. 7 in [9]). Hence, the angular information is no longer suppressed. It is possible to directly map this angular information onto the CCD array of the spectrometer by using a cylindrical lens to image the transmitted light onto the entrance slit of the spectrometer ([10], page 80). In our experiments, a cylindrical lens with a focal length of f = 100 mm was used, and a pinhole with a diameter of 800 μm in front of the sample reduced the size of the focal spot to approximately the dimensions of the grating array. With this setup, an angular range of $-2° < \varphi < 2°$ could be mapped onto the CCD array. Using a pinhole with larger diameter or working even without a pinhole would allow to further increase the mapped φ-range. The advantage of this method is its speed. Only one exposure process is required to map a wide energy and angular range and hence the bandstructure of a sample.

Typical results are presented in Fig. 5.22 and Fig. 5.23 for sample #95 and sample #117 in TE and TM polarization. The figures show the experimentally measured bandstructures in a 3-dimensional surface plot. The extinction is plotted as a function of the wavelength λ and of the angle of incidence φ. The bandstructure appears in the φ-λ-diagram. As can be seen, this way of presenting the bandstructure not only shows the influence of disorder on the bandsplitting. Additionally, the influence on the shape of the resonance is pointed out nicely. For no disorder, the undisturbed bandstructure appears in TE and TM polarization. As mentioned above, frozen-phonon and long-range disorder have different influence on the bandstructure. This can be deduced from Fig. 5.22 and Fig. 5.23. Increasing frozen-phonon disorder reduces the splitting between the bands as well as the amplitudes of the TE- and TM-quasiguided modes, whereas the general shape of the resonances is not affected. Clearly, the inhomogeneous broadening of the resonances for increasing long-range disorder can be observed. Additional resonances are excited whose bandstructures at slightly different energies lead to a smearing out of the overall bandstructure - both in TE and TM polarization.

5.8 Comparison with other systems

We have seen that different disorder types cause characteristic spectral features in our metallic photonic crystal slabs (MPCS), in the extinction at normal light incidence as well as in the dispersion. Frozen-phonon disorder reduces the amplitude of the excited quasiguided mode, whereas long-range disorder additionally broadens this resonance in-

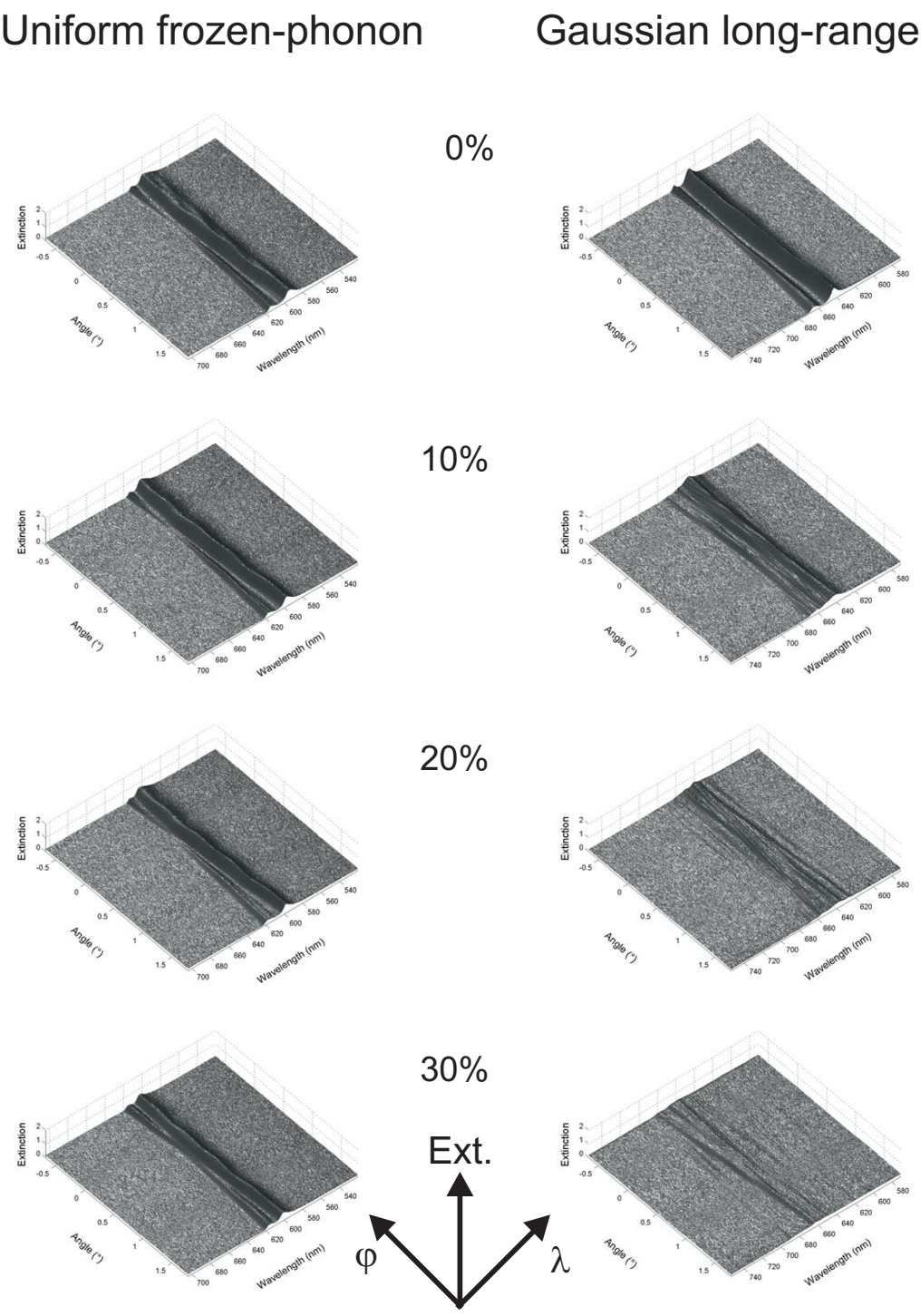

Figure 5.22: Angular extinction spectra for sample #95 (uniform frozen-phonon disorder) and sample #117 (Gaussian long-range disorder) for increasing disorder amounts in TE polarization. The extinction Ext is plotted as a function of the angle of light incidence φ and of the wavelength λ.

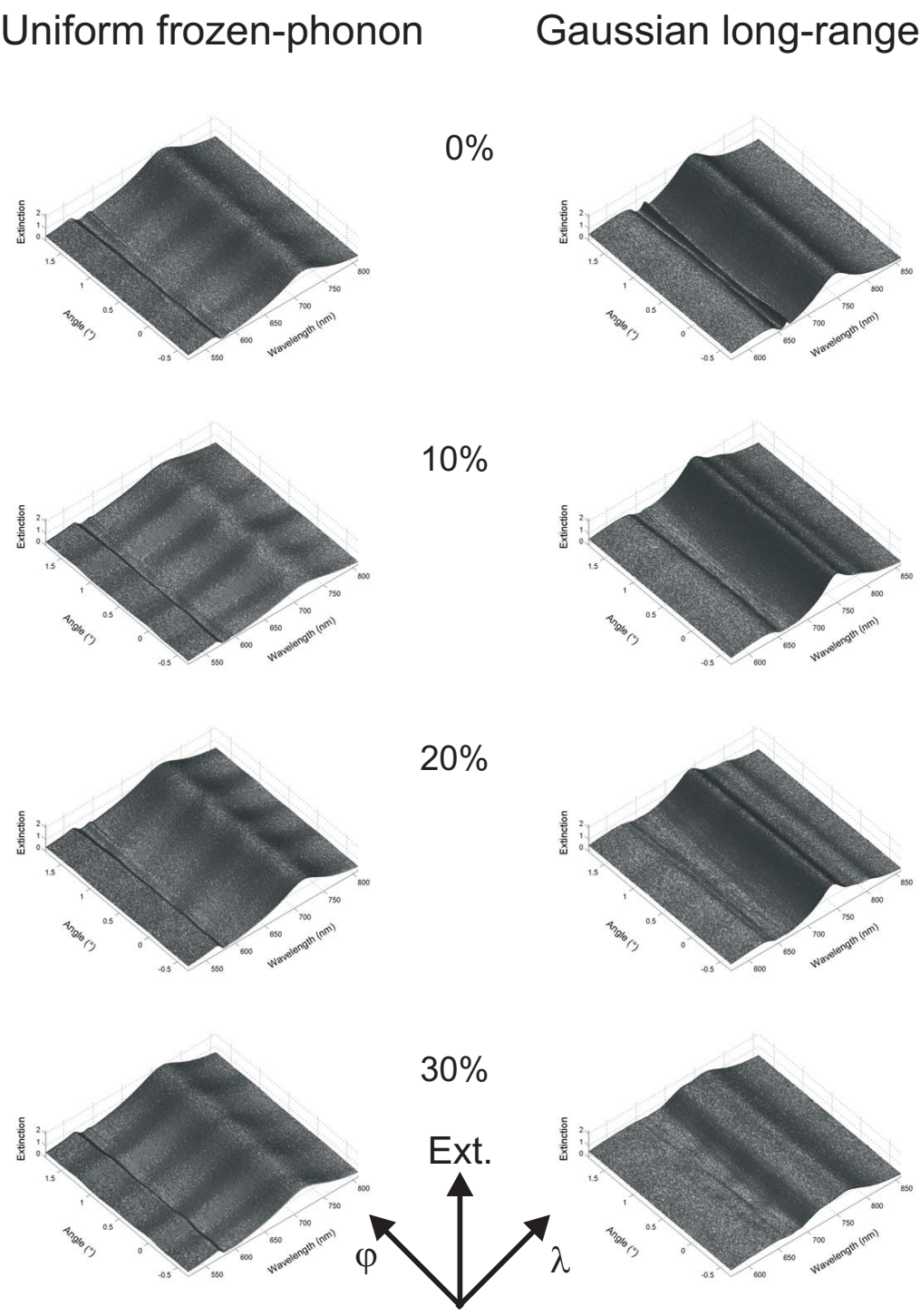

Figure 5.23: Angular extinction spectra for sample #95 (uniform frozen-phonon disorder) and sample #117 (Gaussian long-range disorder) for increasing disorder amounts in TM polarization. The extinction Ext is plotted as a function of the angle of light incidence φ and of the wavelength λ.

homogeneously by exciting several quasiguided modes at slightly different energies. The dispersion in TE and TM polarization is retained for frozen-phonon disorder, only a reduction of the bandsplittings is observable. This is caused by a reduced spatial overlap of the electrical fields of the resonances. However, the bandstructure is destroyed in systems with long-range disorder. Here, the dispersion of each of the quasiguided modes causes the total dispersion of the disordered system to be inhomogeneously broadened.

Now we want to compare these results with results from other systems. Contrary to our metallic photonic crystal slabs, semiconductors are materials whose dispersion $E(k)$ is determined solely by electronic resonances. Here, the motion and the masses of charge carriers (electrons and holes) are responsible for the formation of a bandstructure [16]. It is characterized by the valence band as highest completely filled and the conduction band as lowest unfilled band. Both are separated by an electronic bandgap E_G on the order of up to several eV. The optical and electronic properties of these materials are understood very well (see e.g. [73]). Because semiconductors are of large industrial interest, disorder and imperfections play a crucial role in these materials. Here, we want to compare our disorder models with types that appear in semiconductors.

The equivalence to frozen-phonon disorder are *phonons* in thermally hot semiconductors. They are quantized motions of the atoms around their equilibrium positions [16]. Since the bandstructure in solids is a result of the periodic arrangement of the atoms, it is reasonable that heating a solid and hence introducing phonons as lattice distortion should affect the bandstructure of solids. Exponential tails in the optical absorption, so-called Urbach-tails, are well known for amorphous and crystalline semiconductors [74, 75]. Figure 5.24 schematically draws the bandedge in ordered and disordered semiconductors. Tails appear in disordered materials and reduce E_G. In crystalline materials, they appear due to thermal occupancy of phonon states in the crystal. This was observed experimentally in [75] where a reduced E_G was found in heated solids. E_G as a function of the temperature T is plotted in Fig. 5.24. Comparing frozen-phonon disorder in our systems with the temperature in semiconductors shows that their effect on the bandsplitting is similar.

The pendant of metallic photonic crystal slabs with long-range disorder are amorphous materials. Their glass structure is characterized by a short-range order of the atomic arrangement [41]. In the scheme of Chapter 2, amorphous materials show positional disorder with topological disorder. Detailed studies of the influence of the absence of long-range order on the optical properties of various semiconductors were published e.g. in [75, 76, 77]. Again Urbach-tails appear that reduce E_G, and the band structure itself shows broadened bands. The tails are caused by localized electronic states within the bandgap and not by thermal effects. Furthermore, the structure of the bands was found to be not sufficiently defined [77]. This effect is even increased in melted materials that do not exhibit a bandstructure. These observations are identical with the results that we found in our systems with long-range disorder. Therefore, the latter can be directly

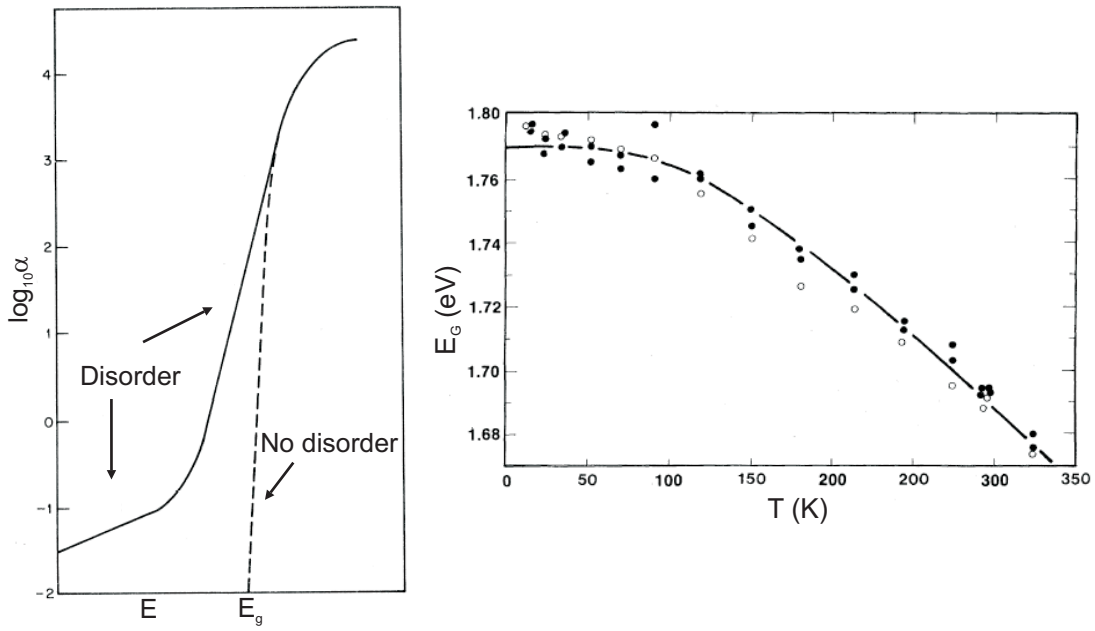

Figure 5.24: Left panel: Form of the absorption edge in ordered and disordered semiconductors. Taken from [78]. Right panel: Bandgap E_G in semiconductors as a function of temperature. Taken from [75].

compared to amorphous materials.

In conclusion, we found that the influence of disorder on the optical properties in metallic photonic crystal slabs can be directly compared to the results published for electronic structures. Both systems show reduced bandgaps and destroyed bandstructures depending on the disorder type.

In the results presented in this chapter we have seen that in systems with long-ranged disorder - i.e., with correlated next-neighbor positions - a large number of quasiguided modes interacts with the particle plasmon. Therefore, an effective Hamiltonian to describe the system completely contains coupling parameters for the interaction of each quasiguided mode with the plasmon and coupling parameters for the interaction between the modes. Such a Hamiltonian was presented in Chapter (2.3). With the energies ϵ_{Pl} and ϵ_i for plasmon and i-th quasiguided mode, respectively, the Hamiltonian reads as

$$H_{eff} = \begin{pmatrix} \epsilon_{Pl} & V_{Pl,1} & V_{Pl,2} & V_{Pl,3} & \cdots \\ V_{1,Pl} & \epsilon_1 & V_{1,2} & V_{1,3} & \cdots \\ V_{2,Pl} & V_{2,1} & \epsilon_2 & V_{2,3} & \cdots \\ \vdots & \vdots & \vdots & \vdots & \ddots \end{pmatrix}. \tag{5.11}$$

$V_{i,Pl}$ and $V_{Pl,i}$ model the coupling of the i-th quasiguided mode with the plasmon, $V_{i,j}$ and $V_{j,i}$ describe the coupling of the quasiguided modes i and j. For further details see Eqn. (2.36). This equation can be used to model the disordered cases. In the frozen-phonon model only a single quasiguided mode is excited. H_{eff} remains as in the the perfect system, except for a modification of $V_{Pl,i}$ and $V_{i,Pl}$ corresponding to a modified V_2. For increasing long-range disorder, further quasiguided modes at energies $\epsilon_j \neq \epsilon_i$ are excited, giving rise to a non-vanishing of the corresponding off-diagonal elements. Just as in the other disorder model, the corresponding off-diagonal elements $V_{Pl,j}$ and $V_{j,Pl}$ have to be modified. In principal, also V_{ij} and V_{ji} have to change. Unfortunately, no theory exist so far to explain this effect.

We can assume that correlation effects in Eqn. (5.11) lead to effects that are similar to the ones presented in literature. Typically, disordered systems consist of N states $\varphi_1 \dots \varphi_N$ which are described in general by a Hamiltonian

$$\begin{aligned} H &= \sum_m \epsilon_m |\varphi_m\rangle\langle\varphi_m| + \sum_{m\neq n} V_{mn} |\varphi_m\rangle\langle\varphi_n| \\ &= \begin{pmatrix} \epsilon_1 & V_{12} & \cdots & V_{1,N} \\ V_{21} & \ddots & \ddots & \vdots \\ \vdots & \ddots & \ddots & V_{N-1,N} \\ V_{N1} & \cdots & V_{N,N-1} & \epsilon_N \end{pmatrix} \end{aligned} \tag{5.12}$$

with V_{ij} as the interaction of the states φ_i and φ_j. The similarity of H to the Hamiltonian in Eqn. (5.11) for the metallic photonic crystal is obvious when assuming $\epsilon_1 = \epsilon_{Pl}$ and $V_{1j} = V_{Pl,j}$ and $V_{j1} = V_{j,Pl}$. Based on the fundamental work by Eugene Wigner [79], a lot of publications deal with systems being described by the Hamiltonian in Eqn. (5.12). In [80] an extended model with correlations between diagonal ϵ_m and off-diagonal elements V_{mn} was presented that is applicable to structurally induced disorder in solids. This model was used to calculate transport in disordered electronic systems. It was found that correlations between site and off-diagonal disorder [see Eqn. (2.41)] can give rise to superdiffusion transport in 1-dim systems, and this transport is furthermore independent of the amount of disorder. This can be explained by the fact that the critical disorder amount W_C [1] for localization in the Anderson-model [51] tends to be infinite in the presence of correlations. This model was extended to random-dimers with two site-energies ϵ_a and ϵ_b with one of the energies set at random for pairs of lattice sites [81].

In [82], Eqn. (5.12) was considered for a tight-binding model with nearest neighbor interaction and $\{\epsilon_i\}$ are correlated random variables. Thus, the off-diagonal Hamiltonian elements V_{ij} vanish except for the case that i and j are nearest neighbors. As already discussed, the energy level spacing function experiences a transition from a Wigner distribution [Eqn. (2.47)] for extended states to a Poisson distribution [Eqn. (2.48)] for localized

[1] All states in the system are localized for disorder amounts W exceeding W_C.

states (see Chapter 2). Further works on 1-dim random potentials as in Eqn. (5.12) revealed a mobility edge in the presence of specific long-range correlations [83].

To summarize we found that an extended Hamiltonian for describing our metallic photonic crystals shows some similarities with Hamiltonians presented in literature. These Hamiltonians are used to model certain disordered systems, where a lot of interesting phenomena like modified localization are found. Therefore, the connection from our disordered system to light localization is obvious. Especially long-range disorder with correlations between the ϵ_i in Eqn. (5.11) could reveal a lot of interesting effects. As a consequence, further studies on our disordered metallic photonic crystal slabs are important.

Chapter 6

Optical switching in metallic photonic crystals

In this chapter we report on a metal-polymer compound material with optical properties that can be reversibly switched all-optically. The key element is a metallic photonic crystal slab with an additional layer of photoaddressable material that provides a large variable birefringence and sharp resonances. Pump-probe experiments show a shift of the photonic crystal resonances that depends on the pump polarization and on the exposure. Comparison of these results with calculations derived from a scattering-matrix theory allows to determine the refractive index changes for different polarization geometries and to model our compound material quantitatively.

6.1 Photoaddressable polymers

Photoaddressable polymers (PAP) have attracted a lot of interest for future optical devices due to their large light-induced birefringence. By modifying the molecular structure, a huge birefringence of up to $\Delta n = 0.5$ was observed [84]. PAP consists of specially designed side-chains that are attached via $(CH_2)_2$ spacers to a polymethacrylate backbone [85]. Two kinds of side chains are connected: chromophoric chains containing azobenzene derivatives and mesogenic chains. The chromophore is a photoactive group and the main element for the observed birefringence. The mesogenic molecules basically stabilize the chromophore configuration [86]. The chemical structure of typically utilized materials are shown in Fig. 6.1. Generally, mesogenic and chromophoric parts are mixed in a relation $x : y = 1 : 1$ [85].

Polymers containing azobenzene moieties have been discovered for their photoinduced optical anisotropy some time ago [87, 88]. These molecules are characterized by two distinct configurations. Besides a stretched *trans*-form they also exist in a folded *cis*-form. The molecules are able to undergo a transition from the *trans*- into the *cis*-isomers and vice versa under light illumination in a so-called *photoisomerization* process [89]. This process was described in detail in [90]. Azobenzene in the stable equilibrium *trans*-

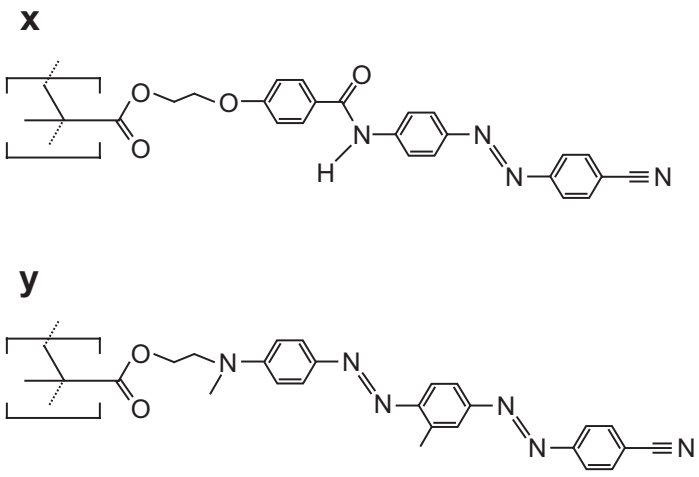

Figure 6.1: Structure of photoaddressable polymers (PAP) [85]. The molecule with concentration x is a mesogen, the molecule with concentration y is a chromophore.

state $S_{0,t}$ can be excited into the state $S_{1,t}$ via photon absorption. The reverse thermal relaxation back to $S_{0,t}$ passes the triplet state $T_{1,t}$. Since the energies of the triplet states $T_{1,t}$ and $T_{1,c}$ of *trans*- and *cis*-form are close by, the probability for a transition $T_{1,t} \rightarrow T_{1,c}$ is very high. Hence, the *trans*-state can undergo a transition to the excited *cis*-state $T_{1,c}$ by absorbing a photon. $T_{1,c}$ relaxes thermally into the *cis*-ground state $S_{0,c}$, a further reverse relaxation into $T_{0,t}$ is possible. This cycle is repeated upon continuous irradiation, initiating the molecule to perform a shivering movement. Figure 6.2 shows both molecular forms of the chromophoric PAP-isomers.

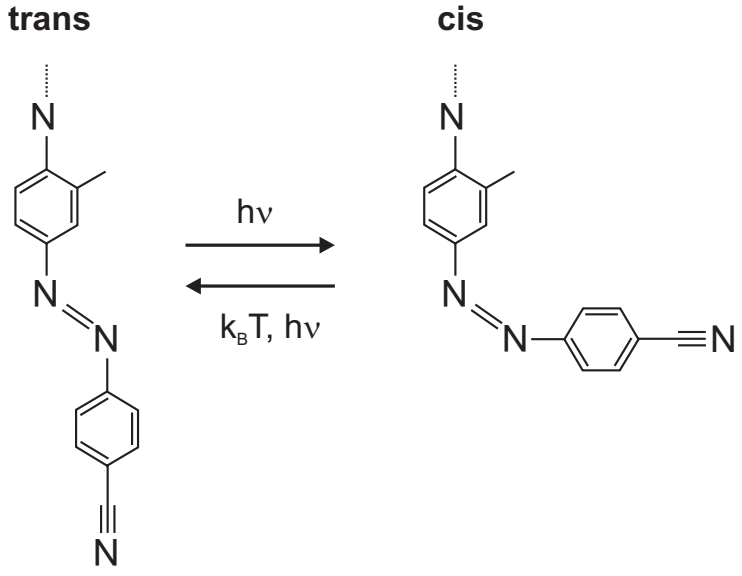

Figure 6.2: Scheme of the photoisomerization cycle of the chromophoric PAP-isomers from the *trans*- into the *cis*-state and vice versa.

It is know that this *trans*-*cis*-photoisomerization can reorient the chromophores [87]. Especially when using linearly polarized light, the long axis of the *trans*-chromophores are oriented perpendicular to the polarization direction of the incident light. A further absorption of light is no longer possible due to the dipole characteristic of the absorption. The molecules remain in this spatially stable orientation, continuous illumination tends to orient all molecules. As a result, the absorption of the incident light is drastically reduced and, because absorption and refractive index are connected via the Kramers-Kronig-relation [43], also the refractive index is influenced. It is decreased in the direction of the polarization ($n_{\parallel}$) and enhanced in the perpendicular direction ($n_{\perp}$), leading to an enhanced birefringence $\Delta n = n_{\perp} - n_{\parallel}$ [84].

To further improve the optically induced birefringence Δn, a modified PAP with additional mesogenic side chains has been developed (see [91] and references therein). Mesogen is a non-absorbing molecule with high form anisotropy. Although it is found typically in a liquid-crystalline phase without optical orientation, quenching processes during the fabrication process may result in an isotropic glassy state. This material is used to stabilize the orientation of the chromophoric azobenzene molecules. It can follow the light induced reorientation of the chromophores due to dipolar or steric interaction, yielding to a Δn of up to 0.13. Further improvements were made by designing a photoactive mesogen also containing azobenzene derivatives [91]. Hence, the mesogen is also able to absorb light which leads both to a stabilized and to an amplified photoisomerization process. Δn of up to 0.5 with a high thermal stability were reported [84, 92]. Improvements in increasing the thermal stability of the molecular orientation by using polymer fractionation have also been published [93].

Due to their remarkable optical properties, PAP was considered as a promising material for future optical devices. Especially the need for smaller and faster devices has increased the effort to implement new materials with improved optical properties. In this work, we want to combine metallic phononic crystal slabs with photoaddressable polymers to show that reconfigurable and reversible all-optical switching of optical properties can be realized in future miniature devices.

6.2 Results

We employed electron-beam lithography to fabricate regular gold nanowire arrays on top of an indium-tin oxide (ITO) waveguide layer that was deposited on a quartz substrate. The wires had a height of 20 nm and a width of 100 nm. Their period was 516 nm, and the ITO-layer had a thickness of 140 nm [Fig. 6.3(a)]. After fabrication of the nanowires, we spin-coated a 100 nm thick layer of PAP material on top of the sample, such that the nanowires were sandwiched between the ITO and the PAP [Fig. 6.3(b)]. The PAP consisted of polymers having bis-azo chromophore side-chains [93, 94]. The PAP was dissolved in cyclopentanone with a concentration of 42 g/l, and the spin-coating

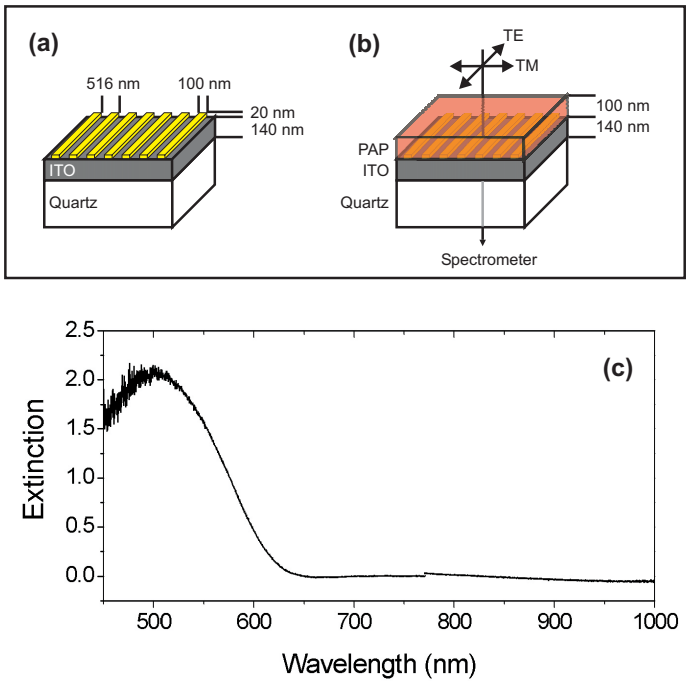

Figure 6.3: Schematic view of the sample without (a) and with PAP-layer (b). The arrows in (b) indicate the electric field direction of the probe beam in TE and TM polarization. (c) Extinction of PAP. The small discontinuity at 775 nm is caused by a change of the spectrometer grating.

was performed at 2000 rpm. Figure 6.3(c) shows the optical absorption of the material, revealing a strong absorption peak around 500 nm.

The optical properties of the sample were determined with a pump-probe experiment [Fig. 6.4(a)]. The beam of a frequency-doubled Nd:YAG laser running at 532 nm was used to trigger the photoizomerization process, leading to a reorientation of the azobenzene molecules and thus to a photoinduced birefringence Δn. Since this can be considered as a "pumping" of the molecules towards a specific orientation, we will refer to this beam in the following as the pump beam. In order to achieve a homogeneous illumination we increased the diameter of the beam to about 1 cm^2 by using a defocusing lens with a focal length of 35 mm at a distance of 25 cm from the sample surface. The total pump intensity at the sample was about 30 mW/cm^2. The pumping was performed in vertical and horizontal polarization with the electrical field being parallel or normal to the nanowires, respectively. The angle of the pump beam with respect to the optical axis was about 50°, see Fig. 6.4(a). A white-light transmission setup was used to probe the extinction of the sample. The linearly polarized white-light beam from a halogen lamp was focused with a microscope objective on the sample, and the transmitted light was measured with a spectrometer. A red-glass filter RG 610 (Schott) ensured that the probe beam was not absorbed and could not modify the PAP. In order to reduce the aperture angle to below 0.2°, we used a pinhole with 600 μm diameter in front of the objective and

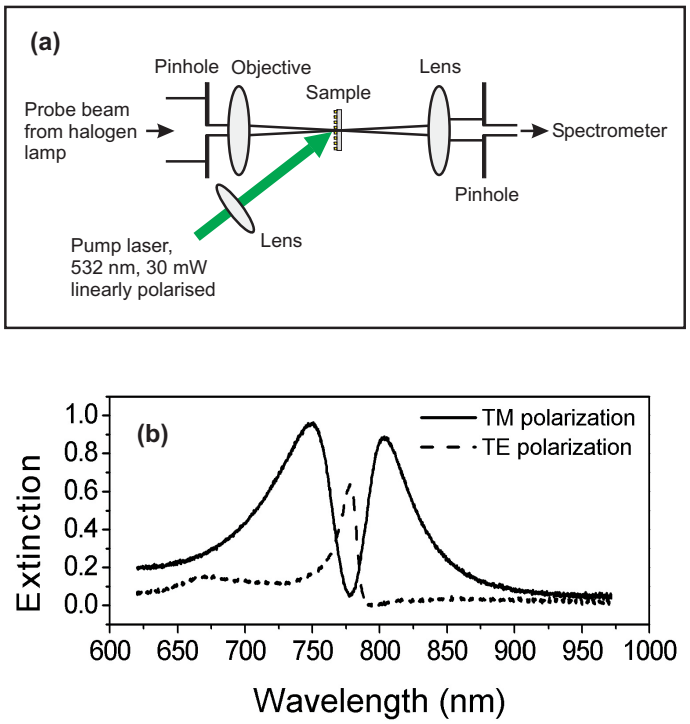

Figure 6.4: (a) Pump-probe setup to determine the optical properties of the sample. The extinction of the unexposed sample with PAP-layer is shown in (b); TM and TE polarization of the probe light are represented by a solid and a dashed line, respectively.

one with 100 μm diameter after the sample. We probed either with the electric field being parallel to the nanowires (TE polarization) or normal to the nanowires (TM polarization).

The extinction spectra of the unexposed sample are shown in Fig. 6.4(b). As shown before, the sample is characterized in TE polarization by the sharp extinction resonance of the quasiguided mode. In TM polarization the coupled system of quasiguided mode and wire plasmon can be observed in the extinction. It should be emphasized that the additional PAP-layer on the sample has no negative influence on the extinction resonances. The resonances are shifted slightly along the wavelength axis, whereas the resonances' form is not affected. Since the energies of these resonances depend crucially on the dielectric constants of the surrounding materials, optical modification of the PAP-layer and hence changing its refractive index will have a strong influence on the spectral positions of the resonances. In the following we will show that this method can be used to reversibly optically switch the optical properties of such metallic photonic crystal slabs. It should be noted that the polaritonic resonances lie outside the absorption band of PAP. However, it was shown that the refractive index in this spectral region between 700 and 850 nm can be influenced by optically-induced dichroism in the blue-green spectral region due to the Kramers-Kronig relation [92].

Extinction spectra for various polarization geometries are plotted in Fig. 6.5. The insets in the figures indicate the polarizations of pump and probe beam with respect

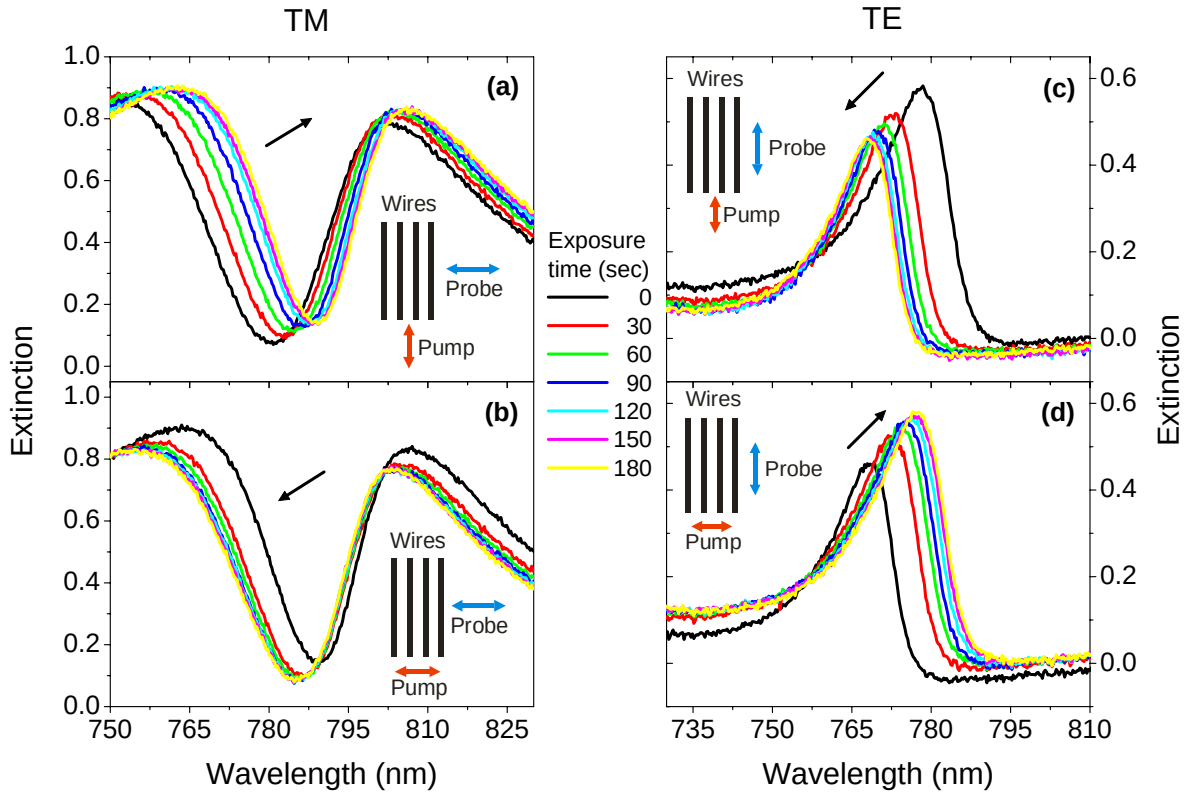

Figure 6.5: Extinction spectra of the sample when pumped with a laser beam at 532 nm and an intensity of about 30 mW/cm^2 for different exposure times. (a) and (b) for TM probe polarization, (c) and (d) for TE probe polarization. The pump beam was polarized vertically [(a), (c)] and horizontally [(b), (d)], respectively. The arrows indicate the shift of the spectral features when pumping the sample for increasing time in a certain polarization geometry.

to the nanowires, which we assume to be vertical. A vertical pump polarization shifts the resonances in TM polarization to higher wavelengths, whereas a horizontal pump polarization has the contrary effect. A similar behavior is observed in TE polarization, where vertical and horizontal pump polarization shift the resonance to lower and higher wavelengths, respectively, which is converse to the TM polarization results. This effect can be understand intuitively: Pumping changes the refractive index of PAP differently in the directions perpendicular ($n_\perp$) and parallel ($n_\parallel$) to the pump polarization [85, 92]. For a fixed probe polarization (TE or TM), the relevant probed refractive index of the material is either $n_\perp$ or $n_\parallel$. Since the refractive index is directly related to a modified propagation vector k_x of the waveguide mode, the dispersion relation leads to a shift of the resonance peak in the spectrum towards shorter and longer wavelengths, depending on whether the relevant refractive index is increased or decreased. These results prove that we are able to influence and switch the optical properties of our metallic photonic crystal by exposing the PAP-layer to pump light.

To further study the use of our structures in possible applications, the time dependen-

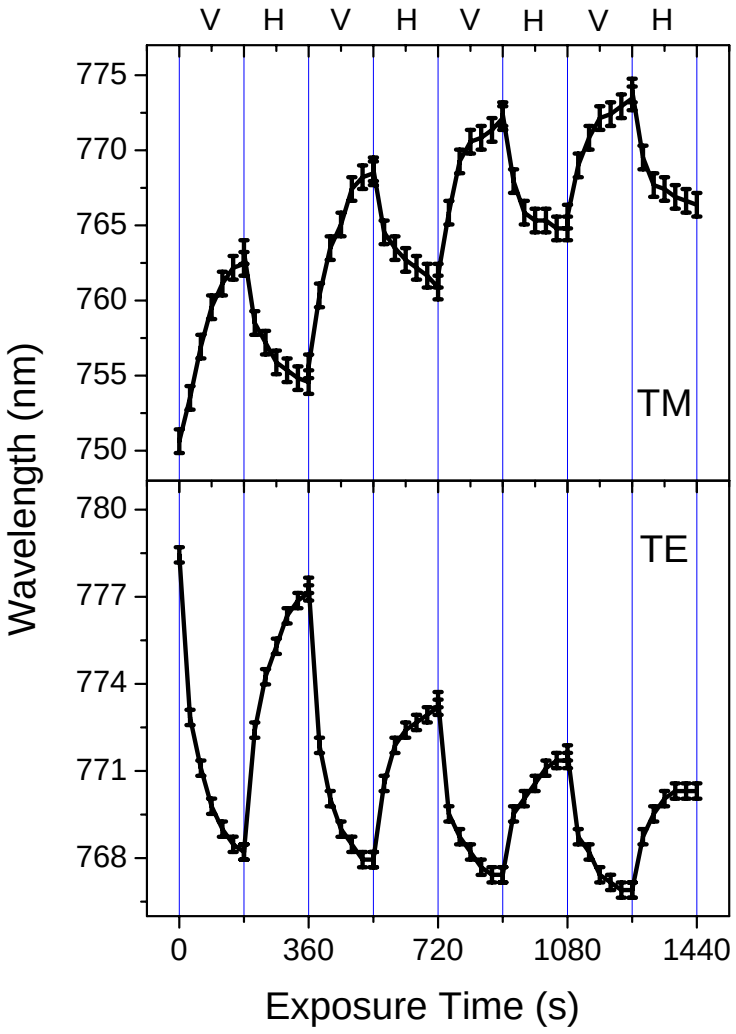

Figure 6.6: Spectral position of the low-wavelength resonance peak in TM probe polarization (upper panel) and of the resonance in TE probe polarization (lower panel) for increasing exposure times and different pump polarizations (H: horizontal, V: vertical).

cies of the shift of the resonances are plotted in Fig. 6.6. We plot the wavelength of the resonance peak in TE polarization for increasing exposure times and for different pump polarizations. The same is done for the extinction maximum at lower wavelengths in TM polarization. The effect of shifting the resonances is clearly visible and reproducible upon repetition of the experiment. TE and TM polarization show opposite behavior for exposure times on the order of a few ten seconds and converse pump polarizations. However, for a given pump polarization, the shift of the resonances becomes smaller for increasing pumping times and reaches a saturation level. We account a nearly complete orientation of the PAP-molecules to be responsible for this effect.

Furthermore, a difference of the saturation levels after several pump processes can be observed. This bleaching effect is assumed to be caused by orientation of the molecules in the direction perpendicular to the film. In this case, the molecules lose their influence on the refractive index [85]. In order to increase the repeatability of the switching properties, using a different, more stable PAP instead of a highly sensitive PAP with a large refractive index change and high birefringence, as we did, would be advantageous. Y. Sabi *et al.* proposed two methods to overcome this problem [85]. One possibility is to modify the shape of the side-chain molecules. This can be achieved by replacing the long-shaped side-chains by ones with a 3-dim polarization ellipsoid. As a result, optical excitation can take place from all directions, especially from the direction perpendicular to the molecule's long axis. The second way to get rid of the bleaching effect is to reduce the interaction between adjacent side-chains. Therefore, the ground state dipole moments and the attractive intermolecular forces have to be reduced. It can be realized by changing the substituents of the azobenzenes.

To get a better understanding of the refractive index changes in the exposed material and to theoretically and quantitatively model the optical properties of our compound system, we applied a scattering matrix theory [30] to reproduce the experimental results. Here, the electromagnetic field is decomposed into planar waves with momenta given by the angle of the incoming light field and the reciprocal lattice vector. The sole parameters in the simulations are the geometric sizes and the dielectric constants of quartz, ITO, and gold (for details see [9] and references therein). To include the exposure of the PAP, we performed the calculations, assuming the refractive indices n_{PAP} of the PAP layer to be independent of the wavelength in the direction of the probe beam polarization, and completely neglecting its birefringence. From comparing experimental and theoretical spectra and looking for agreements, we determined n_{PAP} for different pump/probe geometries and exposure times. Discrepancies are caused by neglecting the spectral dispersion of the refractive index of PAP in the simulations which oversimplifies our situation [86, 95].

Typical theoretical results are plotted in Fig. 6.7, showing the regions around the characteristic spectral features both in TM and TE polarization. These spectra correspond to the experimental data shown in Fig. 6.5(a) and (c). Comparing the results reveals a good agreement between experiment and theory. Imperfections of the fabricated sample causes the absolute extinction in the simulations to be larger than in the measurements. According to the simulations, exposure times of up to 180 s can be interpreted by a change of n_{PAP} from 1.96 to 1.83 in TE polarization and from 1.77 to 1.86 in TM polarization. This supports the fact that a varying refractive index of PAP is the responsible mechanism for shifting the resonances. The slightly different refractive indices in the two polarization directions in our simulations could be caused by the fact that we spin-coated new PAP onto the sample between TE and TM measurements, resulting probably in a slightly modified PAP thickness. This would lead to a different effective refractive index

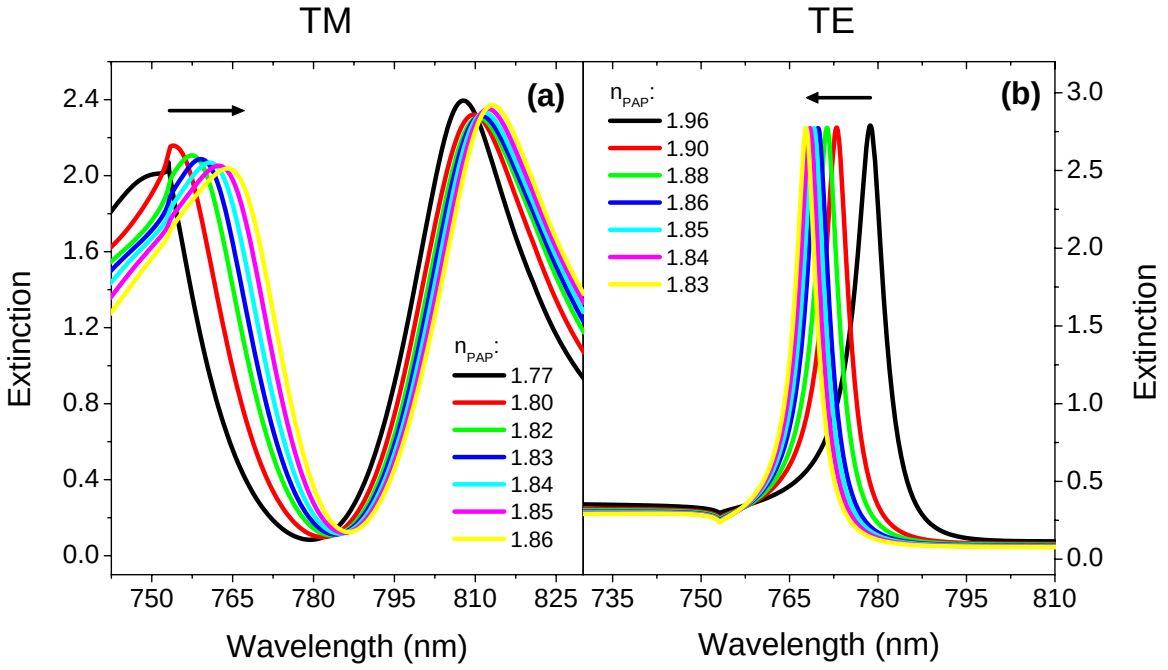

Figure 6.7: Theoretical simulations both for (a) TM and (b) TE polarization. The spectra were modeled for different refractive indices n_{PAP} of PAP. They correspond to the experimental spectra in figures 6.5(a) and (c). The arrows indicate the shift of the resonances.

in our simulations. Taking the data from Figs. 6.6 and 6.7 allows to determine n_{PAP} for a sample that is exposed as described above. Figure 6.8 shows n_{PAP} both for TE and TM polarization. Similar to the resonance positions in Fig. 6.5, n_{PAP} varies depending on exposure time and pump light polarization. In spite of the simplified model, the range of n_{PAP} agrees well with results reported elsewhere [86, 95].

It would be quite easy to build a reconfigurable optical switch using these effects. A miniaturized frequency-doubled Nd:YAG laser (pumped with a diode at 808 nm) with a laser wavelength of 532 nm could serve as pump source and provide the necessary power densities. A simple laser diode at, e.g., 780 nm is used as the source for the probe beam. The sample is exposed to TE polarized light (electric field along the wires), and the optical properties are probed in the orthogonal polarization direction. After illumination for about two minutes, the sample switches the extinction value of the 780 nm probe laser from below 0.2 to above 0.8. Changing the polarization of the pump laser by 90 degrees reverses the effect again. Such a setup has two advantages compared to other realizations. First, the spectral resonances can be shifted within a broad spectral range by simply changing the sample geometry [8, 9, 35]. Second, a very steep resonance can be realized [96] ensuring a high sensitivity to the exposure process.

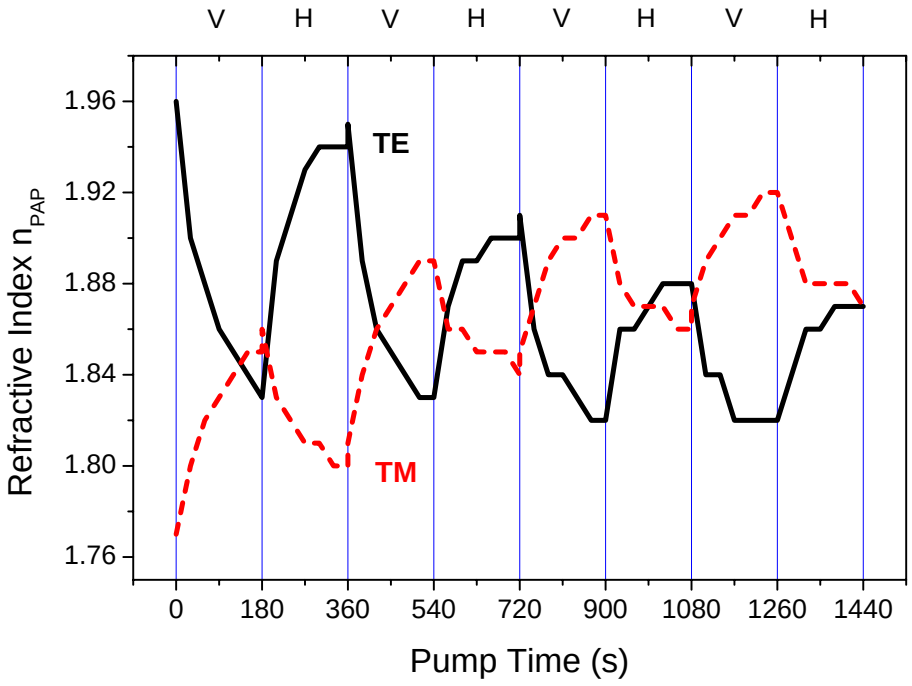

Figure 6.8: Time dependence of the deduced refractive index n_{PAP} of PAP for TM and TE polarization and for different pump polarizations (H: horizontal, V: vertical).

In conclusion, we have shown that the optical properties of a compound material consisting of a metallic photonic crystal slab and an additional layer of a photoaddressable polymer can be reversibly changed by illuminating it within its absorption band with polarized light. The resonances of the system change depending on the polarizations of pump and probe beams and depending on the exposure time. Our experimental results show that such a system can be used as a simple, small, and all-optical reversible switch. To further improve the switching behavior, a modified PAP material as proposed in [85, 91] can be used, warranting a reproducibility of the switching behavior even after many cycles.

Chapter 7

A photonic crystal sensor for hydrogen gas

Recently there has been a lot of effort to investigate new approaches for low-cost and sensitive sensors for hydrogen gas. Such sensors can be used in many hydrogen applications, for example in hydrogen powered cars or fuel cell technology to detect leaks or determine hydrogen levels. One approach is to use the gasochromic coloration of tungsten oxide (WO_3) or certain Lanthanide hydrides, where the reaction with hydrogen gas causes a change in the optical properties of the material. In these systems, the hydrogen gas is dissociated into single H atoms that react with the transition metal oxides according to the double injection / extraction model [97]. So far, this effect was used to measure a change in the reflectivity of the material [98, 99] or a shift in the surface plasmon resonance [100]. In this work, we want to present a new approach for a hydrogen sensor that is based on the gasochromic mechanism in metallic photonic crystal slabs using a WO_3-layer.

7.1 Coloration of WO_3

Tungsten oxide WO_3 is a material that is widely used in technical applications for its ability to change its color. This can be achieved with several techniques:

- Electrochromism
- Photochromism
- Chemochromism / Gasochromism

The basic coloration mechanism is identical for all three techniques, namely the incorporation of electrons and positively charged ions into the material to create color centers. The techniques differ only in the way of providing the charge carriers, therefore, the basic principle of coloration of WO_3 is valid for all of them. Starting with electrochromism, these techniques will be discussed now in detail.

7.1.1 Electrochromism

Electrochromism is described in detail in [101]. It was reported that the injection of ions such as H^+ or Li^+ causes the color of thin amorphous tungsten oxide films ($a - WO_3$) to change from transparent to dark blue. Raman spectra of $a{-}WO_3$ revealed that the valency of the tungsten atoms changes during the coloration process, resulting in the formation of color centers and changed optical properties of the material. As-deposited films contain mainly W^{6+} and W^{4+} states, the chemical formula of the material is $W^{6+}_{1-y}W^{4+}_{y}O_{3-y}$ (y: oxygen deficiency). Positively charged ions leave the W^{4+} states unchanged but reduce some of the W^{6+} states to W^{5+}. The ions are injected by inserting $a - WO_{3-y}$ into an electrolytical solution (e.g. H_2SO_4) and using a platinum wire as counter electrode. This process is described by the so-called *double injection/extraction model*:

$$xM^+ + xe^- + a - WO_{3-y} \longleftrightarrow a - M_xWO_{3-y}, \tag{7.1}$$

where $M = H, Li$, etc. The W^{5+} states then have the possibility to trap and localize electrons that are provided by the solution. Once the electrons are localized, they can polarize the surrounding lattice sites to form polarons. Incident light is then absorbed by transitions of the polarons between W^{6+} and W^{5+}, and W^{5+} and W^{4+} states. For two tungsten ions $W_{(1)}$, $W_{(2)}$ and light at energy $h\nu$ this process reads as:

$$h\nu + W^{4+}_{(1)} + W^{5+}_{(2)} \longrightarrow W^{5+}_{(1)} + W^{4+}_{(2)} \tag{7.2}$$

and

$$h\nu + W^{5+}_{(1)} + W^{6+}_{(2)} \longrightarrow W^{6+}_{(1)} + W^{5+}_{(2)}. \tag{7.3}$$

It was reported that increasing the number y of oxygen deficiencies increases the coloration efficiency in electrochromism [102]. No coloration is observed in nearly stoichiometric films. The number of W^{5+} states, generated by insertion of positively charged ions, is strongly related to the oxygen deficiency.

The consequences of this coloration process are presented in Fig. 7.1, where the refractive index n and the absorption coefficient κ are plotted as a function of wavelength and for different injected charges (data taken from [103]).

The injection of charges causes refractive index n and absorption coefficient κ to change in the visible spectral range. For the case of no injected charge, the refractive index n is monotonically decreasing from n = 2.12 at 400 nm to n = 1.88 at 1400 nm. Incorporated charges change the shape of the n-curve, it has a minimum around 750 nm. The strongest deviations from the case of no injected charges are found in the range from 700 nm to 800 nm. While WO_3 has no absorption in the range above 400 nm, κ increases if injected charges are present and shows a maximum at 1000 nm. These deviations increase for increasing charge injection. This has to be taken into account when making use of the optical properties of WO_3 in sensor applications. In the visible spectral range, we always observe a change of both refractive index and absorption at the same time.

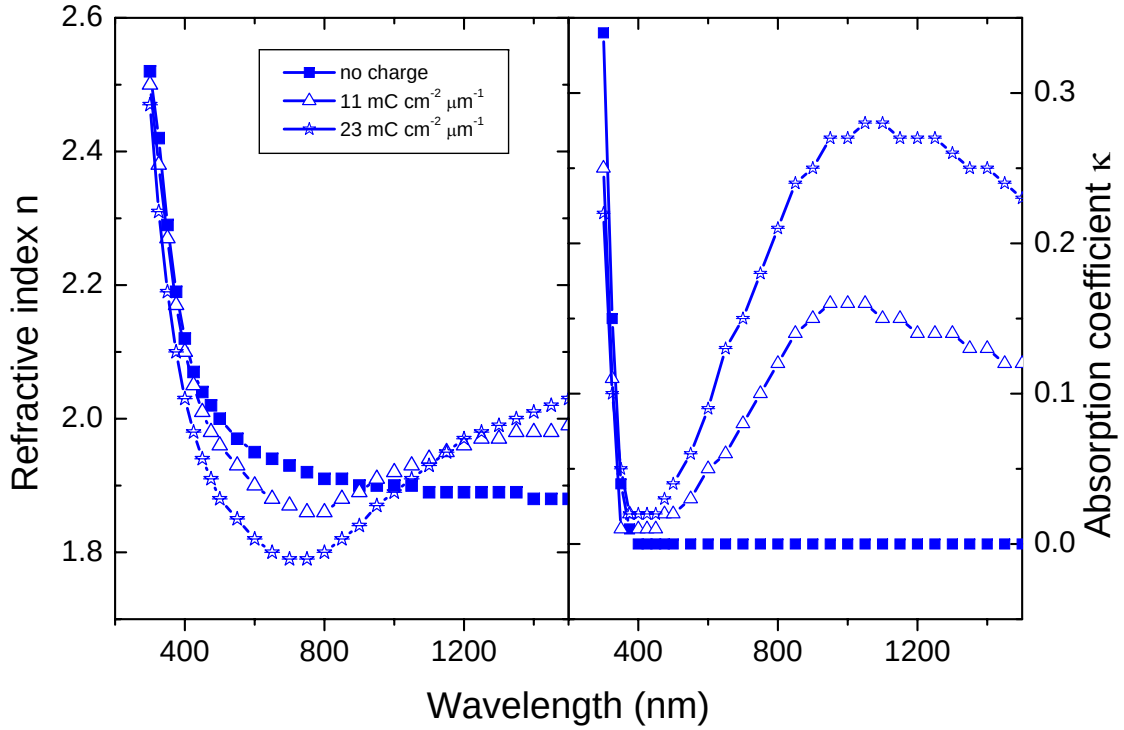

Figure 7.1: Refractive index n and absorption coefficient κ of WO_3 as a function of wavelength and injected charge. Data taken from [103].

As mentioned above, the model for the coloration process of WO_3 holds for all techniques that are described in this work [97, 104]. We can thus take the results, shown in Fig. 7.1, with slight modifications to determine the optical properties of WO_3 in photochromic and gasochromic experiments [100].

7.1.2 Photochromism

Another method to change the color of WO_3 is photochromism, where an absorption band is formed by irradiating thin films of WO_3 with light [105]. A model to explain this process was proposed in [104]. Here, pairs of electrons e^- and holes h^+ are optically excited in the WO_3, which together with the presence of water changes the optical properties of the material. The holes can weaken the H–O bonds of water, which leads to the creation of protons H^+ and metastable oxygen radicals O. The light-induced decomposition of H_2O is called *photoelectrolysis* and can be described by

$$H_2O + 2h^+ \longleftrightarrow O + 2H^+. \tag{7.4}$$

To prevent the starting of the back-reaction, it is necessary to immediately separate protons and oxygen radicals from each other. The radicals have the possibility either to occupy oxygen vacancies in the WO_3 or to form oxygen molecules and escape into the surrounding. The protons together with the optically excited electrons can then form

HWO_3 according to the double injection model. Due to the large band gap of WO_3 of 3.25 eV [105], the photochromism usually requires excitation in the ultraviolet range [104]. However, it was shown that the process can also take place with visible light by adding a thin layer of CdS [106].

7.1.3 Chemochromism / Gasochromism

The chemochromic or gasochromic coloration of a $-\ WO_3$ follows the double injection / extraction model. Here, H^+-ions and electrons are injected by adding hydrogen gas to WO_3 [97]. To further accelerate the reaction, the WO_3-layer has an additional thin layer of a catalyst on top (e.g. palladium Pd). It allows the reaction to take place within a few seconds [100]. The molecular hydrogen gas in the surrounding is split into atomic hydrogen when getting into contact with the catalyst. The atomic hydrogen then has the possibility to diffuse through the catalyst to the WO_3-layer. Coming to the interface, it is split again, this time into H^+ and an electron. These two can then be incorporated into WO_3 and change its optical properties, as described in the double injection/extraction model. Figure 7.2 shows the steps of this process schematically.

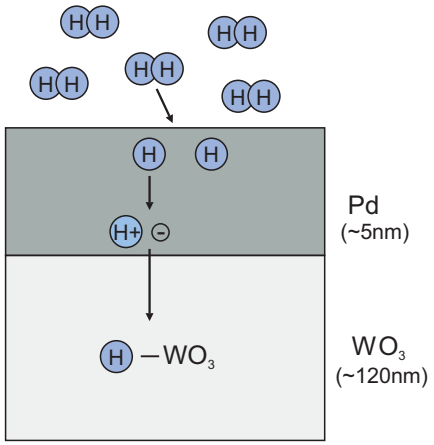

Figure 7.2: Gasochromic coloration of WO_3. Molecular hydrogen is split into atomic hydrogen at the Pd-catalyst, and split again at the interface to the WO_3-layer into H^+ and an electron. These are then incorporated into the WO_3 to form HWO_3.

Since this process is not static, it can be reversed by simply flushing the WO_3 with air, which then removes the hydrogen. The effect on n and κ can be determined by using the data from [103], because we can interpret the gasochromic coloration as electrochromism with H^+ (see also Fig. 7.1).

In conclusion, three different mechanisms can change the optical properties of tungsten oxide (WO_3). The effects can be explained by the so-called double injection/extraction model. In the following, we want to use the gasochromic coloration in combination with a metallic photonic crystal slab to build a sensor for hydrogen gas.

7.2 Basic idea of the sensor

A possible sensor realization has to fulfill certain specifications. The U.S. Department of Energy (DOE) Hydrogen Program has proposed the following performance targets for safety sensors [107]:

- Measurement range: $0.1 \ldots 10\%$ H_2 in air
- Operating temperature: $-30 \ldots 80°C$
- Response time: < 1sec
- Accuracy: 5%
- Gas environment: ambient air, $10 \ldots 98\%$ RH range (humidity)
- Lifetime: 5 years
- Selectivity from interference gases, such as hydrocarbons, is needed.

The idea behind our sensor approach is the following. We want to fabricate a metallic photonic crystal slab as described in the previous chapters. But here, the waveguide material consists of a WO_3-layer. If the hydrogen gas concentration in the surrounding is then raised (lowered), hydrogen gas is incorporated into (removed from) the WO_3 layer, which changes its refractive index and absorption coefficient. This process influences the quasiguided mode whose resonance wavelength is shifted. The shift directly depends on the change of n, see Eqn. (2.26) with $\epsilon_M = n^2$. Furthermore, the resonance wavelength of the plasmon depends on n, too [17]. Hence the optical properties of the whole polariton should be modified if the hydrogen concentration in the surrounding of the sample varies. Finding a relation between the hydrogen concentration and the change of the optical properties would then allow to use the structure as hydrogen sensor.

Since a full extinction spectrum contains too much information to be used in a simple sensor, we propose to use a laser diode as light source, whose wavelength is chosen to be situated on the slope of the quasiguided mode (see Fig. 7.3). A photodiode serves as detector which measures the transmitted light of the laser diode. A beamsplitter between laser diode and sample creates a reference beam to pass an unstructured part of the sample. A change of the hydrogen concentration would shift the waveguide mode / change the extinction of the sample, resulting in a modified extinction. The signal of the photodiode would change according to the hydrogen concentration.

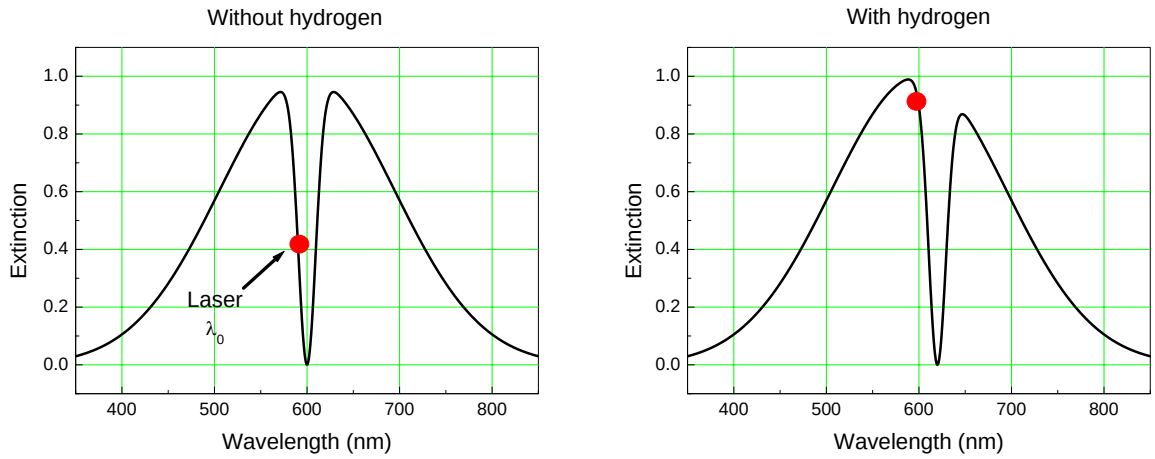

Figure 7.3: Sketch of the modified polariton resonance when the hydrogen concentration is changed. As a result, the measured extinction at the laser wavelength λ_0 changes.

Such a setup has the advantage of being very compact. The typical samples have a size of smaller than 1x1 mm^2. Also laser diode and photodiode are compact which therefore holds for the whole sensor (see Fig. 7.4). As reported, the process of incorporating hydrogen into WO_3 is quite fast and takes place on a time scale of typically a few seconds [100]. Thus, the detection of extinction variations should be possible on this short timescale, too. As will be discussed later on, the sensor is in principal able to detect changes of the hydrogen concentration in the sub-‰-range. Also changes of higher concentrations can be determined, so this new approach can already fulfill most of the requirements mentioned above.

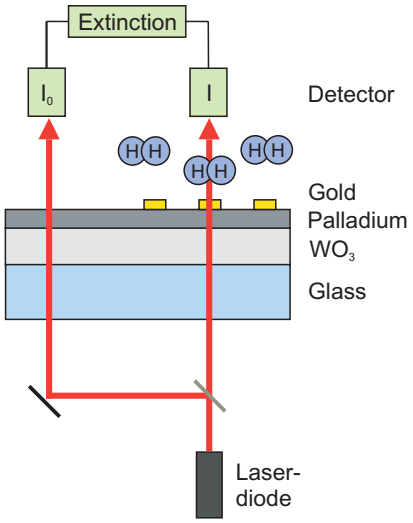

Figure 7.4: Setup of the hydrogen sensor. See text for details.

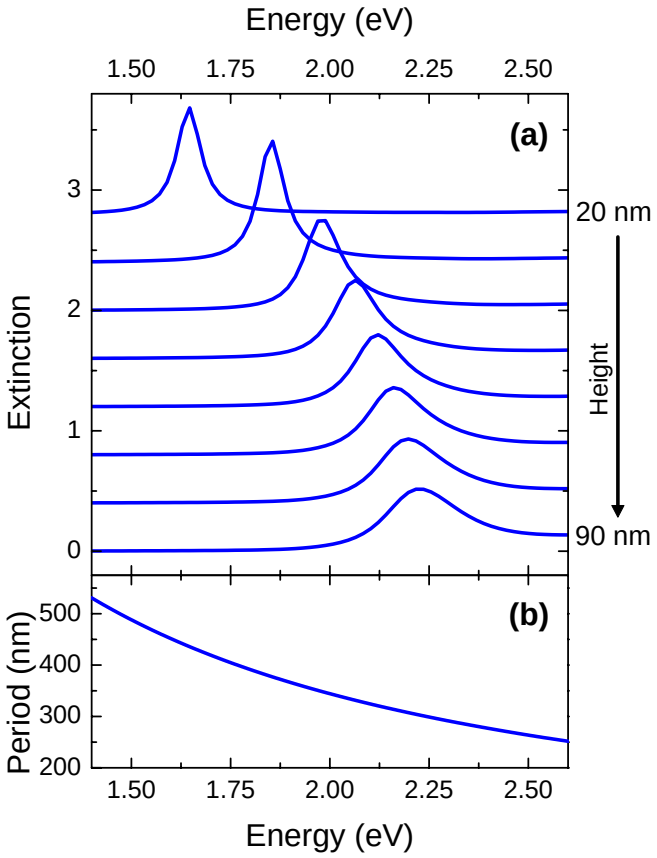

Figure 7.5: (a) Particle plasmon resonance calculated with the electrostatic approximation for gold dots on a WO_3-layer. The particles had a diameter of 100 nm and varying heights. The individual spectra are shifted upwards for clarity. (b) Dispersion of the quasiguided mode excited in a 120 nm thick WO_3-layer.

Figure 7.5(a) shows the calculated particle plasmon resonance for gold dots on a WO_3-layer. The dots had a diameter of 100 nm and varying heights. It can be seen that the plasmon resonance can be tuned within the visible spectral range by changing the particle height from 20 to 90 nm. For a thickness of the WO_3-layer of 120 nm the dispersion in Fig. 7.5(b) indicates that periods of the gold nanostructures of 200 to 500 nm are necessary to cover the same visible spectral region. These parameters are realizable with modern fabrication methods. Therefore, it is possible to combine the optical properties of particle plasmon and quasiguided mode to build a hydrogen sensor based on metallic photonic crystal slabs.

7.3 Setup for gas measurements

In the following, we will concentrate on the optical properties of the metallic photonic crystal slab structure, because it is necessary to understand their basic properties for a possible sensor application. To be able to perform the measurements of the optical properties of the samples in different gas surroundings, the setup that was used so far has to be modified. Two aspects have to be considered. On the one hand, a method is needed to vary the gas concentration as desired. On the other hand, a special chamber to surround the sample with the gas is required. Figure 7.6 presents a sketch of the setup.

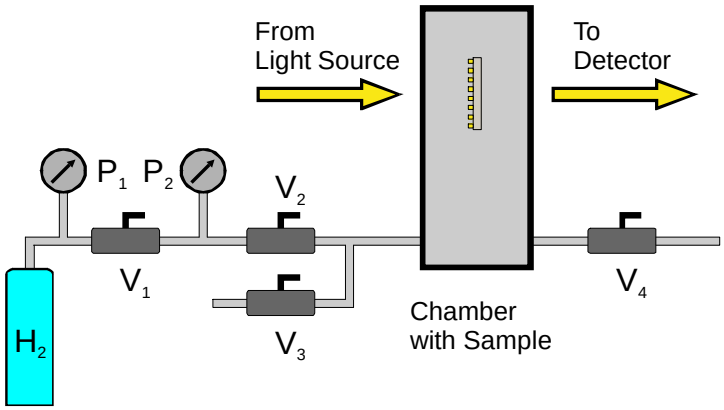

Figure 7.6: Setup for measuring the optical properties of samples in different gas surroundings. See text for details.

The samples are inserted into a chamber, whose interior is connected to the gas system. The chamber consists of a metallic housing with windows on two opposite sides enabling transmission measurements. The samples are fixed in a holder that can be removed by lifting the top of the chamber. The windows are covered on both sides with an anti-reflection coating for the visible spectral range. These coatings avoid multiple reflections within the windows that produce undesired Fabry-Perot fringes in the signals. The measurement of the optical properties of the samples is done by integrating this chamber in the standard linear transmission setup with a halogen lamp as light source and a spectrometer as detector (see Fig. 3.3). The chamber is placed between microscope objective and recollimation lens. The hydrogen gas is contained in 12 l bottles from Messer Griesheim. The bottles are equipped with a valve V1 that allows to reduce the pressure of the gas from 12 bar to about 2 bar. Two measuring instruments P1 and P2 around V1 give the possibility to measure the gas pressure in the bottle and in the chamber system. V1 together with V2 is used to vary the gas concentration as desired (see below). Valve V2 opens the chamber

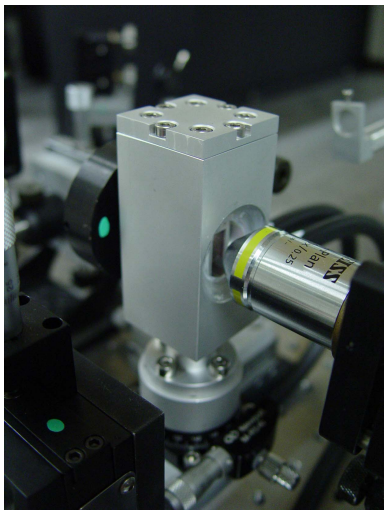

Figure 7.7: Photo of the WO_3-setup. It shows the chamber containing the WO_3-samples in different hydrogen atmospheres. It is included in the standard linear transmission setup (see Fig. 3.3).

to the gas, V3 and V4 are needed to flood the chamber with fresh air and to remove the hydrogen gas. The gas is transported between the elements through special gas tubes. A photo of the gas chamber is shown in Fig. 7.7.

7.4 Determining the hydrogen concentration

To be able to exactly control the hydrogen concentration with the modified setup as described above, we make use of the ideal gas equation (see e.g. [108]). If we assume the chamber to contain only air and V2, V3 and V4 to be closed, the gas equation can be written as

$$p_0 V_0 = \nu_0 R T_0. \tag{7.5}$$

Here, R = 8.31 $J\,mol^{-1}K^{-1}$ denotes the gas constant, p_0 is the air pressure, V_0 the volume of the chamber (the volume of the tubes connecting the chamber with the valves is neglected), T_0 the room temperature and ν_0 the mass of air in the chamber in units mol. Opening V1 and V2 causes hydrogen gas with partial pressure p_{H_2} to flow into the chamber. Therefore we have a mixture of hydrogen and air inside the chamber. With the new pressure $p = p_0 + p_{H_2}$ (measured at P2) and the amount of substance $\nu = \nu_0 + \nu_{H_2}$ inside the chamber, the gas equation reads as

$$(p_0 + p_{H_2})V_0 = (\nu_0 + \nu_{H_2})RT_0. \tag{7.6}$$

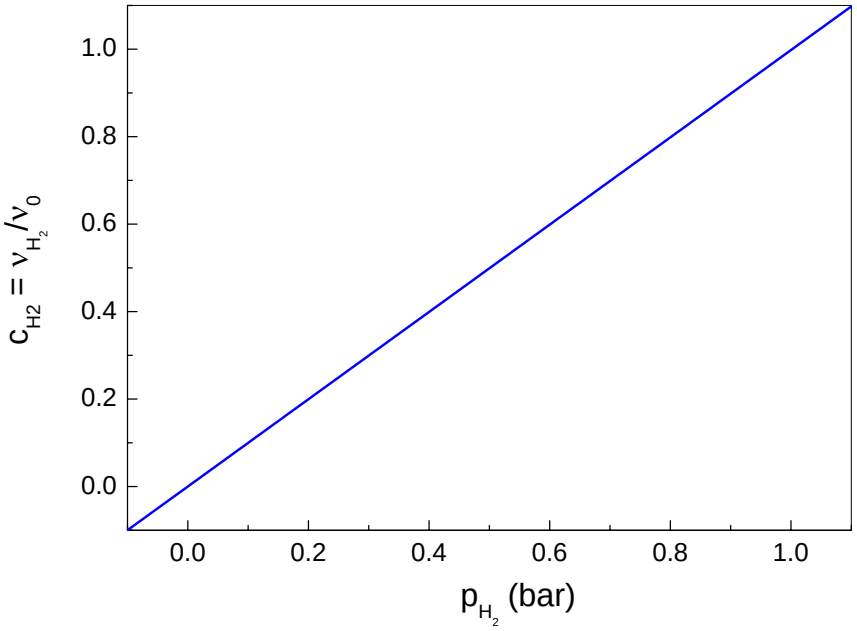

Figure 7.8: Hydrogen concentration c_{H_2} in the sample chamber as a function of the hydrogen partial pressure p_{H_2} at $p_0 = 1002$ mbar.

From this equation we derive the following expression for ν_{H_2}:

$$\nu_{H_2} = \frac{(p_0 + p_{H_2})V_0}{RT_0} - \nu_0. \tag{7.7}$$

If we define the concentration of the hydrogen as $c_{H_2} := \nu_{H_2}/\nu_0$, we get the following expression:

$$c_{H_2} = \frac{\nu_{H_2}}{\nu_0} = \frac{p_{H_2}}{p_0}. \tag{7.8}$$

This means that the concentration of hydrogen gas inside the chamber can be varied by simply changing the partial pressure p_{H_2} of the hydrogen gas, which is measured at P2. Figure 7.8 shows c_{H_2} as a function of p_{H_2} for an ambient air pressure of $p_0 = 1002$ mbar. It is possible to vary the hydrogen concentration in the range from 0 to 1 ($0 \ldots 100\%$) by increasing the hydrogen partial pressure from 0 bar to 1 bar.

A typical measurement is done as follows. After inserting the sample into the chamber, properly closing it and aligning the sample into the focal point of the microscope objective, all remaining hydrogen should be removed out off the chamber. This is done by opening V3 and V4 for a long enough time (at least 1 min). Then V3 and V4 are closed again. V1 and V2 are opened to let hydrogen flow into the chamber. The pressure inside is measured with P2, from which the hydrogen concentration is determined by using Eqn. (7.8). If p_{H_2} (c_{H_2}) has reached the desired value, the measurement of the optical properties of the sample in a certain hydrogen atmosphere can be performed. To be sure to get rid of all incorporated hydrogen after the measurement, the valves V3 and V4 are opened again.

7.5 Experimental results

We prepared 120 nm thick WO_3 waveguide layers on a glass substrate. A 2 nm thick palladium (Pd) layer covering the WO_3 acted as a catalyst to facilitate the reaction with hydrogen gas. Electron-beam lithography was used to fabricate 1-dim gold gratings on top of the Pd. The gold wires had a width of 100 nm, a height of 20 nm, and the period was 450 nm [Fig. 7.9(a)]. According to the calculation presented in Fig. 7.5 the resonances are located in the visible spectral range. This assumption is confirmed by the extinction of the sample that is plotted in Fig. 7.9(b) for $p_{H_2} = 0$. The typical resonance of the TE quasiguided mode and the polariton resonances in TM polarization appear. To examine the influence of various hydrogen concentrations on the optical properties of the sample, we focus on the spectral features that are marked by arrows. These features are the sharp quasiguided mode in TE polarization and the minimum that separates the TM polariton branches.

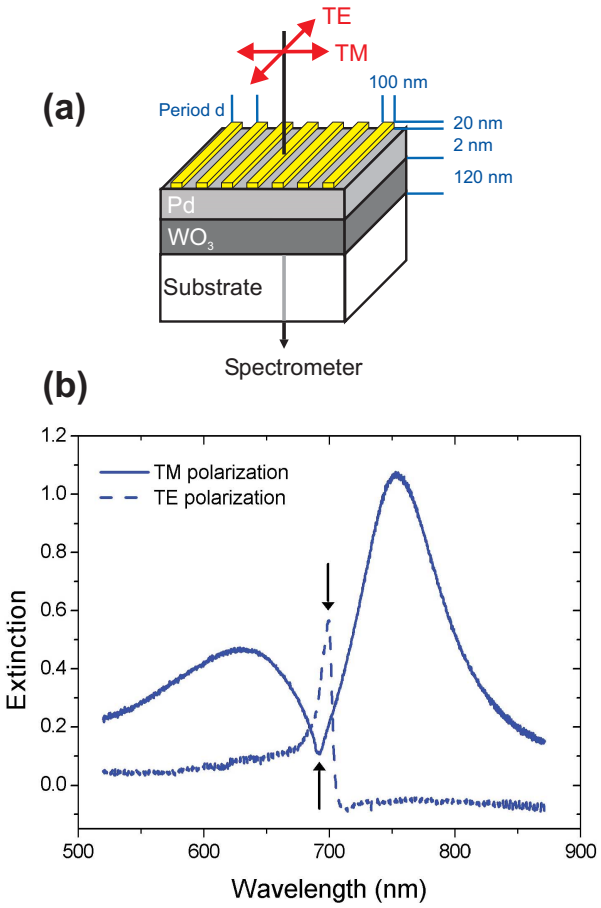

Figure 7.9: (a) Design of the metallic photonic crystal slab using WO_3 as waveguide layer material. The arrows indicate TE and TM polarization, respectively. (b) Extinction of the sample. The arrows mark the spectral features that are examined in the analysis.

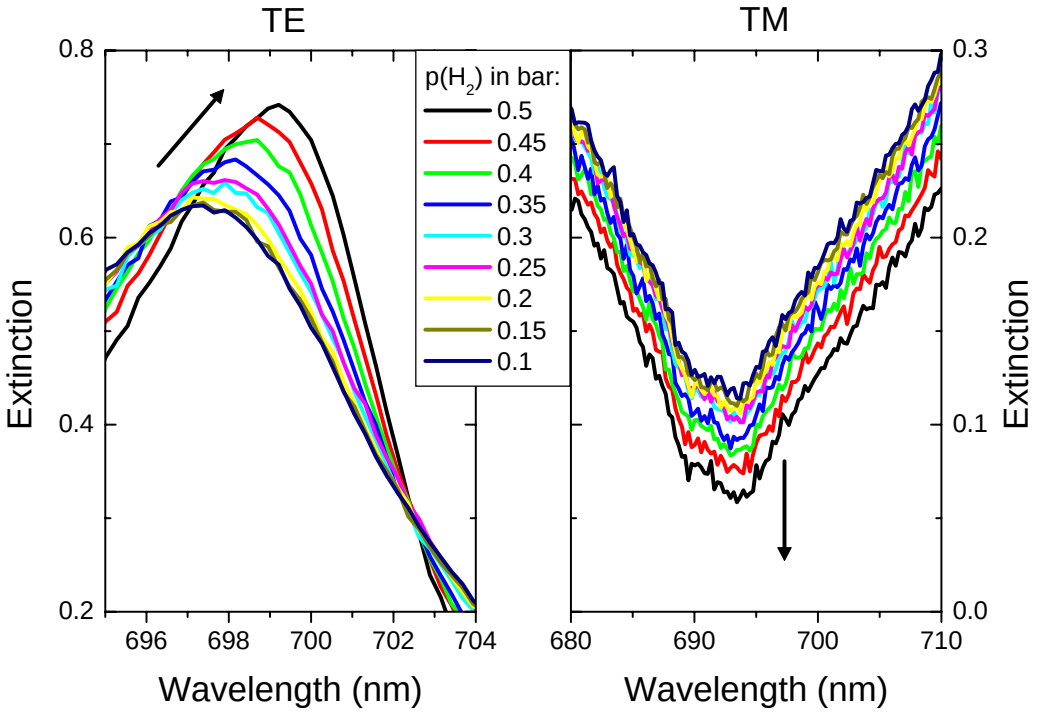

Figure 7.10: Extinction spectra for varying hydrogen pressure p_{H_2} in TE and TM polarization. Arrows indicate changes of the resonances.

Figure 7.10 shows measured extinction spectra of the sample that were taken at various hydrogen pressures. The plots contain narrow spectral regions around the characteristic features marked in Fig. 7.9(b). The experiments were done for decreasing p_{H_2}, starting at $p_{H_2} = 0.5$ bar. Clearly, a strong dependency of the TE resonance on the hydrogen atmosphere is observable. Increasing p_{H_2} causes the extinction of the resonance to rise. Additionally, the resonance shifts to higher wavelengths. In TM polarization, the extinction of the minimum decreases when p_{H_2} is increased. No shift to different wavelengths occurs for varying p_{H_2}, contrary to the expectations. Regarding the total extinction, we observe an converse behavior in opposite polarizations.

To get a more quantitative analysis about the influence of H_2 on the optical properties of the MPCS, we examine the influence of p_{H_2} on the spectral dependencies in Fig. 7.10. Figure 7.11(a) shows the wavelength of the quasiguided mode in TE polarization as a function of p_{H_2}. A nearly monotone increase is observable. Changing p_{H_2} from 0.1 to 0.5 bar results in a shift of the resonance of 1.76 nm (0.25%). This result probably explains why a similar shifting is not observed in TM polarization. Here, the minimum has a full-width-half-maximum of 30.4 nm (see Fig. 7.9). Therefore, the considered spectral feature is too broad to observe any wavelength changes. We assume that sharper polariton resonances show a similar wavelength shift even in TM polarization. The extinction at certain wavelengths in both polarizations is plotted in Fig. 7.11(b). We determine the extinction at $\lambda = 699.2$ nm in TE polarization and $\lambda = 693.2$ nm in TM polarization, respectively. These wavelengths correspond to the spectral positions of the resonances for

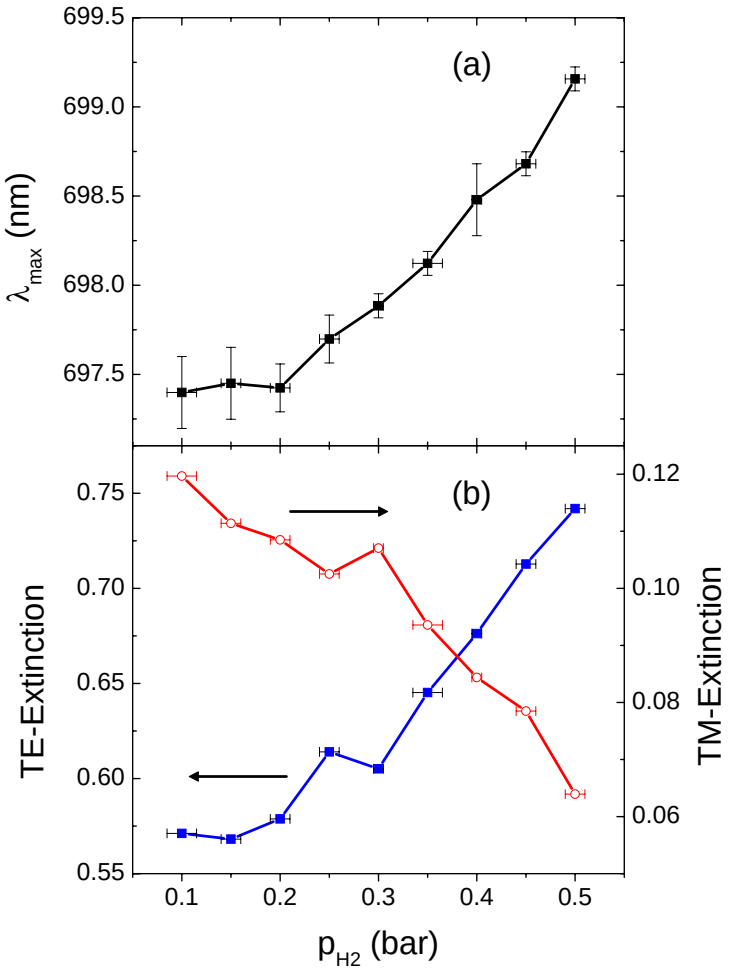

Figure 7.11: (a) Wavelength of the quasiguided mode in TE polarization as a function of p_{H2}. (b) Extinction at $\lambda = 699.21$ nm in TE polarization and at $\lambda = 693.18$ nm in TM polarization, respectively.

$p_{H_2} = 0.5$ bar in Fig. 7.10. Again, nearly monotone curves with slight deviations at $p_{H_2} = 0.3$ bar are obtained for both polarizations. A variation of p_{H_2} of 0.4 bar causes the extinction in TE polarization to increase by 0.17, the TM extinction drops by 0.04. Both modifications correspond to a change of $\approx 30\%$.

However, the observed spectral changes are smaller than expected. We believe that the low quality of the sample is responsible for this fact. During the fabrication process of the nanowires, the very thin Pd catalyst layer (thickness 2 nm) was probably damaged. This would cause a reduced efficiency for the hydrogen incorporation and hence reduced changes of the optical properties.

These results show that it is possible to build a hydrogen sensor that is based on the gasochromic coloration of metallic photonic crystal slabs. However, the observed spectral

changes of the optical properties as a function of the hydrogen concentration are not as pronounced as theoretically predicted. One possibility to further improve a sensor application is to enhance the hydrogen incorporation into the WO_3 waveguide layer. This could be realized by evaporating the Pd-catalyst *after* fabricating the nanostructures, avoiding its damaging during the manufacturing. To get a better sensitivity to changes in the hydrogen atmosphere, one has to increase the steepness of the slopes. Optical interference lithography on different waveguide materials [109] yielded very sharp resonances with an extinction change of 0.836 nm^{-1} in TE and 1.093 nm^{-1} in TM polarization, respectively. Adapting the electrochromism data from [103] to gasochromism, a change of the hydrogen concentration of $\Delta c_{H_2} = 1\%$ would result in a resonance shift of $\Delta\lambda \approx 13$ nm. Hence, $\Delta c_{H_2} = 0.1\% = 1‰$ should show a change of the extinction of 0.836 in TE and 1.093 in TM polarization.

To conclude, we have presented a new approach for a hydrogen sensor based on metallic photonic crystal slabs. WO_3 as waveguide material influences the optical properties of such MPCS by incorporating hydrogen gas. It was shown that both the extinction at certain wavelengths as well as the wavelengths of spectral features can be changed in varied hydrogen atmospheres. Differences in the hydrogen pressure of 0.4 bar can change the extinction by 30% or shift the resonances' wavelength by 0.25%. This allows to build a very compact and reconfigurable sensor. Its theoretical limit is in the sub-‰-range. Response and recovery times of the sensor have not yet been determined. To test the limits of this new hydrogen sensor approached, improved samples with very sharp resonances have to be used within the experimental setup. The setup itself could be improved by using mass-flow controllers to precisely determine the hydrogen concentration [110].

7.6 Comparison with other sensors

Different kinds of hydrogen sensors already exist. They are based on several chemical and physical principles. Some of them are discussed in the following and compared with our sensor approach. The details are taken from [111]. Table 7.1 shows a comparison of these different hydrogen sensors with our approach.

- **Catalytic Bead Sensors**

  Catalytic bead sensors consist of a wire at high temperatures that is surrounded by two beads. One of them is coated with a catalyst to faciliate the reaction with hydrogen. The idea is to measure the electrical resistance of the system as a function of the hydrogen atmosphere. Therefore, the system is integrated into a Wheatstone bridge.

- **Semiconductor Sensors**

  Here, also the electrical resistance of the sensor material, a semiconductor, is measured to determine the hydrogen concentration in the surrounding.

- **Electrochemical Sensors**

  They consist of a hydrogen-sensitive electrolyte that is sandwiched between two electrodes. Hydrogen coming into contact with the electrolyte causes a reversible chemical reaction. This reaction generates an electrical current that is proportional to the hydrogen concentration.

- **H-FET Sensor**

  A standard field effect transistor is used with palladium as gate material. Hydrogen causes a change in the electrical resistance of the palladium that depends on the hydrogen atmosphere in the surrounding.

	Catalytic bead sensor	Semiconductor sensor	Electrochemical sensor	H-FET sensor	Our approach
Detection Range (H_2)	1 - 5%	0 - 1000 ppm	100 - 1000 ppm	50 - 1000 ppm	‰- %
Response Time	10 - 30 sec	$<$ 1 sec	30 - 50 sec	$<$ 1 sec	$\approx$ 1 sec

Table 7.1: Comparison of different hydrogen sensors. $1‰ = 10^3$ ppm.

A number of further principles for hydrogen sensors exist, some of them use optical methods to measure the hydrogen concentration. As an example, we want to draw the attention to optical-fiber methods. They can be used to detect leakages in a wide spatial range. Here, fibers are coated with special materials that change their optical properties in different hydrogen atmospheres. As a result, the absorption of evanescent waves varies in different hydrogen concentrations. E.g. a sensor based on tapered fibers coated with thin palladium layers was presented in [110]. A fiber covered with a mixture of WO_3 and Pt was reported in [112]. Both sensors have a sensing range of up to 5% at a response time of less than 10 s. A different approach is to use surface plasmon resonances [113]. Covering the metal layer, that supports the surface plasmon, with WO_3 allows to vary the optical properties of the surrounding medium by adding hydrogen [100]. As a result, the surface plasmon resonance shifts as a function of the hydrogen concentration. This sensor is sensitive in the range of up to 10% at responds time of a few ten seconds.

It can be seen that our approach is in principle an adequate alternative to commercial devices. Regarding the detection range and the (estimated) response time, it could replace some of the available products. However, further tests and sample improvements

Material / Gas	H_2	CO	NO_2	NH_3
ZnO	x	x	x	x
SnO_2	x	x		x
V_2O_5				x
WO_3	x	x	x	x
CTO	x	x	x	x

Table 7.2: Sensitivity of sensor materials to different gases [114, 115]. Sensitivities are marked by a 'x'. They were determined by measuring the resistance of the materials.

have to be made as discussed.

A point that has to be mentioned is the additional sensitivity of specific sensor materials to several different gases. Wöllenstein *et al.* reported on a novel chip design consisting of several doped semiconductor materials that can be used to detect different gases [114]. Chung *et al.* observed a sensitivity of WO_3 to NO_2 [115]. Table 7.2 gives an overview about their results. The data were obtained by measuring the resistance change in various gas atmospheres. It was assumed that these gases can be adsorbed on the surfaces of the sensing semiconductors and dissociate into adsorbates. The latter then modify the resistance of the semiconductors depending on the gas concentration [115]. It was found that most of the tested materials are sensitive to multiple gases. Interestingly, WO_3 shows a reaction not only to H_2 but also to CO, NO_2 and NH_3. To our knowledge, nothing is known about the influence of the latter gases on the optical properties of WO_3. However, a possible influence should be taken into account. Although the probability for the appearance of CO, NO_2 and NH_3 is usually very small, their appearance could falsify the measured results.

Chapter 8

Conclusion and outlook

This work examines the influence of disorder on the optical properties of metallic photonic crystal slabs (MPCS). The aim is on the one hand to gain a deeper understanding of the underlying physics in these systems. On the other hand, the results obtained in this work can be used for improving further applications based on MPCS. MPCS consist of a 1-dim gold grating on top of an indium tin oxide (ITO) dielectric waveguide layer. Typically, the wires have a width of 100 nm, their height is 20 nm, and the period is between 200 nm and 600 nm. The thickness of the ITO-layer is 140 nm. Illuminating these structures with TE linearly polarized light excites a quasiguided mode in the ITO-layer, using TM linearly polarized light additionally excites a particle plasmon inside the nanostructures. In the latter case, a strong coupling between the TM quasiguided mode and the particle plasmon is observed and a waveguide-plasmon polariton is formed [9].

The main aspect of this work is to analyze the influence of different positional disorder types on the optical properties of such structures. Using electron-beam lithography allows to precisely control type and amount of disorder in the MPCS due to its high spatial accuracy. A linear white-light transmission setup is used to determine the optical properties of the so-fabricated samples. This procedure allows to determine a relation between positional disorder and the optical properties of MPCS. We consider normal light incidence where the resonances are excited and studied thoroughly. Also angle-resolved experiments were performed that reveal the bandstructure of the MPCS.

Two different disorder models are considered: the *frozen-phonon* model, where the positions of next-neighbors are uncorrelated, and the *long-range* model, where they are correlated. Frozen-phonon disorder is similar to the composition of heated solids where the atoms perform thermal movements around their equilibrium positions. Long-range disorder can be compared with the atomic arrangement in liquids. These disorder models are analyzed in great detail by means of statistical methods, the two-point correlation function, and a Fourier decomposition of the spatial arrangement of the nanowires. Their results underline the characteristics of the different disorder types.

Measuring the optical properties of samples with a disordered nanowire arrangement reveals a strong modification of the spectral features. Increasing disorder reduces the

amplitudes of the excited quasiguided mode in TE polarization and of the quasiguided mode-like polariton branch in TM polarization, independent of the disorder model. This reduction is caused by the reduced grating quality in the disordered systems that decreases the excitation efficiency of the quasiguided modes. The plasmonic part of the TM polariton resonance is nearly unaffected by disorder. Also the energy separation of the TM polariton branches is modified by increasing disorder. A simple model helps to understand this effect. It is based on a modified parameter V_2 that determines the coupling strength of the polariton. V_2 depends on the spatial overlap of the electrical fields of plasmon and quasiguided mode. Introducing positional disorder shifts the positions of nanostructures and plasmons which reduces the spatial overlap with the quasiguided mode. Calculating the overlap in this simple model for different disorder types and amounts shows that the shrinking of the polariton coupling strength is smaller for frozen-phonon disorder than for long-range disorder.

Long-range disorder adds inhomogeneous broadening to the resonances. A straightforward theory derived from diffraction theory allows to clarify these observations. It combines the Fourier analysis of the spatial arrangement of the nanowires with the dispersion $E(k)$ of the structure. As a result, the Fourier peaks are transformed from k-space into energy space. These energy peaks determine the energies of the excited resonances, their amplitudes are given by the height of the corresponding Fourier components. Using them as parameters in the lineshape functions of TE and TM polarization (see Eqn. (2.29) and Eqn. (2.35), respectively), reveals a nice agreement with the experimental observations. Now the inhomogeneous broadening is understandable. Frozen-phonon disorder as a typical example of uncorrelated disorder simply reduces the amplitude of the Fourier peak at the first reciprocal lattice vector, as described by the Debye-Waller factor in diffraction theory [16]. The Fourier decomposition of systems with long-range disorder shows additional peaks around the first reciprocal lattice vector. These peaks cause an inhomogeneous broadening in Fourier space, similar to the diffraction pattern of liquids [63]. Hence, multiple resonances at different energies are excited.

The bandstructure of such MPCS can be derived from angle-resolved extinction measurements. In TM polarization, the bandstructure is characterized in the ordered system by three pronounced bands that can be attributed to the different polariton branches. In TE polarization, two bands occurs, i.e. the bandstructure of symmetric and antisymmetric quasiguided mode. It was shown that these bands are separated by energy gaps [9]. In this thesis, disorder was found to have a strong influence on the bandstructure. Increasing frozen-phonon disorder retains the bandstructure but reduces the bandsplitting, as predicted in the V_2-model. Long-range disorder destroys the bandstructure completely, no separated bands are observable for disorder amounts of more than 20%. This effect is caused by the excitation of multiple resonances at different energies as described above. Each resonance gives rise to a different polariton, and the overlap of the bandstructures results in a vanishing of pronounced bands.

In a second part of this thesis, two applications based on the perfect metallic photonic crystal slab are presented. We report on novel concepts for an all-optical switch and for a hydrogen sensor. An additional layer of a photoaddressable polymer (PAP) on top of the ITO waveguide layer allows to optically switch the optical properties of the metallic photonic crystal. When exposing this material within its absorption band, a photoisomerization process from the *trans*- to the *cis*-configuration occurs. The corresponding shivering movement can lead to a reorientation of the PAP-molecules perpendicular to the polarization of the incident light. This reorientation results in a birefringence $\Delta n = n_\perp - n_\parallel$ with $n_\perp$ and $n_\parallel$ as refractive index perpendicular and parallel to the light polarization, respectively. Probing the extinction with different polarizations allows to determine either $n_\perp$ or $n_\parallel$. Our measurements showed that the resonances in TE and TM polarizations shift to opposite wavelengths, as described by $n_\perp$ and $n_\parallel$. This shifting is reproducible although a saturation effect occurs. Using a modified material could diminish the out-of-plane orientation of the molecules, responsible for the saturation. The results prove that MPCS can be used to build an all-optical switch. The experimental observations agree well with scattering-matrix results.

Using tungsten oxide (WO_3) as waveguide layer causes the optical properties of MPCS to vary depending on the hydrogen concentration in the surrounding. Different mechanisms change the optical properties of WO_3 by incorporating charges into the material. These processes have in common that WO_3-based complexes are formed that have different optical properties than pure WO_3. We make use of gasochromism where hydrogen gas is incorporated into the WO_3. Both the absorption coefficient κ and the refractive index n are changed [103]. Our experiments showed the influence of gasochromism on the extinction of MPCS. We found both a shift of the excited resonances along the energy and along the extinction axis. These shifts are caused by the H_2-influence on n and κ of the WO_3-layer. We observed large extinction modifications for rather large changes of the hydrogen concentration Δc_{H_2}. Typically, the extinction varies on the order of 30% for $\Delta c_{H_2} \approx 40\%$. This sensitivity of our sensor on Δc_{H_2} of a few percent is not yet satisfying. We account the low quality of the available samples to be responsible for the experimental results not being as good as expected. We assume that the fabrication of the nanowires damaged the Pd catalyst on the WO_3 so that the incorporation of H_2 into the WO_3-layer was reduced. The sensitivity of our hydrogen sensor should reach down to the sub-‰-range.

In addition to the aspects of metallic photonic crystal slabs treated in this work, further points should be discussed in future. Most of the disorder-induced spectral features are understood, but there are still questions to be answered. Especially the theoretical description of the optical properties of disordered MPCS is still challenging. While the presented straightforward theory explains many of the observed effects, its results do not

completely agree with the measurements, yet. Some extinction spectra in TM polarization can not be reproduced in detail by our theoretical model. The presented idea of how to determine the variation of V_2 in disordered systems seems to be not completely correct. Additionally, no theory to determine the influence of disorder on the coupling between symmetric and antisymmetric quasiguided mode exists. Therefore, this coupling is so far taken to be disorder-independent. A theory including both dependencies would be able to show a better agreement between measured and simulated bandstructure in disordered systems. Such a theory could be based on a Hamiltonian as in Eqn. (2.36).

The influence of disorder on the nonlinear optical properties of MPCS is still unreported. In perfectly ordered systems, the dephasing time T_2 of the waveguide-plasmon polariton is enhanced compared to the pure particle plasmon [39]. Also polariton beats due to the interference between the polariton branches are observed. The extinction spectra of disordered MPCS in Chapter 5 showed strong deviations from the extinction of perfectly ordered MPCS. Depending on the disorder type either a reduction of extinction peaks or an additional inhomogeneous broadening is observed. For large disorder amounts, the extinction is dominated by an (inhomogeneously broadened) plasmon peak in TM polarization. Repeating the experiments by Zentgraf *et al.* [39] for increasing disorder amounts should therefore show a transition from an enhanced T_2 to dephasing times more or less identical with T_2 of the pure particle plasmon. Next-neighbor correlations should reveal an additional T_2-modification. Due to the excited multiple quasiguided modes, multiple polariton branches should interfere with each other causing further polariton beats.

Similar information can be obtained with echo experiments in inhomogeneously broadened systems [116]. One example is the photon echo in solids [117]. If the experimental time scale is small enough so that interactions, that destroy the coherence, can be neglected, the system can answer with an echo to an excitation. A resonant $\pi/2$-pulse excites the Bloch-vectors to the equatorial plane of the Bloch-sphere where they perform oscillations. Each vector corresponds to one state of the inhomogeneous systems. Their oscillation frequencies ω_i are determined by the energies of the individual states i. Since the ω_i are distributed in a disordered system, the Bloch-vectors loose their coherence and start to oscillate out of phase. A π-pulse at time $\tau < T_2$ inverses the oscillation direction of the Bloch-vectors, so that they are again in phase at time 2τ. The system answers with a macroscopic signal. Such experiments are performed to examine phase-destroying processes [116] or to distinguish between spontaneous and stimulated photon echos [118]. The extinction spectra of MPCS with long-range disorder show additional waveguide modes at different energies that cause the resulting resonance to be inhomogeneously broadened. For this reason we can expect that this system will respond with a photon echo to ultrashort laser pulse excitation. Attention has to be paid to the short dephasing times in MPCS that are on the order of a few ten fs in perfect MPCS [39] and a few fs in pure particle plasmons [22, 119].

Cross-correlation frequency resolved optical gating (XFROG) experiments can be used to examine the propagation of ultrashort laser pulses through MPCS [36]. A breakup of

the initial laser pulse into two spectrally and temporally separated pulses was found in TE polarization [120]. The temporal phase performs jumps on the order of $\pi/2$ due to beating effects between these pulses. A jump of the spectral phase of $\pi/2$ is caused by an imaginary part of the transmission. Therefore, long-range disorder should modify the XFROG-spectrogram because of its inhomogeneous broadening of the TE-resonance. Similar effects are expected in TM polarization.

As already discussed, localization of light could be possible in disordered MPCS because the quasiguided mode propagates in the direction of the 1-dim disorder. To detect light localization, a XFROG-experiment could be used. The localized spectral components should be stored in the disordered MPCS for a time longer than the typical propagation times. Thus, pronounced components in the XFROG-spectrogram should appear. Another possibility to detect localized light could be to use scanning near-field optical microscopy (SNOM) [121]. Localization could be then detected by determining the electromagnetic field in disordered MPCS.

The next step in the PAP-experiments should be to replace the polymer material with a modified PAP [85, 91], warranting the reproducibility of the switching behavior even after many cycles. Covering a metallic photonic crystal slab with this material allows further experiments as an application as all-optical switch. Of course, the final step should be the realization of an all-optical switch device.

Regarding the development of the hydrogen sensor the principal mechanism was demonstrated. However, the quality of the signal detection is not yet useful in a rough environment such as in industry. In the future, the quality of the samples has to be improved. This includes to find the best configuration for the catalyst layer such as thickness and material (palladium or platinum). Possible damaging in the fabrication process has to be excluded. Improving the quality of the metallic grating arrangement helps to rise the sensitivity of the sensor. A promising fabrication method to increase the steepness of the spectral features is optical interference lithography [109]. In the experiments, the time-dependency of the observed spectral effects has to be measured in order to determine the response time of the possible sensor. As for the PAP-experiment, the final step should be the realization of the device. The experimental setup could be improved by using mass-flow controllers to precisely determine the hydrogen concentration inside the chamber. Also a possible influence of different gases like CO, NO_2 and NH_3 on the optical properties should be taken into account.

To summarize, dealing with disorder in MPCS has the potential to solve further interesting questions. Furthermore, this thesis has shown that MPCS can be utilized to develop interesting future applications.

Appendix A

Autocorrelation

A.1 General remarks

In this chapter we want to derive the formulas for the two-point particle function (TPCF) of disordered structures. As we are working with grating structures, we consider a 1-dimensional problem. For simplicity we neglect the size of the nanostructures, so that the nanostructures can be described by an arrangement of δ-peaks. Further details about the mathematics of correlations and δ-functions can be found in [122].

The TPCF of the disordered samples is given by the autocorrelation of the spatial positions of the nanostructures. For two functions $f(x)$ and $g(x)$, the crosscorrelation is defined as

$$(f \star g)(x) = \int_{-\infty}^{\infty} f(\alpha) g(\alpha - x)\, d\alpha. \tag{A.1}$$

One can simply prove that

$$(f \star g)(x) \neq (g \star f)(x). \tag{A.2}$$

With $g(x) = f(x)$ we receive the autocorrelation

$$(f \star f)(x) = \int_{-\infty}^{\infty} f(\alpha) f(\alpha - x)\, d\alpha. \tag{A.3}$$

Since we want to describe the disordered systems by a sequence of δ-functions, the following relation will be very useful:

$$(f \star \delta)(x) = \int_{-\infty}^{\infty} f(\alpha) \delta(\alpha - x)\, d\alpha = f(x). \tag{A.4}$$

This means that the crosscorrelation of a function with a δ-function returns the function itself.

A.2 Perfect grating

Let us start with the perfect periodic grating. Such systems can be described by a comb of δ-functions. The δ-functions are supposed to be at positions $x_i = x_0 + i \cdot d_0$ $(i = 0, \ldots N)$, where x_0 is the position of the zeroth wire, d_0 is the grating period and $N + 1$ is the number of wires:

$$comb(x) = \sum_{i=0}^{N} \delta(x - x_0 - i \cdot d_0). \tag{A.5}$$

The crosscorrelation of a function $f(x)$ with $comb(x)$ yields

$$(f \star comb)(x) = \sum_{i=0}^{N} f(x + x_0 + i \cdot d_0), \tag{A.6}$$

because by using Eqn. (A.4) we calculate

$$\begin{aligned}
(f \star comb)(x) &= \int_{-\infty}^{\infty} f(\alpha) comb(\alpha - x)\, d\alpha \\
&= \int_{-\infty}^{\infty} f(\alpha) \sum_{i=0}^{N} \delta(\alpha - x - x_0 - i \cdot d_0)\, d\alpha \\
&= \int_{-\infty}^{\infty} \sum_{i=0}^{N} f(\alpha) \delta(\alpha - x - x_0 - i \cdot d_0)\, d\alpha \\
&= \sum_{i=0}^{N} \int_{-\infty}^{\infty} f(\alpha) \delta(\alpha - x - x_0 - i \cdot d_0)\, d\alpha \\
&= \sum_{i=0}^{N} f(x + x_0 + i \cdot d_0).
\end{aligned}$$

With $f(x) = comb(x)$ we see that the autocorrelation and hence the TPCF of a perfect periodic grating structure is given by

$$\begin{aligned}
(comb \star comb)(x) &= \sum_{i=0}^{N} comb(x + x_0 + i \cdot d_0) \\
&= \sum_{i=0}^{N} \sum_{j=0}^{N} \delta(x + x_0 + i \cdot d_0 - x_0 - j \cdot d_0) \\
&= \sum_{i=0}^{N} \sum_{j=0}^{N} \delta(x - (j - i) d_0)
\end{aligned}$$

This results denotes that the TPCF of a perfect grating is simply the sum of perfectly ordered combs of δ-peaks, resulting in a perfectly ordered comb:

$$(comb \star comb)(x) = \sum_{i=0}^{N} \sum_{j=0}^{N} \delta(x - (j - i) d_0). \tag{A.7}$$

A.3 Frozen-phonon disorder

In this disorder model we vary the position of the nanostructures around their original grid position. Therefore the comb-function, describing the arrangement, has to be modified. We do this by adding a shift Δx_i to the positions, and we receive the position of the i-th nanostructure:

$$x_i = x_0 + i \cdot d_0 + \Delta x_i. \tag{A.8}$$

The disordered system can be described by the following function:

$$comb_1(x) := \sum_{i=0}^{N} \delta(x - x_0 - i \cdot d_0 - \Delta x_i). \tag{A.9}$$

For the crosscorrelation of a function $f(x)$ with $comb_1(x)$ we calculate:

$$\begin{aligned}
(f \star comb_1)(x) &= \int_{-\infty}^{\infty} f(\alpha) comb_1(\alpha - x)\, d\alpha \\
&= \int_{-\infty}^{\infty} f(\alpha) \sum_{i=0}^{N} \delta(\alpha - x - x_0 - i \cdot d_0 - \Delta x_i)\, d\alpha \\
&= \sum_{i=0}^{N} \int_{-\infty}^{\infty} f(\alpha) \delta(\alpha - x - x_0 - i \cdot d_0 - \Delta x_i)\, d\alpha \\
&= \sum_{i=0}^{N} f(x + x_0 + i \cdot d_0 + \Delta x_i).
\end{aligned}$$

With $f(x) = comb_1(x)$ we can determine the autocorrelation and hence the TPCF of a structure with frozen-phonon disorder:

$$\begin{aligned}
(comb_1 \star comb_1)(x) &= \sum_{i=0}^{N} comb_1(x + x_0 + i \cdot d_0 + \Delta x_i) \\
&= \sum_{i=0}^{N} \sum_{j=0}^{N} \delta(x + x_0 + i \cdot d_0 + \Delta x_i - x_0 - j \cdot d_0 - \Delta x_j) \\
&= \sum_{i=0}^{N} \sum_{j=0}^{N} \delta(x - (j - i) d_0 + \Delta x_i - \Delta x_j).
\end{aligned}$$

A.4 Long-range disorder

The situation in systems with long-range disorder is different since here the positions of the nanostructures are related to the preceding nanostructure. The position of the i-th nanostructure can be described by

$$x_i = x_0 + i \cdot d_0 + \sum_{n=1}^{i} \Delta x_n. \tag{A.10}$$

Therefore, the total arrangement in the system is given by

$$comb_2(x) := \sum_{i=0}^{N} \delta(x - x_0 - i \cdot d_0 - \sum_{n=1}^{i} \Delta x_n). \tag{A.11}$$

The crosscorrelation of a function $f(x)$ with $comb_2(x)$ is

$$\begin{aligned}
(f \star comb_2)(x) &= \int_{-\infty}^{\infty} f(\alpha) comb_2(\alpha - x)\, d\alpha \\
&= \int_{-\infty}^{\infty} f(\alpha) \sum_{i=0}^{N} \delta(\alpha - x - x_0 - i \cdot d_0 - \sum_{n=1}^{i} \Delta x_n)\, d\alpha \\
&= \sum_{i=0}^{N} \int_{-\infty}^{\infty} f(\alpha) \delta(\alpha - x - x_0 - i \cdot d_0 - \sum_{n=1}^{i} \Delta x_n)\, d\alpha \\
&= \sum_{i=0}^{N} f(x + x_0 + i \cdot d_0 + \sum_{n=1}^{i} \Delta x_n).
\end{aligned}$$

The autocorrelation of a system with long-range disorder is given by

$$\begin{aligned}
(comb_2 \star comb_2)(x) &= \sum_{i=0}^{N} comb_2(x + x_0 + i \cdot d_0 + \sum_{n=1}^{i} \Delta x_n) \\
&= \sum_{i=0}^{N} \sum_{j=0}^{N} \delta(x + x_0 + i \cdot d_0 + \sum_{n=1}^{i} \Delta x_n - x_0 - j \cdot d_0 - \sum_{m=1}^{j} \Delta x_m) \\
&= \sum_{i=0}^{N} \sum_{j=0}^{N} \delta(x - (j - i) d_0 + \sum_{n=1}^{i} \Delta x_n - \sum_{m=1}^{j} \Delta x_m).
\end{aligned}$$

Appendix B

Spatial overlap

The tables in this appendix show the results from simulating the spatial overlap of particle plasmon and quasiguided mode in disordered metallic photonic crystals (see Chapt. 5.4). Each table contains the data for a certain disorder type. The results were obtained by averaging over 200 different grating realizations for each disorder type and amount. Each grating consisted of 300 wires with a period of 400 nm, the wires' width was set to 100 nm. The columns contain the disorder amount in %, the calculated spatial overlap V_2^{Dis} (arb. units), the standard deviation and the normalized V_2^{Dis} according to Eqn. (5.5).

Disorder (%)	V_2^{Dis} (arb. units)	Standard Deviation	V_2^{Dis} (norm.)
0	6873.187	0	1
10	6642.97294	5.48941	0.96651
20	6318.67201	22.86439	0.91932
30	5791.02789	46.12405	0.84255
40	5117.47546	81.75045	0.74456
50	4310.82602	117.09996	0.62719
60	3410.18705	160.13787	0.49616
70	2506.47011	215.91976	0.36467
80	1575.06679	237.69205	0.22916
90	796.81997	258.1856	0.11593
100	336.81521	174.31435	0.049

Table B.1: V_2 for uniform frozen-phonon disorder.

Disorder (%)	V_2^{Dis} (arb. units)	Standard Deviation	V_2^{Dis} (norm.)
0	6873.187	0	1
10	6517.95435	18.20466	0.94832
20	5862.01978	65.10016	0.85288
30	4911.47591	129.75192	0.71458
40	3837.2195	178.61279	0.55829
50	2797.6143	231.19928	0.40703
60	1915.50804	264.57575	0.27869
70	1249.93652	258.20657	0.18186
80	777.42801	259.77885	0.11311
90	515.10591	224.93718	0.07494
100	388.0621	194.79846	0.05646

Table B.2: V_2 for Gaussian frozen-phonon disorder.

Disorder (%)	V_2^{Dis} (arb. units)	Standard Deviation	V_2^{Dis} (norm.)
0	6760.05	0	1
10	3670.31052	1398.07326	0.54294
20	1864.26986	966.62137	0.27578
30	1139.87094	570.86251	0.16862
40	989.59997	509.27825	0.14639
50	757.21287	386.51849	0.11201
60	606.90973	314.68572	0.08978
70	509.9807	253.48449	0.07544
80	435.65832	216.06595	0.06445
90	396.63128	201.03869	0.05867
100	358.13038	194.01703	0.05298

Table B.3: V_2 for uniform long-range disorder.

Disorder (%)	V_2^{Dis} (arb. units)	Standard Deviation	V_2^{Dis} (norm.)
0	6760.05	0	1
10	2461.00299	1182.88716	0.36405
20	1334.54647	665.0017	0.19742
30	844.95744	432.00806	0.12499
40	683.31237	346.1925	0.10108
50	526.74814	261.63946	0.07792
60	478.21642	245.96463	0.07074
70	413.94021	190.48106	0.06123
80	383.11441	199.8288	0.05667
90	365.04611	181.56334	0.054
100	348.70557	183.59602	0.05158

Table B.4: V_2 for Gaussian long-range disorder.

Appendix C

Theoretical modelling

The calculation of the theoretical extinction spectra is done in several steps (see Chapter 5.5):

1. In a first step, the extinction of the perfect sample with period d_0 is measured at normal light incidence in TE and TM polarization.

2. This step checks whether the period of the sample has the desired value d_0. Therefore, the dispersion $E(k)$ of the structure in TE polarization is calculated by using Eqn. (2.26). Then, the measured energy E_0 of the TE resonance is compared with the dispersion. E_0 corresponds to a momentum k_0 in the dispersion and hence to a period d of the real sample. If $d \neq d_0$, the fabricated sample does not have the desired period. In this case, the predetermined coordinates of the nanowires are multiplied by a factor d/d_0 to adapt them to the real structure.

3. Given the measured energies of the polariton branches and the period d of the real structure, the dispersion $E(k)$ in TM polarization is determined with Eqn. (2.34). The parameters E_{Pl} and V_2 are varied, so that the simulated energies at momentum $k = 2\pi/d$ correspond to the measured energies.

4. The measured extinction resonances of the perfect sample are fitted with a Fano-form in TE polarization [Eqn. (2.26)] and with the absorption curve of coupled oscillators in TM polarization [Eqn. (2.34)], respectively. Except for energy and amplitude, the parameters of these fits are used as disorder-independent parameters in the calculation later on.

5. The Fourier analysis of the spatial grating arrangement is calculated. It requires the exact coordinates of the individual nanostructures. Only the k-range around the first reciprocal lattice vector at $k = 2\pi/d_0$ is considered: $k \in [\pi/d_0, 3\pi/d_0]$ (see next step).

6. The dispersion $E(k)$ of the structure is determined by using Eqn. (2.26) for TE polarization and Eqn. (2.34) for the dispersion in TM polarization. The restriction to a small k-range becomes reasonable: This limited k-range corresponds to

an energy range which covers the spectral range from the experiment. For each disorder amount, the appropriate normalized coupling parameter V_2^{Dis} is used in the calculation of the dispersion in TM polarization, see Eqn. (5.6).

7. Combining Fourier analysis and dispersion $E(k)$ yields energy and strength of the excited resonances. A Fourier component with momentum k_j and amplitude A_j leads to resonances with amplitude $I_j = cA_j^2$. We set $c = 1$. The calculation of the respective resonances use $E_j = E(k_j)$ as important parameter. This is done for all Fourier components in the examined k-range. In TE polarization, a Fourier component excites a single resonance, whereas two resonances are excited in TM polarization.

8. The energies E_j and amplitudes I_j of the excited resonances are taken as parameters in the lineshape function $\alpha_j(E)$ of the structure. The other lineshape parameters were already determined by fitting the lineshape.

9. The program is run first for the perfect sample. This is done to check for little deviations of the simulations from the measurements. Because the maxima of the resonances in the lineshape functions do not necessarily coincident with the energies E_j, possibly small energy shifts have to be included.

10. The total extinction $\alpha_{Dis}^{Pol}(E)$ of the sample is the summation over all excited resonances $\alpha_{Dis}^{Pol}(E) = \sum_j \alpha_j^{Pol}(E)$, where Pol denotes the polarization (TE or TM).

Bibliography

[1] J. D. Joannopoulos, P. R. Villeneuve, and S. Fan, *Photonic crystals: putting a new twist on light*, Nature **386**, 143 (1997).

[2] E. Yablonovitch, *Inhibited spontaneous emission in solid-state physics and electronics*, Phys. Rev. Lett. **58**, 2059 (1987).

[3] S. John, *Strong localization of photons in certain disordered dielectric superlattices*, Phys. Rev. Lett. **58**, 2486 (1987).

[4] M. Bayindir, B. Temelkuran, and E. Ozbay, *Photonic-crystal-based beam splitters*, Appl. Phys. Lett. **77**, 3902 (2000).

[5] A.-L. Fehrembach, S. Enoch, and A. Sentenac, *Highly directive light sources using two-dimensional photonic crystal slabs*, Appl. Phys. Lett. **79**, 4280 (2001).

[6] T. F. Krauss, R. M. De La Rue, and S. Brand, *Two-dimensional photonic-bandgap structures operating at near-infrared wavelengths*, Nature **383**, 699 (1996).

[7] E. R. Brown and O. B. McMahon, *Large electromagnetic stop bands in metallodielectric photonic crystals*, Appl. Phys. Lett. **67**, 2138 (1995).

[8] S. Linden, J. Kuhl, and H. Giessen, *Controlling the interaction between light and nanoparticles: Selective suppression of extinction*, Phys. Rev. Lett. **86**, 4688 (2001).

[9] A. Christ, S. G. Tikhodeev, N. A. Gippius, J. Kuhl, and H. Giessen, *Waveguide-plasmon polaritons: Strong coupling of photonic and electronic resonances in a metallic photonic crystal slab*, Phys. Rev. Lett. **91**, 183901 (2003).

[10] A. Christ, *Optical properties of metallic photonic crystal structures*, Ph.D. thesis, Universität Marburg (2005).

[11] Y. A. Vlasov, V. N. Astratov, A. V. Baryshev, A. A. Kaplyanskii, O. Z. Karimov, and M. F. Limonov, *Manisfestation of intrinsic defects in optical properties of self-organized opal photonic crystals*, Phys. Rev. **E 61**, 5784 (2000).

[12] A. F. Koenderink, A. Lagendijk, and W. L. Vos, *Optical extinction due to intrinsic structural variations of photonic crystals*, Phys. Rev. **B 72**, 153102 (2005).

[13] J. Bertolotti, S. Gottardo, D. S. Wiersma, M. Ghulinyan, and L. Pavesi, *Optical necklace states in Anderson localized 1D systems*, Phys. Rev. Lett. **94**, 113903 (2005).

[14] R. Sainidou, N. Stefanou, and A. Modinos, *Widening of photonic transmission gaps via Anderson localization*, Phys. Rev. Lett. **94**, 205503 (2005).

[15] V. D. Freilikher, B. A. Liansky, I. V. Yurkevich, A. A. Maradudin, and A. R. McGurn, *Enhanced transmission due to disorder*, Phys. Rev. **E 51**, 6301 (1995).

[16] C. Kittel, *Introduction to Solid State Physics* (John Wiley & Sons, 1996).

[17] U. Kreibig and M. Vollmer, *Optical Properties of Metal Clusters* (Springer-Verlag, Berlin, 1995).

[18] C. F. Bohren and D. R. Huffman, *Absorption and Scattering of Light by Small Particles* (Wiley Science Paperback Series, 1998).

[19] P. B. Johnson and R. W. Christy, *Optical constants of the noble metals*, Phys. Rev. **B 6**, 4370 (1972).

[20] N. E. Christensen and B. O. Seraphin, *Relativistic band calculation and the optical properties of gold*, Phys. Rev. **B 4**, 3321 (1971).

[21] G. Mie, *Beiträge zur Optik trüber Medien, speziell kolloidaler Metallösungen*, Ann. d. Phys. **25**, 377 (1908).

[22] B. Lamprecht, G. Schider, R. T. Lechner, H. Ditlbacher, J. R. Krenn, A. Leitner, and F. R. Aussenegg, *Metal nanoparticle gratings: influence of dipolar particle interaction on the plasmon resonance*, Phys. Rev. Lett. **84**, 4721 (2000).

[23] W. Rechberger, A. Hohenau, A. Leitner, J. R. Krenn, B. Lamprecht, and F. R. Aussenegg, *Optical properties of two interacting gold nanoparticles*, Opt. Commun. **220**, 137 (2003).

[24] C. Rockstuhl, M. G. Salt, and H. P. Herzig, *Application of the boundary-element method to the interaction of light with single and coupled metallic nanoparticles*, J. Opt. Soc. Am. **A 20**, 1969 (2003).

[25] H. R. Stuart and D. G. Hall, *Enhanced dipole-dipole interaction between elementary radiators near a surface*, Phys. Rev. Lett. **80**, 5663 (1998).

[26] E. Hecht, *Optik* (Oldenbourg Verlag, 2001).

[27] S. G. Johnson, S. Fan, P. R. Villeneuve, J. D. Joannopoulos, and L. A. Kolodziejski, *Guided modes in photonic crystal slabs*, Phys. Rev. **B 60**, 5751 (1999).

[28] S. Fan and J. D. Joannopoulos, *Analysis of guided resonances in photonic crystal slabs*, Phys. Rev. **B 65**, 235112 (2002).

[29] M. K. Barnoski, *Introduction to Integrated Optics* (Plenum Press, New York, 1974).

[30] S. G. Tikhodeev, A. L. Yablonskii, E. A. Muljarov, N. A. Gippius, and T. Ishihara, *Quasiguided modes and optical properties of photonic crystal slabs*, Phys. Rev. **B 66**, 045102 (2002).

[31] H. Kogelnik and V. Ramaswamy, *Scaling rules for thin-film optical waveguides*, Appl. Opt. **13**, 1857 (1974).

[32] S. Linden, *Kontrolle der Wechselwirkung zwischen Licht und Partikelplasmonen durch selektive Unterdrückung der Extinktion*, Ph.D. thesis, Universität Marburg (2001).

[33] P. K. Tien, R. Ulrich, and R. J. Martin, *Modes of propagating light waves in thin deposited semiconductor films*, Appl. Phys. Lett. **14**, 291 (1969).

[34] M. L. Dakss, L. Kuhn, P. F. Heidrich, and B. A. Scott, *Grating coupler for efficient excitation of optical guided waves in thin films*, Appl. Phys. Lett. **16**, 523 (1970).

[35] A. Christ, T. Zentgraf, J. Kuhl, S. G. Tikhodeev, N. A. Gippius, and H. Giessen, *Optical properties of planar metallic photonic crystal structures: Experiment and theory*, Phys. Rev. **B 70**, 125113 (2004).

[36] A. Schönhardt, *Pulspropagation in metallischen photonischen Kristallen*, Master's thesis, Universität Bonn (2005).

[37] U. Fano, *Effects of configuration interaction on intensities and phase shifts*, Phys. Rev. **124**, 1866 (1961).

[38] A. L. Yablonskii, E. A. Muljarov, N. A. Gippius, S. G. Tikhodeev, T. Fujita, and T. Ishihara, *Polariton effect in distributed feedback microcavities*, J. Phys. Soc. Jpn. **70**, 1137 (2001).

[39] T. Zentgraf, A. Christ, J. Kuhl, and H. Giessen, *Tailoring ultrafast dephasing of quasiparticles in metallic photonic crystals*, Phys. Rev. Lett. **93**, 243901 (2004).

[40] M. W. Klein, T. Tritschler, M. Wegener, and S. Linden, *Lineshape of harmonic generation by metallic nanoparticles and metallic photonic crystal slabs*, Phys. Rev. **B 72**, 115113 (2005).

[41] J. M. Ziman, *Models of Disorder* (Cambridge University Press, 1979).

[42] P. M. Ossi, *Disordered Materials* (Springer-Verlag, Berlin, 2003).

[43] C. F. Klingshirn, *Semiconductor Optics* (Springer-Verlag, Berlin, 1997).

[44] P. Y. Yu and M. Cardona, *Fundamentals of Semiconductors* (Springer-Verlag, Berlin, 1999).

[45] D. Levine and P. J. Steinhardt, *Quasicrystals: A new class of ordered structures*, Phys. Rev. Lett. **53**, 2477 (1984).

[46] F. J. Dyson, *The dynamics of a disordered linear chain*, Phys. Rev. **92**, 1331 (1953).

[47] S. K. O'Leary and S. Zukotynski, *Semiclassical density-of-states and optical-absorption analysis of amorphous semiconductors*, Phys. Rev. **B 51**, 4143 (1995).

[48] H. Matsuda and K. Ishii, *Localization of normal modes and energy transport in the disordered harmonic chain*, Prog. Theor. Phys. Suppl. **45**, 56 (1970).

[49] D. G. Blair, *Mean free path of electrons in a one-dimensional liquid model*, Phys. Rev. **B 5**, 2097 (1972).

[50] D. J. Thouless, *Localization distance and mean free path in one-dimensional disordered systems*, J. Phys. C **6**, L49 (1973).

[51] P. W. Anderson, *Absence of diffusion in certain random lattices*, Phys. Rev. **109**, 1492 (1958).

[52] D. S. Wiersma, P. Bartolini, A. Lagendijk, and R. Righini, *Localization of light in a disordered medium*, Nature **390**, 671 (1997).

[53] A. Z. Genack and N. Garcia, *Observation of photon localization in a three-dimensional disordered system*, Phys. Rev. Lett. **66**, 2064 (1991).

[54] A. F. Ioffe and A. R. Regel, *Non-crystalline, amorphous, and liquid electronic semiconductors*, Prog. Semicond. **4**, 237 (1960).

[55] F. Intonti, V. Emiliani, C. Lienau, T. Elsaesser, V. Savona, E. Runge, R. Zimmermann, R. Nötzel, and K. H. Ploog, *Quantum mechanical repulsion of exciton levels in a disordered quantum well*, Phys. Rev. Lett. **87**, 076801 (2001).

[56] G. v. Freymann, U. Neuberth, M. Deubel, M. Wegener, G. Khitrova, and H. M. Gibbs, *Level repulsion in nanophotoluminescence spectra from single* GaAs *quantum wells*, Phys. Rev. **B 65**, 205327 (2002).

[57] S. N. Evangelou and E. N. Economou, *Spectral density singularities, level statistics, and localization in a sparse random matrix ensemble*, Phys. Rev. Lett. **68**, 361 (1992).

[58] B. I. Shklovskii, B. Shapiro, B. R. Sears, P. Lambrianides, and H. B. Shore, *Statistics of spectra of disordered systems near the metal-insulator transition*, Phys. Rev. **B 47**, 11487 (1993).

[59] D. Nau, A. Christ, S. Linden, J. Kuhl, and H. Giessen, *The influence of disorder in metallic photonic crystal slabs*, *CLEO/IQEC and PhAST Technical Digest on CDROM*, IThB6 (The Optical Society of America, Washington, DC, 2004).

[60] K. Maschke, H. Overhof, and P. Thomas, *On the description of multiple scattering processes in amorphous and crystalline semiconductors*, phys. stat. sol. (b) **57**, 237 (1973).

[61] K. Huang, *Statistische Mechanik III* (Bibliographisches Institut Mannheim, 1964).

[62] T. Zentgraf, A. Christ, J. Kuhl, N. A. Gippius, S. G. Tikhodeev, D. Nau, and H. Giessen, *Metallodielectric photonic crystal superlattices: Influence of periodic defects on transmission properties*, Phys. Rev. **B 73** (2006).

[63] F. Zernike and J. A. Prins, *Die Beugung von Röntgenstrahlen in Flüssigkeiten als Effekt der Molekülanordnung*, Zeitschr. Phys. **41**, 184 (1927).

[64] M. v. Laue, *Röntgenstrahlinterferenzen* (Akademische Verlagsgesellschaft, Leipzig, 1941).

[65] D. Y. K. Ko and J. C. Inkson, *Matrix method for tunneling in heterostructures: Resonant tunneling in multilayer systems*, Phys. Rev. **B 38**, 9945 (1988).

[66] C. D. Ager and H. P. Hughes, *Optical properties of stratified systems including lamellar gratings*, Phys. Rev. **B 44**, 13452 (1991).

[67] S. Pereira, *Private Communication*, University of Karlsruhe, Germany (2005).

[68] J. D. Jackson, *Klassische Elektrodynamik* (de Gruyter, Berlin, 1981).

[69] S. Linden, N. Rau, U. Neuberth, A. Naber, M. Wegener, S. Pereira, K. Busch, A. Christ, and J. Kuhl, *Near-field optical microscopy and spectroscopy of one-dimensional metallic photonic crystal slabs*, Phys. Rev. **B 71**, 245119 (2005).

[70] T. Tamir, editor, *Guided-Wave Optoelectronics*, Springer Series in Electronics and Photonics 26 (Springer-Verlag, Berlin, 1994).

[71] A. Ghatak and K. Thyagarajan, *Introduction to Fiber Optics* (Cambridge University Press, 1998).

[72] A. Yariv and M. Nakamura, *Periodic structures for integrated optics*, IEEE J. Quant. Electr. **57**, 233 (1977).

[73] H. Haug and S. W. Koch, *Quantum Theory of the Optical and Electronic Properties of Semiconductors* (World Scientific, Singapur, 1998).

[74] M. V. Kurig, *Urbach rule*, phys. stat. sol. (a) **8**, 9 (1971).

[75] G. D. Cody, T. Tiedje, B. Abeles, B. Brooks, and Y. Goldstein, *Disorder and the optical-absorption edge of hydrogenated amorphous silicon*, Phys. Rev. Lett. **47**, 1480 (1981).

[76] R. Zallen, R. E. Drews, R. L. Emerald, and M. L. Slade, *Electronic structure of crystalline and amorphous As_2S_3 and As_2Se_3*, Phys. Rev. Lett. **26**, 1564 (1971).

[77] K. L. Chopra and S. K. Bahl, *Structural, electrical, and optical properties of amorphous Germanium films*, Phys. Rev. **B 1**, 2545 (1970).

[78] D. L. Wood and J. Tauc, *Weak absorption tails in amorphous semiconductors*, Phys. Rev. **B 5**, 3144 (1972).

[79] E. P. Wigner, *Characteristic vectors of bordered matrices with infinite dimensions*, Ann. Math. **62**, 548 (1955).

[80] D. H. Dunlap, K. Kundu, and P. Phillips, *Absence of localization in certain statistically disordered lattices in any spatial directions*, Phys. Rev. **B 40**, 10999 (1989).

[81] D. H. Dunlap, H-L. Wu, and P. W. Phillips, *Absence of localization in a random-dimer model*, Phys. Rev. Lett. **65**, 88 (1990).

[82] C. M. Soukoulis, M. J. Velgakis, and E. N. Economou, *One-dimensional localization with correlated disorder*, Phys. Rev. **B 50**, 5110 (1994).

[83] F. M. Izrailev and A. A. Krokhin, *Localization and the mobility edge in one-dimensional potentials with correlated disorder*, Phys. Rev. Lett. **82**, 4062 (1999).

[84] R. Hagen and T. Bieringer, *Photoaddressable polymers for optical data storage*, Adv. Mat. **13**, 1805 (2001).

[85] Y. Sabi, M. Yamamoto, H. Watanabe, T. Bieringer, D. Haarer, R. Hagen, and S. G. Kostromine, *Photoaddressable polymers for rewritable optical disc systems*, Jpn. J. Appl. Phys. **40**, 1613 (2001).

[86] V. Cimrova, D. Neher, S. G. Kostromine, and T. Bieringer, *Optical anisotropy in films of photoaddressable polymers*, Makromolecules **32**, 8496 (1999).

[87] M. Eich and J. Wendorff, *Laser-induced gratings and spectroscopy in monodomains of liquid-crystalline polymers*, J. Opt. Soc. Am. **B 7**, 1428 (1990).

[88] S. Hvilsted, F. Andruzzi, and P.S. Ramanujam, *Side-chain liquid-crystalline polyesters for optical information storage*, Opt. Lett. **17**, 1234 (1992).

[89] G. C. Hartley, *The cis-form of azobenzene*, Nature **140**, 281 (1937).

[90] R. P. Bertram, *Photoadressierbare Polymere als neue elektrooptische Materialien*, Ph.D. thesis, Universität Bonn (2004).

[91] S. J. Zilker, T. Bieringer, D. Haarer, R. S. Stein, J. W. van Egmond, and S. G. Kostromine, *Holographic data storage in amorphous polymers*, Adv. Mat. **10**, 855 (1998).

[92] B. L. Lachut, S. A. Maier, H. A. Atwater, M. J. A. de Dood, A. Polman, R. Hagen, and S. G. Kostromine, *Large spectral birefringence in photoaddressable polymer films*, Adv. Mat. **16**, 1746 (2004).

[93] R. P. Bertram, N. Benter, D. Apitz, E. Soergel, K. Buse, R. Hagen, and S. G. Kostromime, *Increased thermal stability of a poled electro-optic polymer using high-molar mass fractions*, Phys. Rev. **E 70**, 041802 (2004).

[94] R. P. Bertram, E. Soergel, H. Blank, N. Benter, K. Buse, R. Hagen, and S. G. Kostromime, *Strong electro-optic effect in electrically poled photoaddressable polymers*, J. Appl. Phys. **94**, 6208 (2003).

[95] D. Apitz, R. P. Bertram, N. Benter, W. Hieringer, J. W. Andreasen, M. M. Nielsen, P. M. Johansen, and K. Buse, *Investigation of chromophore-chromophore interaction by electro-optic measurements, linear dichroism, X-ray scattering and density-functional calculations*, Phys. Rev. **E 72**, 036610 (2005).

[96] H. Guo, to be published.

[97] S. H. Lee, H. M. Cheong, P. Liu, D. Smith, C. E. Tracy, A. Mascarenhas, J. R. Pitts, and S. K. Deb, *Gasochromic mechanism in* $\mathrm{a-WO_3}$ *thin films based on Raman spectroscopic studies*, J. Appl. Phys. **88**, 3076 (2000).

[98] K. Ito and T. Kubo, *Gas detection by hydrochromism*, Proc. of the 4^{th} Sensor Symposium 153 (1984).

[99] K. Ito and T. Ohgami, *Hydrogen detection based on coloration of anodic tungsten oxide film*, Appl. Phys. Lett. **60**, 938 (1992).

[100] D. K. Benson, C. E. Tracy, S. H. Lee, G. A. Hishmeh, D. P. Haberman, and P. A. Ciszek, *Low-cost, fiber-optic hydrogen gas detector using guided-wave, surface-plasmon resonance in chemochromic thin films*, Proc. of SPIE Photonics East **3535**, 185 (1998).

[101] S. H. Lee, H. M. Cheong, J.-G. Zhang, A. Mascarenhas, D. K. Benson, and S. K. Deb, *Electrochromic mechanism in* $\mathrm{a-WO_{3-y}}$ *thin films*, Appl. Phys. Lett. **74**, 242 (1999).

[102] S. H. Lee, H. M. Cheong, C. E. Tracy, A. Mascarenhas, A. W. Czanderna, and S. K. Deb, *Electrochromic coloration efficiency of* $\mathrm{a-WO_{3-y}}$ *thin films as a function of oxygen deficiency*, Appl. Phys. Lett. **75**, 1541 (1999).

[103] K. v. Rottkay, M. Rubin, and S.-J. Wen, *Optical indices of electrochromic tungsten oxide*, Thin Solid Films **306**, 10 (1997).

[104] C. Bechinger, G. Oefinger, S. Herminghaus, and P. Leiderer, *On the fundamental role of oxygen for the photochromic effect of* WO_3, J. Appl. Phys. **74**, 4527 (1993).

[105] S. K. Deb, *Optical and photoelectrical properties and colour centres in thin films of tungsten oxide*, Philos. Mag. **27**, 801 (1973).

[106] C. Bechinger, E. Wirth, and P. Leiderer, *Photochromic coloration of* WO_3 *with visible light*, Appl. Phys. Lett. **68**, 2834 (1996).

[107] R. D. Smith, P. Liu, S. H. Lee, E. Tracy, and R. Pitts, *Interfacial stability of thin film fiber-optic hydrogen sensor*, Proc. of the 2002 U.S. DOE Hydrogen Program Review NREL/CP–610–32405 (2002).

[108] C. Gerthsen and H. Vogel, *Physik* (Springer-Verlag, Berlin, 1993).

[109] H. C. Guo, D. Nau, A. Radke, X. P. Zhang, J. Stodolka, X. L. Yang, S. G. Tikhodeev, N. A. Gippius, and H. Giessen, *Large-area metallic photonic crystal fabrication with interference lithography and dry etching*, Appl. Phys. B **81**, 271 (2005).

[110] J. Villatoro and D. Monzón-Hernández, *Fast detection of hydrogen with nano fiber tapers coated with ultra thin palladium layers*, Opt. Expr. **13**, 5087 (2005).

[111] A. P. Jardine, *Hydrogen sensors for hydrogen fuel cell applications*, `http://www.powerpulse.net/features/techpaper.php?paperID=99`.

[112] S. Okazaki, H. Nakagawa, S. Asakura, Y. Tomiuchi, N. Tsuji, H. Murayama, and M. Washija, *Sensing characteristics of an optical fiber sensor for hydrogen leak*, Sens. Actuators B **93**, 142 (2003).

[113] H. Raether, *Surface Plasmons* (Springer-Verlag, Berlin, 1988).

[114] J. Wöllenstein, J. A. Plaza, C. Cané, Y. Min, H. Böttner, and H. L. Tuller, *A novel single chip thin film metal oxide array*, Sens. Actuators B **93**, 350 (2003).

[115] Y.-K. Chung, M.-H. Kim, W.-S. Um, H.-S. Lee, J.-K. Song, S.-C. Choi, K.-M. Yi, M.-J. Lee, and K.-W. Chung, *Gas sensing properties of* WO_3 *thick film for* NO_2 *gas dependent on process condition*, Sens. Actuators B **60**, 49 (1999).

[116] T. Meier and P. Thomas, *Echos in Festkörpern*, Physik Journal **2**, 53 (2003).

[117] N. A. Kurnit, I. D. Abella, and S. R. Hartmann, *Observation of a photon echo*, Phys. Rev. Lett. **13**, 567 (1964).

[118] G. Noll, U. Siegner, S. G. Shevel, and E. O. Göbel, *Picosecond stimulated photon echo due to intrinsic excitations in semiconductor mixed crystals*, Phys. Rev. Lett. **64**, 792 (1990).

[119] B. Lamprecht, J. R. Krenn, A. Leitner, and F. R. Aussenegg, *Resonant and off-resonant light-driven plasmons in metal nanoparticles studied by femtosecond-resolution third-harmonic generation*, Phys. Rev. Lett. **83**, 4421 (1999).

[120] A. Schönhardt *et al.*, *Puls-propagation in metallic photonic crystals*, Phys. Rev. **B** (to be published).

[121] E. Betzig and J. K. Trautman, *Near-field optics: microscopy, spectroscopy, and surface modification beyond the diffraction limit*, Science **257**, 189 (1992).

[122] J. D. Gaskill, *Linear Systems, Fourier Transforms, and Optics* (John Wiley & Sons, 1978).

Danksagung

Diese Arbeit konnte nicht ohne die wichtige Hilfe anderer Personen entstehen. Ich danke insbesondere

- Prof. Harald Gießen dafür, daß er mir die Gelegenheit gegeben hat, in seiner Gruppe zu arbeiten. Ich danke für sein stetiges Interesse an meiner Arbeit und die tolle und motivierende Zusammenarbeit.
- Prof. Karsten Buse für die freundliche Übernahme des Zweitgutachtens.
- Hongcang Guo, Sebastian Pricking, Anja Schönhardt, Jörn Teipel, Diana Türke, Rui Zhang und Xinping Zhang für die angenehme Atmosphäre in unserer Arbeitsgruppe. Euch allen danke ich für die tolle Unterstützung und die schöne gemeinsame Zeit! Ebenso allen anderen Mitgliedern der AG Gießen in Bonn und Stuttgart.
- Christina Bauer, André Christ und Thomas Zentgraf vom Max-Planck-Institut für Festkörperforschung in Stuttgart für die Herstellung der Proben, ohne die die hier gezeigten Ergebnisse nicht möglich geworden wären, und für viele fruchtbare Diskussionen. Herrn Jürgen Kuhl danke ich für die Gastfreundschaft bei meinen Besuchen in der Spektroskopie-Gruppe.
- Allen Mitgliedern des Instituts für Angewandte Physik und des Heinrich-Hertz-Lehrstuhls der Universität Bonn für die guten Arbeitsbedingungen, die freundliche Atmosphäre und jede Hilfe. Ganz besonders danken möchte ich Rainer Langen, Klaus-Dieter Krause und ihren Mitarbeitern für die technische Unterstützung und die stets hervorragende Arbeit.
- Prof. Hans Kroha für etliche Diskussionen, die viel zu meinem Verständnis über Unordnung beigetragen haben.
- Prof. Peter Thomas (Universität Marburg) dafür, daß er meine Aufmerksamkeit auf korrelierte Unordnung gerichtet hat.
- Prof. Sergei G. Tikhodeev (Universität Moskau) für Diskussionen über Unordnung und photonische Kristalle sowie für das Bereitstellen des Streumatrixprogramms.
- Satyen K. Deb und Se-Hee Lee (NREL, Golden, Colorado/USA) für die Bereitstellung der WO_3-Substrate.

- Ein ganz besonderer Dank gebührt meinen Eltern und meiner Familie, ohne deren Unterstützung ich nicht der wäre, der ich heute bin.

- Ein ganz lieber Dank gilt meiner Anja für die schöne gemeinsame Zeit und die liebevolle Unterstützung. Ohne Dich wäre es sehr viel schwieriger gewesen!